

PL-TR-93-2021

AD-A267 294



2  
DA

# Nowcasting Methods for Satellite Imagery

Thomas Nehrkorn

Thomas M. Hamill

Lawrence W. Knowlton

DTIC  
ELECTE  
JUL 13 1993  
S A D

Atmospheric and Environmental Research, Inc.  
840 Memorial Drive,  
Cambridge, MA 02139

May 27, 1993

Scientific Report No. 1

Approved for public release; distribution unlimited

93


6

93-15768



**PHILLIPS LABORATORY**  
**Directorate of Geophysics**  
**AIR FORCE MATERIEL COMMAND**  
**HANSCOM AIR FORCE BASE, MA 01731-3010**

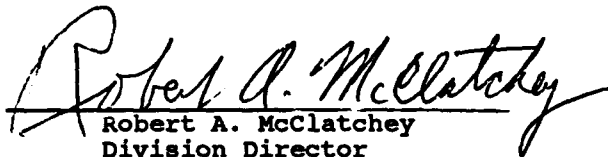
"This technical report has been reviewed and is approved for publication"



Kenneth F. Heideman  
Contract Manager



Donald A. Chisholm  
Branch Chief



Robert A. McClatchey  
Division Director

This report has been reviewed by the ESC Public Affairs Office (PA) and is releasable to the National Technical Information Service (NTIS).

Qualified requestors may obtain additional copies from the Defense Technical Information Center. All others should apply to the National Technical Information Service.

If your address has changed, or if you wish to be removed from the mailing list, or if the addressee is no longer employed by your organization, please notify PL/TSI, Hanscom AFB, MA 01731-3010. This will assist us in maintaining a current mailing list.

Do not return copies of this report unless contractual obligations or notices on a specific document requires that it be returned.

REPORT DOCUMENTATION PAGE			Form Approved OMB No. 0704-0188	
Public reporting burden for this collection of information is estimated to average 1 hour per response, including the time for reviewing instructions, searching existing data sources, gathering and maintaining the data needed, and completing and reviewing the collection of information. Send comments regarding this burden estimate or any other aspect of this collection of information, including suggestions for reducing this burden, to Washington Headquarters Services, Directorate for Information Operations and Reports, 1215 Jefferson Davis Highway, Suite 1204, Arlington, VA 22202-4302, and to the Office of Management and Budget, Paperwork Reduction Project (0704-0188), Washington, DC 20503.				
1. AGENCY USE ONLY (Leave blank)		2. REPORT DATE May 27, 1993		3. REPORT TYPE AND DATES COVERED Scientific Report No. 1
4. TITLE AND SUBTITLE Nowcasting Methods for Satellite Imagery			5. FUNDING NUMBERS Contract F19628-92-C-0014 PE63707F PR2688 TR06 WULB	
6. AUTHOR(S) Thomas Nehrkorn, Thomas Hamill, Lawrence W. Knowlton				
7. PERFORMING ORGANIZATION NAME(S) AND ADDRESS(ES) Atmospheric and Environmental Research, Inc. 840 Memorial Drive Cambridge, MA 02139			8. PERFORMING ORGANIZATION REPORT NUMBER	
9. SPONSORING/MONITORING AGENCY NAME(S) AND ADDRESS(ES) Phillips Laboratory 29 Randolph Rd. Hanscom AFB, MA 01731-3010 Contract Manager: Kenneth Heideman/GPAP			10. SPONSORING/MONITORING AGENCY REPORT NUMBER PL-TR-93-2021	
11. SUPPLEMENTARY NOTES				
12. DISTRIBUTION AVAILABILITY STATEMENT Approved for public release; distribution unlimited.			13. DISTRIBUTION CODE	
14. ABSTRACT (Maximum 200 words) <p>This report documents the development and testing of nowcasting methods for satellite imagery. Techniques for identifying, tracking, and forecasting features of interest through contours of brightness temperature in geostationary IR imagery were evaluated in a study covering over 200 features from all four seasons. Results indicate that because contours frequently split, merge, or dissipate, contour based techniques are successful in only a minority of cases. The most skillful contour extrapolation technique is movable persistence, which simply extrapolates the position of the contour based on the past movement of its centroid position. Its verification scores are significantly better than persistence for forecasts from 1/2 to 3 hours in advance.</p> <p>As an alternative to the contour-based schemes, a cross-correlation technique for predicting short-term changes in pixel grayshade values (brightness temperatures) was developed and tested. Pixel-based verification of the cross-correlation forecasts show an improvement over persistence out to 2 1/2 hours (the longest time period studied for this technique). Contour forecasts derived from the cross-correlation are significantly more skillful than those of the best contour extrapolation technique (movable persistence) out to 1 hour, and no worse out to 2 1/2 hours.</p>				
14. SUBJECT TERMS Satellite imagery, nowcasting, cross-correlation, image processing			15. NUMBER OF PAGES 122	
			16. PRICE CODE	
17. SECURITY CLASSIFICATION OF REPORT Unclassified	18. SECURITY CLASSIFICATION OF THIS PAGE Unclassified	19. SECURITY CLASSIFICATION OF ABSTRACT Unclassified	20. LIMITATION OF ABSTRACT SAR	

## **Table of Contents**

List of Figures	iv
List of Tables	viii
1. Introduction	1
2. Description of Contour Selection and Contour Forecast Algorithms	5
2.1 Contour Selection Software	5
2.1.1 Remapping of Geostationary Data	5
2.1.2 Contour Level Selection.	7
2.1.3 Contour Generation / Selection	7
2.1.4 Storage of Contour and Pixel Information.	8
2.2 Forecast Algorithm Description	8
2.2.1 Whole Contour Technique	8
2.2.2 Segmentation Technique	9
2.2.3 Adaptive Exponential Smoothing (Kavvas) Technique	10
2.2.4 Movable Persistence	11
2.2.5 Persistence	11
2.2.6 Cross - Correlations Technique	12
3. Evaluation of Forecast Techniques	14
3.1. Approach	14
3.2. Stratification of Cases	17
3.3. Sensitivity Tests	22
3.3.1. Whole Contour Method:	22
3.3.2. Segmentation Method:	24
3.3.3. Kavvas Method:	26
3.4. Forecast Method Intercomparison	28
3.4.1 Intercomparison of Three Contour Extrapolation Techniques	28
3.4.2. Significance Testing and Comparison With Other Techniques	29
4. Summary of Results and Recommendations	32
5. References	35
Appendix A: A Short-Term Cloud Forecast Scheme Using Cross Correlations	108

INFO QUALITY INSPECTED 5

Accession For	
NTIS	CRA&I <input checked="" type="checkbox"/>
DTIC	TAB <input type="checkbox"/>
Unannounced <input type="checkbox"/>	
Justification	
By	
Distribution /	
Availability Codes	
Dist	Avail and/or Special
A-1	

## **List of Figures**

- Figure 1: Illustrating how initial frames (time  $t-\Delta t$  and  $t$ , on left) from a time series of analyzed contours can be used to generate forecast contours (for time  $t+\Delta t$ , on right). 2
- Figure 2 Domain used in testing the cloud forecast techniques. The domain is a Lambert-conformal projection true at 30 and 60 N. 37
- Figure 3 A sample frame of raw GOES IR imagery remapped to the Lambert conformal projection. Map overlay is not included here, but the domain corresponds to the one shown in Figure 2. The imagery was from 1500 UTC 20 Nov 1991. 38
- Figure 4 A subframe of GOES imagery taken from 3, with contours overlaid for pixel brightness 181. 39
- Figure 5 The same subframe of GOES imagery as shown in Figure 4, but after the selection of the one feature for tracking and deletion of all other features. 39
- Figure 6 Illustration of a sample contour (a) and the decomposition into x- and y- coordinates (b) (from Bianco and Huang 1990). 40
- Figure 7 Illustration of the concept of defining a contour using a centroid and a set of line lengths radiating from the centroid. 41
- Figure 8 Illustration of correlation analysis and derivation of the displacement vector. The displacement vector is directed from the center of the correlation box in Image 1 to the center of the correlation box in Image 2 most highly correlated with Image 1. 41
- Figure 9 Example of a correlation field used in the derivation of a displacement vector. The point (12, 12) is the center of the original correlation box. The displacement vector originates at this point and ends at the point with the highest correlation. 42
- Figure 10 (a) Raw displacement vectors, (b) displacement vectors after a quality control, and (c) objectively analyzed displacement vectors for the same satellite scene as shown in Figure 5. 42

Figure 11 Illustration of two contours bounding a forecast area (A + C), and a verification area (A + B), and the breakdown into regions of hits (A), misses (B), and false alarms (C).	43
Figure 12: Verification scores for the CONTROL sample for fall, for the whole contour method with method number = 2. Shown are CSI (a), POD (b), FAR (c), BIAS (d), and RMSE (e) as a function of frequency (number of modes). The different lines correspond to different forecast increments: increment 1 (solid), increment 2 (dotted), increment 3 (short dashes), increment 4 (dash-dot), increment 5 (dash-dot-dot-dot), and increment 6 (long dashes).	44-45
Figure 13: Same as Figure 12, except for method number = 3.	46-47
Figure 14: Same as Figure 12, except for method number = 4.	48-49
Figure 15: Verification scores for the SLOW feature sample for fall, for the whole contour method with method number = 2. Shown are CSI (a) and RMSE (b) as a function of frequency (number of modes). The different lines correspond to different forecast increments, as in Figure 12.	50
Figure 16: Same as Figure 15, except for the FAST feature subsample.	51
Figure 17: Same as Figure 15, except for the LARGE feature subsample.	52
Figure 18: Same as Figure 15, except for the SMALL feature subsample.	53
Figure 19: Same as Figure 15, except for the PRE2 subsample.	54
Figure 20: Same as Figure 15, except for the PRE4 subsample.	55
Figure 21: Same as Figure 15, except for the PRE6 subsample.	56
Figure 22: Same as Figure 12, except for winter.	57-58
Figure 23: Same as Figure 12, except for spring.	59-60
Figure 24: Same as Figure 12, except for summer.	61-62
Figure 25: Verification scores for the CONTROL sample for fall, for the segmentation method. Shown are CSI (a), POD (b), FAR (c), BIAS (d), and RMSE (e) as a function of the segmentation angle (in °). The different lines correspond to different forecast increments, as in Figure 12.	63-64
Figure 26: Verification scores for the SLOW feature sample for fall, for the segmentation method. Shown are CSI (a) and RMSE	

(b) as a function of the segmentation angle (in $^{\circ}$ ). The different lines correspond to different forecast increments, as in Figure 12.	65
Figure 27: Same as Figure 26, except for the FAST feature subsample.	66
Figure 28: Same as Figure 26, except for the LARGE feature subsample.	67
Figure 29: Same as Figure 26, except for the SMALL feature subsample.	68
Figure 30: Same as Figure 26, except for the PRE2 subsample.	69
Figure 31: Same as Figure 26, except for the PRE4 subsample.	70
Figure 32: Same as Figure 26, except for the PRE6 subsample.	71
Figure 33: Same as Figure 25, except for winter.	72-73
Figure 34: Same as Figure 25, except for spring.	74-75
Figure 35: Same as Figure 25, except for summer.	76-77
Figure 36: Verification scores for the CONTROL sample for fall, for the Kavvas method. Shown are CSI (a), POD (b), FAR (c), BIAS (d), and RMSE (e) as a function of the smoothing coefficient. The different lines correspond to different forecast increments, as in Figure 12.	78-79
Figure 37: Verification scores for the SLOW feature sample for fall, for the Kavvas method. Shown are CSI (a) and RMSE (b) as a function of the smoothing coefficient. The different lines correspond to different forecast increments, as in Figure 12.	80
Figure 38: Same as Figure 37, except for the FAST feature subsample.	81
Figure 39: Same as Figure 37, except for the LARGE feature subsample.	82
Figure 40: Same as Figure 37, except for the SMALL feature subsample.	83
Figure 41: Same as Figure 37, except for the PRE2 subsample.	84
Figure 42: Same as Figure 37, except for the PRE4 subsample.	85
Figure 43: Same as Figure 37, except for the PRE6 subsample.	86
Figure 44: Same as Figure 36, except for winter.	87-88
Figure 45: Same as Figure 36, except for spring.	89-90
Figure 46: Same as Figure 36, except for summer.	91-92

Figure 47: Verification scores for the CONTROL sample for fall as a function of forecast increment. Shown are the sample size (a), CSI (b), POD (c), FAR (d), BIAS (e), and RMSE (f) . The different lines correspond to different forecast techniques: segmentation (solid), whole contour (dotted), Kavvas (dashed).	93-94
Figure 48: Verification scores for the SLOW feature subsample for fall as a function of forecast increment. Shown are the sample size (a), CSI (b), and RMSE (c) . The different lines correspond to different forecast techniques, as in Figure 47.	95
Figure 49: Same as Figure 48, except for the FAST feature subsample.	96
Figure 50: Same as Figure 48, except for the LARGE feature subsample.	97
Figure 51: Same as Figure 48, except for the SMALL feature subsample.	98
Figure 52: Same as Figure 47, except for winter.	99-100
Figure 53: Same as Figure 47, except for spring.	101-102
Figure 54: Same as Figure 47, except for summer.	103-104
Figure 55: Mean verification scores with 5% confidence intervals from the ANOVA for the CONTROL sample for the whole year as a function of forecast increment. Shown are the CSI (a), POD (b), and FAR (c). The different lines, and symbols used for the confidence intervals, correspond to different forecast techniques: segmentation (solid, asterisk), whole contour (dotted, X), Kavvas (dashed, diamond), and persistence (dash-dot-dot-dot, square), movable persistence based on the center of mass (dash-dot, triangle), and based on the mean contour position (long dashes, confidence intervals omitted for clarity).	105
Figure 56: As Fig. 55, but with the whole contour technique eliminated from the comparison.	106
Figure 57: Mean verification scores with 5% confidence intervals for the contour forecasts from the cross-correlation technique (solid, asterisk) and movable persistence based on the center of mass (dashed, diamond). From the ANOVA for the 40 case sample for the whole year. Shown are the CSI (a), POD (b), and FAR (c) as a function of forecast increment.	107



### **List of Tables**

1: Case parameter values of samples (sets of cases) used for forecast method testing and verification.	18
2: Distribution of feature sizes for the fall season	19
3: Distribution of translation speeds for the fall season	20

## **1. Introduction**

One of the weather forecast tools wanted by the U.S. Air Force is one to help make more effective nowcasts of cloud and precipitation features. In the future, the weather forecaster will have more data available than can be synthesized in a short amount of time, so schemes which simplify the job of forecasting are desirable. Another desirable characteristic for such a scheme is the ability to work with very little data, since many Air Force operations are in data-denied areas or areas where active sensors cannot be operated. The Air Force Phillips Laboratory has been actively engaged in developing and testing prototype nowcasting schemes meeting these criteria. Once developed and adequately tested, a prototype scheme could eventually be transferred to an Air Force meteorological workstation such as the Automated Weather Distribution System, or AWDS.

The focus of previous work at the Phillips Laboratory for nowcasting clouds and precipitation has been on contour extrapolation techniques for radar and satellite data. The basic idea of the contour extrapolation schemes is as follows: the cloud elements with significant weather can be identified as areas bounded by some significant contour; for example, the precipitating area of a thunderstorm may be defined by a cloud top temperature of colder than -50 C. With a time series of bounding contours around the -50 C area, an intelligent extrapolation of the future size, shape, and movement may be estimated (Figure 1). A number of forecast schemes have been developed or tailored at the Phillips Laboratory. They are: (1) the whole contour technique (Bohne et al. 1988) (Bianco and Huang 1990); (2) the segmentation method (ibid); (3) the adaptive exponential smoothing technique, also called the

Kavvas technique (Kavvas and Chen 1989), and (4) movable persistence.

Section 2 of this report will elaborate more on these schemes.

Prior testing of these schemes had been limited by the cumbersome contour selection process, which had not been automated and involved contouring a satellite image, producing paper plots of the contours, searching the paper plots for trackable features, etc. Some problems were quickly discovered: first, this method was very slow. Second, many of the desired features did not remain coherent over a large number of frames, i.e., one feature split into many, two features merged into one, a feature totally dissipated. None of the contouring schemes were designed to handle such cases. Because of these limitations, a comparison of forecast skill among the different schemes proved inconclusive due to small sample size (Heideman et al. 1990; Ruggiero et al. 1991).

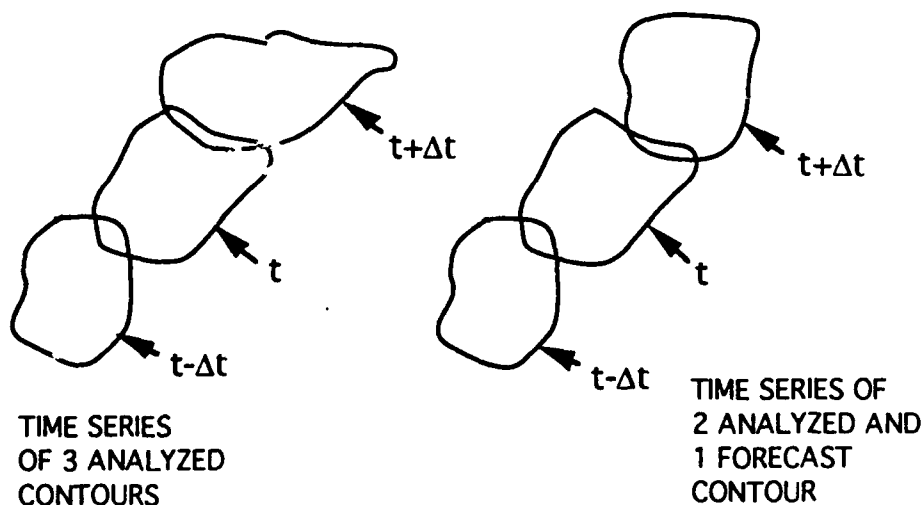


Figure 1. Figure illustrating how initial frames (time  $t-\Delta t$  and  $t$ , on left) from a time series of analyzed contours can be used to generate forecast contours (for time  $t+\Delta t$ , on right).

As a result, the Phillips Lab initiated a contract to adequately test the contouring schemes and to recommend one winner for technology transition or further development. This report documents the work performed under this contract. As agreed with the Phillips Laboratory, we proposed in the contract to:

(1) Develop a prototype display and archive software to allow a user to loop up consecutive frames of remapped satellite imagery or display each separately. Using a mouse, the user could then select a pixel having the brightness temperature desired to use for a contour, and display/overlay contours for each of the frames of satellite imagery. Last, this software would archive the contours for use by the forecasting and verification programs.

(2) Examine possible enhancements to the existing algorithms which would broaden their generality. Ways to deal with the splitting and merging of contours, to forecast multiple cloud layers, and to deal with boundary intersections would be studied.

(3) Study replacement algorithms which may be more generally applicable. These algorithms would be abandoned or recommended as candidates for further development and testing, depending on the results of the test with the contouring algorithms.

(4) Test each algorithm over a broad range of cases (50 for each season) and verify algorithm skill using the standard skill scores such as probability of detection, false alarm rate, critical success index, and root mean square error. Selection of the cases to be tested was to be done on the basis of meteorological interest, *not on what the algorithm could handle*. Rephrased, to simulate the process in a real forecasting situation, the areas

to be selected had dynamic or interesting weather. This was done to simulate the situations in which a weather forecaster was likely to seek forecast advice from an automated algorithm. Thus, if any or all of the schemes did not work, this would have been noted. The results would indicate the percent of the time each scheme was able to produce a usable forecast. Further, if generalities could be made about regimes where an algorithm is strong or weak, these would be made.

One modification that was made shortly after we began the contract was to abandon the search for algorithmic improvements which could handle splitting and merging and instead focus on the development of a new forecast scheme based on cross-correlations. This was done for two reasons. First, after some preliminary research, we saw no easy way to handle the splitting and merging of features, and attempting work on this problem could have slowed down the evaluation process. Further, with four candidate forecast techniques, four general solutions might have been required, but the short timeline of the project may have dictated our improving only one of the four techniques, thus possibly biasing the evaluation to the one selected for improvement. The second major reason was that the technique of cross-correlations (Bellon et al. 1992) avoided many of the pitfalls of the contouring techniques, producing full forecast IR satellite images rather than contour forecasts. Thus, time allotted for tasks (2) and (3) above were mostly spent in the development of a new, prototype cross-correlations scheme.

This report, then, documents the resulting contract work performed over the last year on satellite nowcasting. Some of the work, namely, the testing of the cross-correlations technique on synoptic-scale features, has already been described (Hamill and Nehrkorn 1993). In this report, we will

first give a quick overview of the forecast schemes (Section 2), and an in-depth summary of the evaluation process and the results (Section 3). The last part, Section 4, provides conclusions.

## **2. Description of Contour Selection and Contour Forecast Algorithms**

This section describes the new contour selection and cross-correlations forecast software developed this year and reviews the existing contour forecast schemes.

### **2.1 Contour Selection Software**

A way of selecting trackable contour features was obviously needed before forecasts could be run or verified. As mentioned before, the pre-existing process for selecting cases for testing the algorithms was cumbersome, involving a lengthy remapping process, production of paper plots of contours, and other time-consuming steps. With new software tools available (specifically, an image processing language called PVWAVE) it was decided the first part of the time should be allotted to developing new front-end software. This software would be an integrated package to interactively remap satellite data, allow the user to examine the remapped data and to select features for examination, contour them, and store the contour and pixel information if desired for later input to the forecast algorithms. The components of this system are summarized below.

#### **2.1.1 Remapping of Geostationary Data**

The forecast domain selected from which cases were chosen is shown in Figure 2. It is a Lambert-conformal map projection true at 30 and 60

degrees N, with the domain centered at 41.36 degrees N latitude, and 88.68 degrees W longitude (Marseilles, IL). The new software remaps to a 256\*256 grid, with an effective resolution of approximately 11 km (later the grid is expanded to a 512\*512 grid through pixel replication). Contour selection and evaluation were judged to be easier and more accurate in a Lambert projection than in the projection of the raw GOES data, where the earth's curvature was apparent.

Previously, remapping GOES data to the Lambert projection was done in batch mode because of the extended length of the job. The remapping process now has been speeded up so it can be done interactively. The old remapping software was designed to perform a coordinate conversion for every pixel on the Lambert grid, a computationally intensive process. The algorithm would start with pixel (1,1), determine the location in the raw GOES image, and remap the pixel value, and proceed to (2,1), (3,1), and so on. Because the coordinate conversion can be considered linear over small sections of the forecast domain, we decided that only a select few points needed to be fully coordinate converted, and the rest of the conversion could be done by interpolation. For example, say that we know pixel (1,1) corresponds to pixel (a,b) in the forecast image, and (3,1) corresponds to (c,d). Then, assuming linearity, we can calculate the coordinate of (2,1) as  $((a+c)/2, (b+d)/2)$ . In our algorithm, we actually perform the coordinate conversion every 15 pixels in each direction, and determine the rest through bilinear interpolation. The resulting remapped image is indistinguishable from the same image remapped with a full coordinate conversion, and the time savings is tremendous; on the VAX 3600 workstation, remapping six frames of imagery takes 2-3 minutes, whereas the old method took 30 minutes.

### **2.1.2 Contour Level Selection.**

After the image has been remapped, the analyst has a set of tools available for inspecting the image and selecting an interesting subimage and a level for contouring. Some of the features are:

- (1) Looping capabilities.
- (2) Ability to examine a single frame of the image.
- (3) Enhancement tables.
  - (a) GOES ZA and ZB tables (Clark 1983),
  - (b) A set of 15 false color enhancement tables,
  - (c) Interactive generation of new enhancement tables.
- (4) Storage of remapped imagery for quicker reprocessing later.

The user also has a choice of how a contour level can be selected. The user can: (1) Enter the pixel brightness value to use as a contour, or (2) Click on a pixel on the screen and use the value of the pixel at that location. The user also can select the size of the subdomain around the feature, inside which the contouring will take place. Figure 3 illustrates one sample remapped frame of satellite imagery that might be examined for selection of a trackable contour feature.

### **2.1.3 Contour Generation / Selection**

The new package is also set up to contour the image and to display the resulting contours overlaid on the original satellite image loop (Figure 4).



Since there may be more than one contour in a given subframe, if the user decides that one of the features is trackable (i.e., contiguous over many frames), then the software will prompt the user to click a mouse button inside the feature of interest. The software will automatically delete any other contours, and once again display a satellite loop with the one selected contour feature overlaid (Figure 5).

#### **2.1.4 Storage of Contour and Pixel Information.**

The last step performed is the storage of either contour information (for the contour forecast techniques) or actual satellite subframes (for the cross-correlation scheme). The contour information is stored in a form that is usable as input by all the contouring schemes, and the satellite subframes can be read into the correlation scheme directly.

### **2.2 Forecast Algorithm Description**

The evaluation of the cloud forecasts was to be done for six techniques; the first five were all contouring techniques, and the last, the cross-correlations, produces pixel forecast images, from which contours can be extracted for comparison with the other schemes. A brief explanation of each of the schemes is given below.

#### **2.2.1 Whole Contour Technique**

The whole contour technique is more completely described in Bianco and Huang (1990). The premise of this scheme is that a contour can be sampled at regular points along the contour, and described by a periodic set of x- and y-coordinates. A graph of the x- and y-components shows they are periodic; thus, they can be decomposed by Fourier analysis into a spectral

representation of phases and amplitudes (Figure 6). The number of waves describing the contour can be specified by the user; the more waves, the more accurate the initial description of the shape of the contour.

In addition to phases and amplitudes, the centroid positions and aspect ratios (length / height) are also calculated. All the calculated parameters, including the time tendencies for each Fourier component, are then linearly extrapolated in time, and a forecast contour is reconstructed through an inverse transform. The forecast shape and size are scaled to fit the extrapolated aspect ratio and area. The position of the contour is determined from the extrapolated centroid position, with the centroid position defined as the average of the contour boundary values.

The testing of this scheme allowed the user to vary the number of previous observations used to initialize the model. For two previous observations, only a simple linear extrapolation was possible. With three or more observations, this linear extrapolation estimate was improved through a least-squares regression. The user was also able to vary the number of Fourier components used in the analysis (from 1 to 5) and the forecast method, which allowed linear extrapolation of the Fourier amplitude and phases, or more complex extrapolations including relationships between adjacent Fourier components.

### **2.2.2 Segmentation Technique**

The segmentation technique is also described in Bianco and Huang (1990), where it is referred to as the "angle displacement method." The abbreviated description given in Ruggiero et al. (1991) is used here.

The segmentation technique defines a contour by its centroid position and the length of lines radiating out from the centroid to the contour boundary (Figure 7). The lines are at equally spaced angles around the centroid. The angle separating the line segments is called the displacement (alpha) angle and is determined by the user. The segmentation technique uses a linear least squares fit to forecast future line lengths and centroid position. The contour is reconstructed by connecting the endpoints of the lines radiating out from the forecast centroid.

Displacement angles of 5, 10, 15, and 20 degrees were tested.

### **2.2.3 Adaptive Exponential Smoothing (Kavvas) Technique**

The Kavvas technique is very similar to the segmentation technique. It is described in Kavvas and Chen (1989). This technique uses the centroid position and line lengths radiating from the centroid to describe the contour. For Kavvas, however, the displacement angle is fixed at 22.5 degrees. Extrapolation is done by an adaptive exponential smoothing procedure which is a weighted least squares fitting procedure with an exponentially discounted weighting factor.

The user was required to set a smoothing coefficient to determine how sensitive the method is to rapid changes in the observations. A small value of the smoothing coefficient puts more emphasis on the older observations, while a large value makes the extrapolation more reliant on newer observations.

#### **2.2.4 Movable Persistence**

This is the simplest of the techniques. Shape and size of the feature are persisted, but the centroid position is extrapolated from the latest position using a linear least-squares regression centroid displacement in previous frames.

After much of the forecast work was done, it was determined that the methodology for defining centroids could be enhanced. Rather than defining a centroid as the average of the contour locations, the centroid was defined as the center of mass. In this way, long, thin features which were not contributing a large amount of volume to the overall contour were not heavily weighted in the centroid position.

As will be explained later, verification scores for movable persistence were found to be erroneous after completion of the forecasts. Corrected movable persistence scores were recomputed for both methods of defining the centroid position. For logistical reasons, scores were only computed for forecasts initialized from the first two frames of the 12-frame sequence of images used in the case selection.

#### **2.2.5 Persistence**

Straight persistence of the last analyzed contour is also included for comparison in the verification statistics. As is discussed in the results section, verification scores for persistence were found to be erroneous for the majority of cases because of a coding error. Corrected persistence scores were recomputed along with those for movable persistence, again only for forecasts initialized from the first two frames of the 12-frame sequence of

images used in the case selection. Comparison with the other techniques is thus restricted to this subsample.

### **2.2.6 Cross - Correlations Technique**

This new technique was introduced to work around the limitations of the contour-based forecast techniques. As discussed in the introduction, all straight contour forecast techniques have the disadvantage of being unable to handle cases where forecast features split, merge, or dissipate. Additionally, an implicit assumption of these schemes is that the important information from a satellite scene can be synthesized into a series of contours. This results in a binary cloud forecast; a point is either inside the contour or outside; actual brightness temperature or rainfall rate is not forecast.

Bellon et al. (1992) describe a possible approach to cloud forecasting, one which can implicitly handle splitting and merging and which does result in a full forecast image of IR pixel brightness values. Judging from the apparent success of this approach, we decided to attempt developing such a scheme at the Phillips Laboratory. A description of the technique and its application to the synoptic scale was described in Atch. 1 (Hamill and Nehr Korn 1993). We review some of the background from that paper below, and point out how the technique is applied differently to the small-scale features used in the contour extrapolation studies.

At the heart of this prototype cloud forecast technique is the derivation of displacement vectors (i.e., "winds") through a cross correlations analysis. First, a subset of pixels from the first image in a satellite loop is chosen. For purpose of illustration in Figure 8, this subset is 8\*8; in our actual prototype scheme, the subset chosen is 15\*15. Next, based on the maximum possible

wind displacement in half an hour, a search radius is chosen, and identically sized subsets of pixels from the second image with centers inside the search radius are correlated against the subset from the first image. If the scene has a uniform cloud layer, then the advective velocity for this layer will be defined by the vector from the center of the subset in Image 1 to the center of the subset with the maximum correlation in Image 2. This is illustrated in Figure 8, and a sample plot of correlation coefficients and a derived displacement vector is shown in Figure 9. In our technique, a cross correlations analysis is repeated at a gridded subset of points throughout the domain, and wind displacement vectors for all points are then derived through an objective analysis. A backwards-in-time trajectory forecast is then used to produce the cloud forecasts.

There are a number of differences in how the technique has been tailored to handle the small-scale features rather than the synoptic-scale. First, the GOES data used in the synoptic-scale forecast experiment was on a  $256 \times 256$  grid, with an approximate resolution of 11 km. For the selection of smaller features to track and forecast, this domain was enlarged to  $512 \times 512$ , halving the effective resolution of the satellite data. Second, the quality control step was modified slightly to throw out any correlation vector with a maximum correlation below 0.75. Subjectively, it was found that this was an effective compromise between eliminating bad displacement vectors and having few wind vectors. Another modification was the use of three iterations in the objective analysis instead of two, with the radius of influence interactively determined from the size of the feature being forecast; the smaller the feature, the smaller the radii of influence, and the greater the detail. Otherwise, the forecast algorithm is identical to the synoptic-scale

algorithm described in the attached conference paper. Figure 10 shows the raw, quality-controlled, and objectively analyzed displacement vectors used to derive the subsequent trajectory forecast for the satellite picture shown in Figure 5.

In addition to the pixel-by-pixel verification of forecast satellite images discussed in the appendix, we also derived computed contours from the cross-correlation forecasts. These contour forecasts were then compared to the contour extrapolation schemes.

### **3. Evaluation of forecast techniques**

#### **3.1. Approach**

Testing of the contour extrapolation techniques posed some special problems, since the testing environment is quite different from the eventual operational environment in which the candidate techniques might ultimately be used. We attempted to make the process of selecting the contour levels and resulting features as objective as possible. Procedures used were designed to guard against the tendency to select only those features that were trackable and resulted in usable cases for the verification statistics. A set of 12 consecutive half-hourly satellite images were loaded for each case selection process. Only the first 6 images were used to select one or more features for tracking and forecasting. The last 6 images were considered to be future verification images not available to the user. The forecasts required at least 3 successive non-splitting, non-merging, and non-dissipating observations - at least 2 observations from the first 6 images for the extrapolation and at least 1 observation from the last 6 images for verification. If successive observations were available only in the first 6 images, the selection was

considered a failure because of a lack of at least 1 verification observation. Though the last 6 images were treated as verification images in the case selection process, observations available from these images were also used to produce forecasts which used more than 6 observations in the extrapolation.

The percentage of case selection failures for each season were: fall - 18%; winter - 26%; spring - 25%; summer - 24%. The fall failure rate is lower because the above case selection criteria were not utilized for this season until after 65% of the cases had been selected. The percentage of splitting, merging, and dissipating contours which caused the above failures were: fall - 42%, 33%, 25%; winter - 47%, 26%, 27%; spring - 35%, 47%, 18%; and summer - 62%, 25%, 13%. It should be noted that even if a case selection was successful by our definition, the selected feature was trackable through all available subsequent image frames in only a minority of cases. The percentage of splitting, merging, and dissipating contours which prevented the use of observations out to the 12<sup>th</sup> image for the successful case selections were: fall (92%) - 36%, 28%, 28%; winter (67%) - 27%, 20%, 20%; spring (69%) - 21%, 23%, 25%; and summer (75%) - 27%, 15%, 33%. On average, the selected features were identifiable in slightly over half of all available frames. The number of frames for each season were: fall - 6.4; winter - 7.6; spring - 7.7; summer - 7.2.

There are a large number of possible combinations of parameters for which verification scores can be computed. We distinguish between two basic types of parameters: characteristics of the cases (size and speed of the features, and the number of previous observations available for forecasting), and extrapolation technique parameters. We chose a subset of all possible combinations, based on the twin objectives of this part of the study: (1)



determination of optimal parameter settings for contour extrapolation techniques, and (2) intercomparison of the four extrapolation techniques, and comparison with other techniques (cross-correlation and persistence). For this control set of cases, sensitivity tests were performed by systematically varying the adjustable parameters of each forecast scheme. We repeated these sensitivity tests for other subsamples of cases to determine whether the results depend on the attributes of the cases (e.g., whether different parameter values give the best results for slow and fast moving features). Based on the results of these tests, optimal parameter value(s) for each scheme were determined. Once the optimal parameter values had been determined, they were held fixed for the remainder of all forecast method intercomparisons (but we allowed different optimal values for different seasons, if appropriate). Forecast method intercomparisons concentrated on the control set of cases, but other samples (i.e., slow and fast features, small and large features) were also used to determine whether the ranking of the methods depends on the case characteristics.

The main verification score used for comparison was the Critical Success Index (CSI), although four others (Probability of Detection - POD, False Alarm Rate - FAR, Bias, and Root mean square error of centroid position - RMSE) were also considered. As illustrated in Figure 11, the scores can be defined as follows:

$$CSI = A / (A+B+C)$$

$$FAR = C / (C+A)$$

$$POD = A / (B+A)$$

$$\text{Bias} = \frac{A + C}{A + B}$$

where A represents the cloud pixels correctly forecast, C represents false alarms (forecast, no verification), and B the misses (verification, no forecast). Scores for CSI, FAR, and POD range from 0.0 to 1.0; a high CSI and POD is desirable, as is a low FAR.

In the following, we discuss the stratification of the statistics by case parameters, and describe the details of the forecast method sensitivity and intercomparison tests.

### **3.2. Stratification of cases**

Cases are characterized by four parameters: observed speed and size of the feature, the number of previous frames available for forecasting, and the forecast increment or lead time. In this definition of "case", each forecast is considered a separate case, whereas in the database each case number refers to all forecasts for a particular feature. We formed three categories each for the size and speed of the features (small; medium; large and slow; moderate; fast, respectively). Selection criteria for these categories were chosen such that between  $1/3$  and  $1/2$  of all cases ended up in the middle categories. The number of previous frames available for forecasting ranges from 2 to 11, and the forecast increment ranges from 1 to 6 frames ( $1/2$  to 3 hours). The control set of cases (CONTROL) consisted of all cases with:

- size: medium or large
- speed: slow, moderate, or fast
- number of previous frames: any number between 2 and 11.

That is, all cases except those with small features are included in CONTROL. Small features were excluded to eliminate features that are less likely to be of meteorological significance. For an examination of how much the results depend on the case characteristics, we also considered samples for which one of three case parameters is varied from CONTROL. The total number of samples is summarized in the following table:

Table 1: Case parameter values of samples (sets of cases) used for forecast method testing and verification.

Name	Size	Speed	Previous Frames
CONTROL	medium,large (CONTROL)	slow, moderate, fast (CONTROL)	2 - 11 (CONTROL)
SMALL	small	CONTROL	CONTROL
LARGE	large	CONTROL	CONTROL
SLOW	CONTROL	slow	CONTROL
FAST	CONTROL	fast	CONTROL
PRE2	CONTROL	CONTROL	2
PRE4	CONTROL	CONTROL	4
PRE6	CONTROL	CONTROL	6

The above table represents a total of 8 samples. For each sample, all available lead times were considered. Because of the limited lifetime of features and limitations on the number of frames available for case selection, not all combinations of number of previous frames and forecast increments are present for each feature. Thus, sample size and composition are not the same for different forecast increments - this is acceptable since the crucial intercomparison is between different methods and forecast parameter settings, at each forecast increment, not between different forecast increments.

The distribution of size and speed of the features was examined in detail for the fall season. Sizes for the 53 features span more than 2 orders of magnitude (52 to 9100 km<sup>2</sup>). When plotted on a semi-logarithmic plot, the distribution is bimodal, with one peak at fairly small sizes (ca. 200 km<sup>2</sup>), and one just above the median (ca. 500 km<sup>2</sup>). Some percentiles are shown in Table 2:

Table 2: Distribution of feature sizes for the fall season

	rank	size (km <sup>2</sup> )		rank	size (km <sup>2</sup> )
1/6:	9	95	5/6:	45	1990
1/4:	13	152	3/4:	41	1224
1/3:	18	207	2/3:	35	661
1/2:	27	433			
(median)					

We used cutoff values corresponding to the approximate  $1/4$  -  $3/4$  thresholds, and roughly centered around the median (on a logarithmic scale):

small (11 features): features no larger than  $150 \text{ km}^2$   
 large (13 features): features larger than  $1200 \text{ km}^2$

Use of these thresholds removes only the very smallest features from the CONTROL sample, leaving a sufficient number to allow the further stratifications indicated in Table 1.

Speeds have a unimodal distribution which is skewed towards slow speeds, and a long tail at high speeds. Some percentiles of the 53 fall features are shown in Table 3:

Table 3: Distribution of translation speeds for the fall season

	rank	speed (km/h)		rank	speed (km/h)
$1/6$ :	9	55	$5/6$ :	45	135
$1/4$ :	13	60	$3/4$ :	41	113
$1/3$ :	18	68	$2/3$ :	35	105
$1/2$ :	27	88			
(median)					

When all the small features are excluded, the distribution with speed for the remaining cases is modified as follows:

Total number of cases: 42  
Median: Rank=21.5 Speed=89 km/h

To assure sample sizes of at least 10 for the SLOW and FAST samples, we used approximate  $1/3$  -  $2/3$  cutoffs centered around the median value:

slow (14 features): features with speeds no faster than 70 km/h  
fast (12 features): features with speeds faster than 110 km/h

For the winter season, the size and speed distributions of the features were similar. The total number of 52 cases were subdivided into small, large and medium features according to the following cutoff values:

small (11 features): features no larger than 250 km<sup>2</sup>  
large (11 features): features larger than 1000 km<sup>2</sup>

After removal of the small features, the remaining 41 features were further subdivided into slow, moderate, and fast speeds according to the following cutoff values:

slow (15 features): features with speeds no faster than 80 km/h  
fast (12 features): features with speeds faster than 120 km/h

For spring and summer, scores were only computed for the control sample (examination of the results by subsample revealed no significant differences between the fall and winter seasons). We used a cutoff of 250 km<sup>2</sup> (225 km<sup>2</sup>) for the small cases for spring (summer), eliminating 10 (13) features from the total sample of 52 (51), leaving 42 (38) features in the control sample.

### **3.3. Sensitivity tests**

#### **3.3.1. Whole Contour Method:**

There are three separate tunable parameters for this technique: the number of Fourier modes used for prediction (frequency), the type of forecast method, and the order of extrapolation. However, previous experimentation has already established linear extrapolation (order=1) as the optimal choice. The remaining two parameters have the following possible values:

frequency: 1 - 5  
method: 2, 3, or 4

The verification scores for the CONTROL sample for fall are displayed in Figure 12 for all values of frequency for method 2. The corresponding scores for method 3 and 4 are shown in Figures 13 and 14. The sample sizes for the CONTROL sample range from 499 (increment 1), 337 (increment 2), 207 (increment 3), 114 (increment 4), 60 (increment 5), to 22 (increment 6). A striking feature of the plots of the Critical Success Index (CSI) is the insensitivity of the results to frequency. Close examination reveals, however, that for all methods, for all increments, best CSIs are obtained for frequency=1 (with one exception, where frequency=2). For those frequency values, CSI is completely insensitive to method. This conclusion also applies to the probability of detection (POD), false alarm rate (FAR), and the bias. The rms error of the centroid position (RMSE) is insensitive to frequency and method.

It is somewhat surprising that using only one frequency mode, i.e., approximating the shape of any cloud feature selected for tracking by an ellipse, results in better forecasts than retaining and predicting higher

wavenumbers. It indicates that there is no skill, at least using the approaches tried with the whole contour method, in predicting any but the grossest scales of cloud features.

Figures 15 and 16 show the CSI and RMSE for the LARGE and SMALL subsamples, respectively (because there is essentially no sensitivity to the forecast method, only results for method no. 2 are shown in these and all following figures). Results agree qualitatively with those for the CONTROL sample, as do those for the SLOW and FAST samples (Figures 17 and 18) and the samples with 2, 4, or 6 previous frames (PRE2, PRE4, and PRE6), corresponding to Figures 19, 20, and 21. Sample sizes for the subsamples are substantially smaller than for CONTROL, ranging from 100 - 200 at increment 1 to 5 - 15 at increment 6; sample sizes for the PRE4 and PRE6 subsamples are even smaller, with no cases for the longer increments.

For the purposes of forecast method intercomparison, we chose an optimum parameter setting based on the results described above of frequency=1, and method = 2 (although any one of the three methods (2, 3, or 4) would give the same results).

Comparing skill between subsamples gives some interesting results. CSI values increase with the size of the feature (they are higher for LARGE than for CONTROL, and smaller for SMALL than for CONTROL). The RMSE are much smaller for small features, but in light of the extremely small CSI (0.2) the overall forecast skill for small features must still be judged poor; LARGE and CONTROL RMSEs are roughly comparable, with a tendency towards smaller errors for large features. Both measures of skill improve as the speed of the feature decreases (values for the SLOW sample



are better than those for CONTROL, which in turn are better than those for the FAST sample). There is no clear dependence of the CSI or RMSE skills on the number of previous frames. This is not surprising, since only the previous 2 frames are used for forecasting in our linear extrapolation technique.

Results for the other three seasons are shown in Figures 22, 23, and 24 for the control sample. The lack of sensitivity to the number of modes is evident in these seasons as well. CSI scores tend to be slightly higher in fall and winter than spring and summer, particularly at longer forecast increments.

### **3.3.2. Segmentation Method**

The only tunable parameter for this technique is the segmentation angle, which was varied from  $5^\circ$  to  $20^\circ$  in increments of  $5^\circ$  (a total of 4 values).

Skill scores for the CONTROL sample for fall are shown in Figure 25. There is very little sensitivity with respect to the segmentation angle in either the CSI or the RMSE, with some suggestion that neither the minimum nor the maximum value ( $5^\circ$ ,  $20^\circ$ ) is optimal. The POD generally decreases with increasing segmentation angle, whereas the FAR and the bias is largest at the smallest angle, but nearly constant otherwise for most forecast increments. Thus, the higher values of POD at smaller segmentation angles come at the expense of overforecasting. The RMSE is quite insensitive to the segmentation angle, aside from increment 6, where minimum values are for segmentation angles of  $10^\circ$  and  $15^\circ$ .

The lack of sensitivity to the segmentation angle indicates that for this technique, as was found for the whole contour technique, there is no skill in predicting small scale features of the selected contours. Visual inspection of segmentation forecasts revealed that smaller segmentation angles not only fail to improve the verification scores, but also result in highly unrealistic contour shapes. Since adjacent segment lengths are forecast independently from one another, the forecasted contours can contain long, thin protrusions, and bear no resemblance to meteorological features. Since the area enclosed by these protrusions is small, however, the skill scores are not degraded significantly for these unrealistic contour forecasts. This results in deceptively good scores in some cases.

The results for the SLOW and FAST subsamples (Figures 26 and 27) are qualitatively similar to those for the CONTROL sample. The LARGE sample results (Figure 28) also confirm the results of the CONTROL sample, whereas the SMALL sample (Figure 29) indicates better results for larger angles (15 or 20 degrees).

We chose a value of 15° as the optimal parameter setting for the purpose of forecast method intercomparison based on these results.

The differences in skill scores between the subsamples mirror those discussed previously for the whole contour method. In particular, skill increases with increasing size and decreasing speed of the feature, and shows no systematic dependence on the number of previous frames available for forecasting (Figures 30 - 32; recall that the segmentation method also only uses the previous 2 frames for a linear extrapolation).

Results for the other three seasons are shown in Figures 33, 34, and 35 for the control sample. The lack of sensitivity to the segmentation angle is evident in these seasons as well. CSI scores tend to be slightly higher in fall and winter than spring and summer, particularly at longer forecast increments, as was seen in the whole contour technique.

### **3.3.3. Kavvas Method:**

The only tunable parameter for this technique is the smoothing coefficient, which was varied from 0.10 to 0.50 in increments of .05.

For the CONTROL sample for fall (Figure 36), the CSI, POD, and FAR all indicate increasing skill with increasing smoothing coefficient for forecast increments less than 3. At longer forecast increments, optimal values are less than at shorter increments ( .5 for increments 1 and 2, .35 and .4 for increments 3-6). The bias is smallest for smoothing coefficients of .4 to .5 for short increments (1-3), whereas it increases monotonically with smoothing coefficient for longer increments. The RMSE indicates smallest errors for smoothing coefficients in the range .25 to .35, for all forecast increments.

The sensitivity of the CSI and RMSE with respect to the smoothing coefficient are similar for the SLOW and FAST subsample (Figures 37 and 38). However, optimum values are slightly larger for fast features, at least in terms of the RMSE (.3 to .4, vs. .25 to .35). The SLOW subsample shows just the opposite, with optimum values slightly lower (.3 to .45 for CSI, .15 to .25 for RMSE for increments > 1).

The SMALL and LARGE subsample (Figures 39 and 40) indicate similar opposing sensitivities: CSI for small features increase with smoothing

coefficient (optimum values  $> .5$ ), for large features optimum values are .3 to .45. The RMSE for large features indicates optimum values of .2 to .25, whereas in the SMALL subsample optimum values range from .15 for increment 1 to .45 for increment 6.

There are no striking differences in sensitivity for the pre2, pre4, or pre6 subsamples (Figures 41 - 43).

In contrast to the other two techniques, skill scores show a much greater sensitivity to the tunable parameter of the technique. In theory, this might present an opportunity for optimization of the technique; in practice, however, it will complicate its implementation. Choosing an overall optimum value for the forecast method intercomparison is difficult for the Kavvas technique, since different optimum values exist for the different increments, subsamples, and measures of skill. However, it is possible to choose one value that results in scores that are not too different from the optimum score for any increment, for either CSI or RMSE. We selected an optimum value of .40 based on the results of the CONTROL sample. This value is also close to the optimum values for the LARGE and SLOW subsamples. For the SMALL and FAST subsamples it is decidedly suboptimal, particularly at short forecast increments; however, since the CSI skill for these subsamples is low for any value of the smoothing coefficient, this is not a serious problem.

As was the case in the other two techniques, CSI scores are generally higher for larger features, and RMSE errors tend to increase with feature size. For smoothing coefficients at the respective optimum values, CSI and RMSE scores tend to improve as the speed decreases.

Comparison between the PRE2, PRE4, and PRE6 subsamples indicates no clear advantage of having a longer time history on which to base the prediction.

Results for the other three seasons are shown in Figures 44, 45, and 46 for the control sample. The sensitivity to the smoothing coefficient is similar in these seasons. Because in the winter sample slightly better scores are obtained for larger values of the smoothing coefficient, we used an optimum value of .45 for winter for subsequent method intercomparisons. In spring and summer, we used the same value as in fall (.40).

### **3.4. Forecast method intercomparison**

#### **3.4.1 Intercomparison of three contour extrapolation techniques**

Figure 47 shows a direct comparison of the skill scores for the CONTROL sample for fall of the contour extrapolation methods, using the optimum values selected above (whole contour: method=2, frequency=1; segmentation: angle=15°; Kavvas: smoothing coefficient = 0.4). Also shown are the sample sizes for the different forecast increments and techniques (sample sizes for the different techniques are not exactly the same because the extrapolation algorithms failed for some cases for one of the techniques, but not the others; these differences in sample size are small enough, however, to avoid influencing the results). It can be seen that the segmentation technique is superior overall in terms of CSI and POD; its FAR is slightly inferior to the whole contour method at larger increments, and its bias is worse than that of both other methods. The Kavvas is inferior to both methods in terms of CSI, POD, and FAR; its bias, however, is the smallest of any of the forecast methods. Thus, the segmentation method tends to

overforecast more than whole contour, but the improved POD more than makes up for it in the CSI, and the Kavvas method is overall inferior by any measure except bias. In terms of the RMSE, the segmentation method is better at most increments than the whole contour RMSE, and the Kavvas method is by far worse than the other two methods.

The relative ranking in terms of CSI and RMSE of the three methods is the same in the CONTROL, SLOW, FAST, LARGE and SMALL subsamples (Figures 48, 49, 50 and 51): the segmentation is best, followed by the whole contour method, with Kavvas a distant third (particularly in terms of RMSE).

Results for the other three seasons confirm the conclusion that the segmentation method is the best of the three contour extrapolation methods considered so far (Figures 52, 53, 54). The relative ranking of the three techniques for all the measures of skill is the same for fall, winter, and spring. In summer, the Kavvas method is second to segmentation, ahead of the whole contour method, mainly because its FAR in that season is better when compared to the other techniques.

#### **3.4.2. Significance Testing and comparison with other techniques**

We performed a statistical analysis on the forecast method intercomparison to assess the statistical significance of the results. We separately considered each score for each forecast increment. An analysis of variance (ANOVA; see Neter and Wassermann, 1974, hereafter referred to as NW) was performed on the raw verification scores, using the Splus statistical package (Chambers and Hastie, 1992). Because there is substantial variability of the forecast score from one case to the next for each of the

methods, we considered the forecast method a treatment factor, and the case number a blocking factor. Different forecasts produced for the same case number were grouped together under each case number. The treatment factor (forecast method) is a fixed effect, since the methods were chosen beforehand for their intrinsic interest, whereas the blocking factor must be considered a random effect, since the cases are a sample from a larger population. For this analysis we eliminated all cases that did not have scores for all forecast methods available, so that a complete block design resulted (all methods were tested for each of the blocks, i.e. cases). With this experimental design, tests for the presence of block and treatment effects are performed using a two-way ANOVA (NW, p. 474 and p. 730). In the presence of treatment effects, the confidence interval for all pairwise comparisons between treatment means (i.e., mean scores for the different forecast methods) can be computed using the Tukey confidence intervals (NW, p. 474 and p. 730). Results from this analysis are presented below. Assumptions underlying these significance tests are that the residuals are normally distributed random variables (residuals are the deviations of the actual scores from the means for the method and case number), and that the mean scores for the cases are normally distributed random variables.

We first applied the ANOVA to a comparison of the three contour extrapolation techniques with persistence and movable persistence. As was discussed in sections 2.2.4 and 2.2.5, scores for persistence and movable persistence were only available for forecasts initialized from the first two frames of the 12-frame sequence of images used for case selection. We further restricted the analysis to those forecasts where a verification score was available for each forecast technique. This resulted in much smaller

sample sizes than those used in the method intercomparisons of the previous section: 58 cases (at increment 1) to 31 cases (at increment 5), from the forecasts for all four seasons. The results shown in Figure 55 confirm the conclusion of the previous section that the segmentation technique is the best of the three extrapolation techniques (it is significantly better at the 5% level than any other scheme only for increment 1). In addition, it is significantly better than persistence (at the 5% level of statistical significance) at all forecast increments. Movable persistence based on the center of mass is best overall, and significantly better than persistence at all forecast increments. The differences between the two movable persistence methods and the segmentation technique are not statistically significant at any increment computed from this sample.

An examination of the sample used for the intercomparison revealed that the whole contour technique accounted for the majority of missing forecast scores. The reason for these missing scores is not entirely clear without further investigation. Since the results so far indicate none of the three contour techniques are candidates for technology transition, this problem was not investigated further; instead, it was circumvented by deleting the whole contour technique from the intercomparison. This resulted in roughly doubled sample sizes (140 cases of increment 1 to 71 cases at increment 5), and correspondingly tighter confidence intervals. As is shown in Fig. 56, the movable persistence based on the center of mass has significantly better CSI scores than the segmentation technique at all forecast increments (the difference between the two movable persistence scores is still statistically insignificant). Interestingly, its POD scores are



lower than those of segmentation, but this is more than compensated by lower (better) FAR scores.

Finally, we compared contour forecasts produced by the cross-correlation technique with those of movable persistence (again based on the center of mass) for 40 cases (10 from each season). To simplify the computations, we used a slightly different verification procedure in this comparison than in the other contour forecasts. In cases where more than one contour of the selected contour level exists in the scene, we treat all pixels enclosed by those contours as cloudy, and all others as clear; previously, only pixels within the one contour selected for forecasting were considered cloudy. For the movable persistence, the centroid position is still defined in terms of the contour selected for forecasting. The results from this comparison (Figure 57) show that the cross-correlation forecasts have equal or greater skill than movable persistence at all forecast increments. Out to one hour, they are significantly better.

#### **4. Summary of results and recommendations**

The exhaustive testing of the contour extrapolation techniques resulted in several important findings:

- 1) Identifying, tracking, and forecasting features of interest on satellite imagery through contours of brightness temperature is successful in only a minority of cases. On average, contours selected for forecasting either split, merged, or dissipated after three to four hours. Contours remained intact to the end of the six hour sequence of satellite images used in our study in only 8% to 33% of the cases, depending on the season.

2) There is no measurable skill in predicting anything but the position of contours. Attempts at predicting smaller scale features (i.e., shape) did not improve verification scores, and resulted in unrealistic forecast contour shapes. In the case of the segmentation and Kavvas techniques, adjacent segment line lengths are predicted independently from one another, resulting in forecast contours with long, pointed protrusions.<sup>1</sup> In the case of the whole contour technique, the most skillful forecasts (in terms of verification scores) were those with ellipsoidal contours.

3) Consistent with point 2) above, the most skillful contour extrapolation technique is movable persistence, in which the contour shape is persisted, and the centroid position (based on the center of mass of the area enclosed by the contour) is extrapolated based on its past movement. Its verification scores, along with those of the segmentation technique, are significantly better than persistence for forecasts from 1/2 to 2 1/2 hours in advance.

4) The most generally applicable technique for producing short-term forecasts from satellite imagery is the cross-correlation technique developed in this project. Pixel-based verification of the cross-correlation forecasts show an improvement against persistence out to 2 1/2 hours (the longest time period studied for this technique). Contour forecasts derived from the cross-correlation were significantly more skillful than those of the best contour

---

<sup>1</sup>Because these protrusions cover only a small area, these unrealistic contour shapes are not always accompanied by lower objective skill scores.

extrapolation technique (movable persistence) out to 1 hour, and no worse out to 2 1/2 hours.

The above findings could possibly be altered if algorithmic improvements to the contour extrapolation were explored (e.g., considering segment line lengths together, not independent from one another). However, because of the overall failure rate of contour techniques, it is recommended that the cross-correlation technique developed in this project be considered for technology transition to AWDS. It requires only limited data (two frames of IR satellite imagery spaced 1/2 hour apart) and modest computer resources. It will produce a forecast satellite image under all conditions, and requires minimal human intervention. Its skill has been demonstrated by comparison to simple persistence in terms of pixel grayshade values, and against the best contour extrapolation scheme in terms of contour forecasts. It was found to yield the greatest improvement over persistence in cases dominated by advection; in convective situations, its inability to handle development and dissipation led to smaller improvements over persistence. For situations in which contour-based forecasts are useful (well-defined, long-lived, isolated features), and when the additional forecaster time required for selection of contour levels is acceptable, one may in addition consider including the movable persistence contour extrapolation scheme as a candidate for transition. Although its skill was found to be inferior to that of the cross-correlation scheme, its computational simplicity makes it an attractive option.

## **5. References**

- Bellon, A., A. Kilambi, G. L. Austin, and M. R. Duncan, 1992: A satellite and rainfall observation and forecast system. *Preprints, 8th AMS Interactive Information and Processing Systems Conference*, pp. J110-J-116.
- Bianco, A. and H.-C. Huang, 1990: Satellite and radar forecast techniques for short-term prediction of storm motion on the Remote Atmospheric Processing and Display system (RAPID). GL-TR-90-0179, Geophysics Laboratory, Hanscom AFB, MA 43 pp, ADA261190
- Bohne, A. R., F. I. Harris, P. A. Sadoski, and D. Egerton, 1988: Short term forecasting of cloud and precipitation. Air Force Geophysics Laboratory Technical Report, AFGL-TR-88-0032, 94pp. ADA212692
- Chambers, J.M., and T. J. Hastie, 1992: Statistical Models in S. Wadsworth and Brooks, Pacific Grove, CA, 608 pp.
- Clark, J. D. ed., 1983: The GOES User's Guide. U.S. Department of Commerce, Washington, D. C.,
- Hamill, T. M., and T. Nehrkorn, 1993: A short-term cloud forecast scheme using cross-correlations. *Preprints, 9th AMS Interactive Information and Processing Systems Conference*, 6 pp.
- Heideman K. F., H.-C. Huang, and F. H. Ruggiero, 1990: Evaluation of a nowcasting technique based on GOES IR satellite imagery. *Preprints, 5th AMS Conf. Satellite Meteor. and Ocean.*, London, England, 366-371.
- Kavvas, M. L., and Z. Chen 1989: The radar-based short-term prediction of the time-space evolution of rain fields. GL-TR-89-0103, Geophysics Laboratory, Hanscom AFB, MA, 18 pp, ADA213802.

Neter, J., and W. Wassermann, 1974: Applied Linear Statistical Models.

Richard D. Irwin, Inc., Homewood, IL, 842 pp.

Ruggiero, F. H., K. F. Heideman, and J. Doherty, 1991: An evaluation of three techniques for nowcasting precipitation fields using weather radar. *Preprints, 25th AMS Conf. Radar Meteor.*, Paris, France, 83-86.

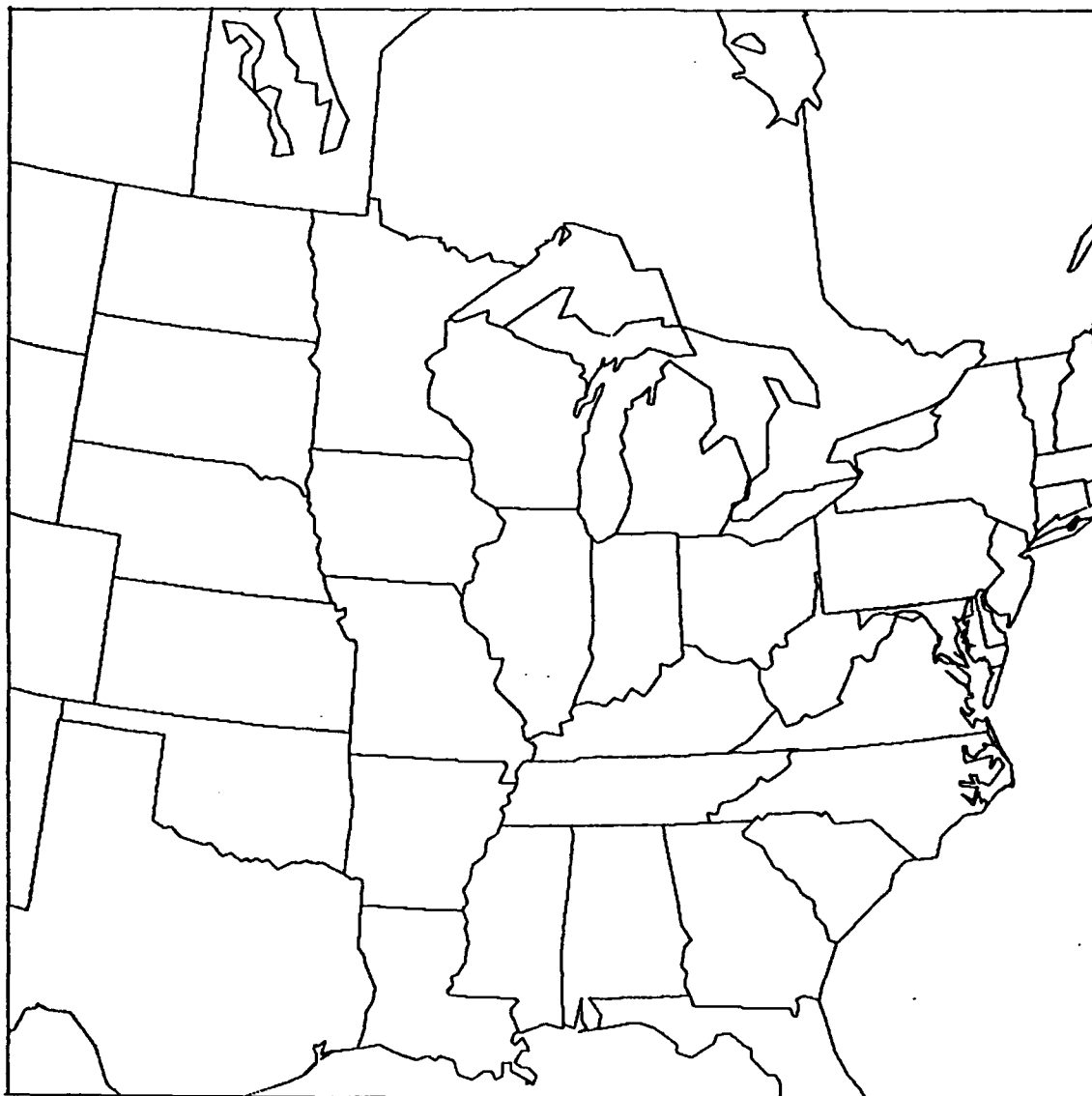


**Figure 2: Domain used in testing the cloud forecast techniques. The domain is a Lambert-conformal projection true at 30 and 60 N.**



**Figure 3: A sample frame of raw GOES IR imagery remapped to the Lambert conformal projection. Map overlay is not included here, but the domain corresponds to the one shown in Figure 2. The imagery was from 1500 UTC 20 Nov 1991.**

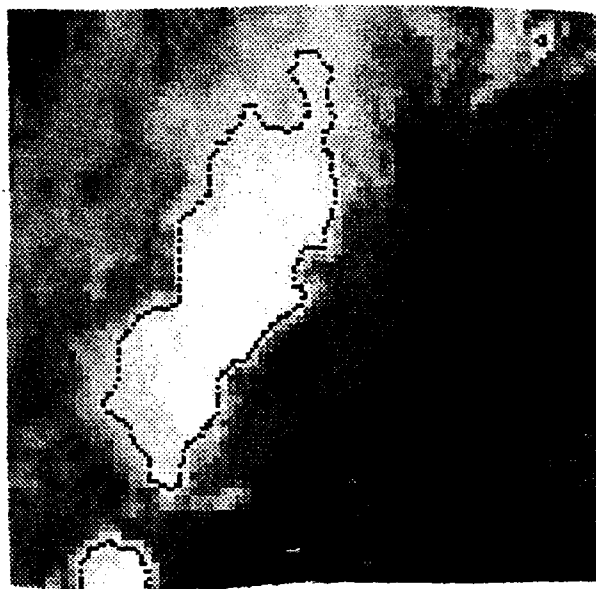


**Figure 4:** A subframe of GOES imagery taken from 3, with contours overlaid for pixel brightness 181.

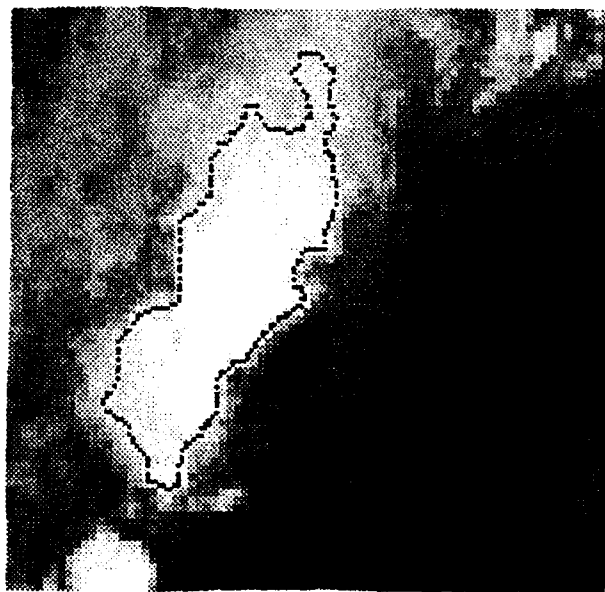


**Figure 5:** The same subframe of GOES imagery as shown in Figure 4, but after the selection of the one feature for tracking and deletion of all other features.



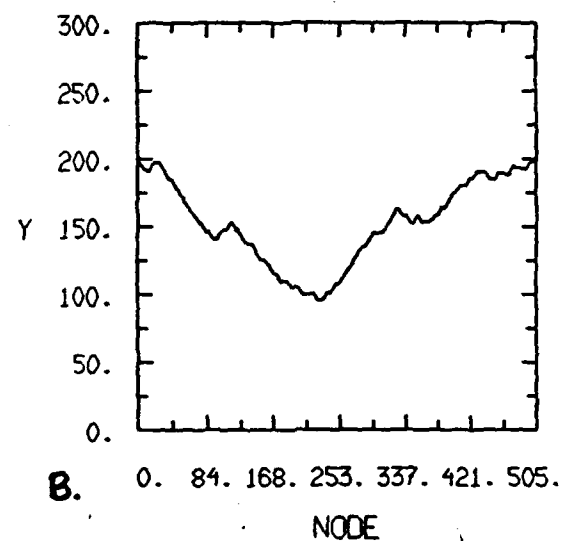
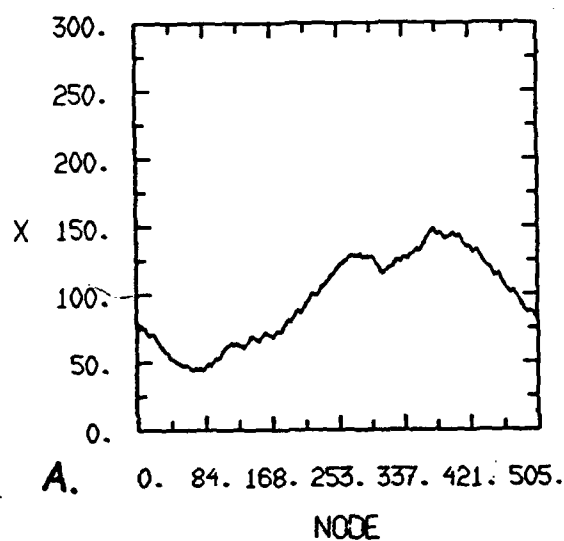
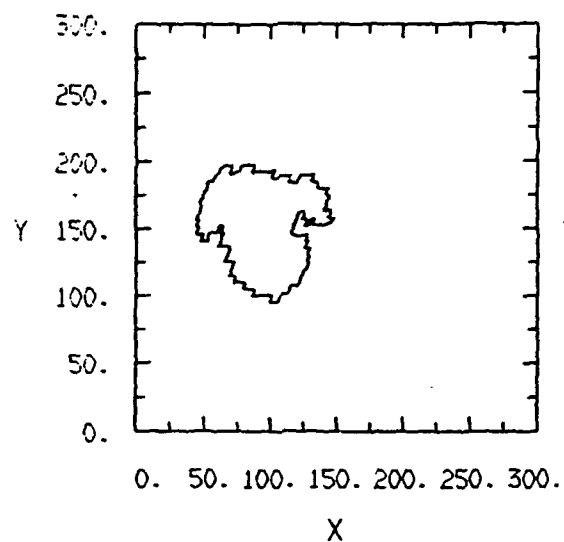


**Figure 6:** Illustration of a sample contour (a) and the decomposition into x- and y- coordinates (b) (from Bianco and Huang 1990).

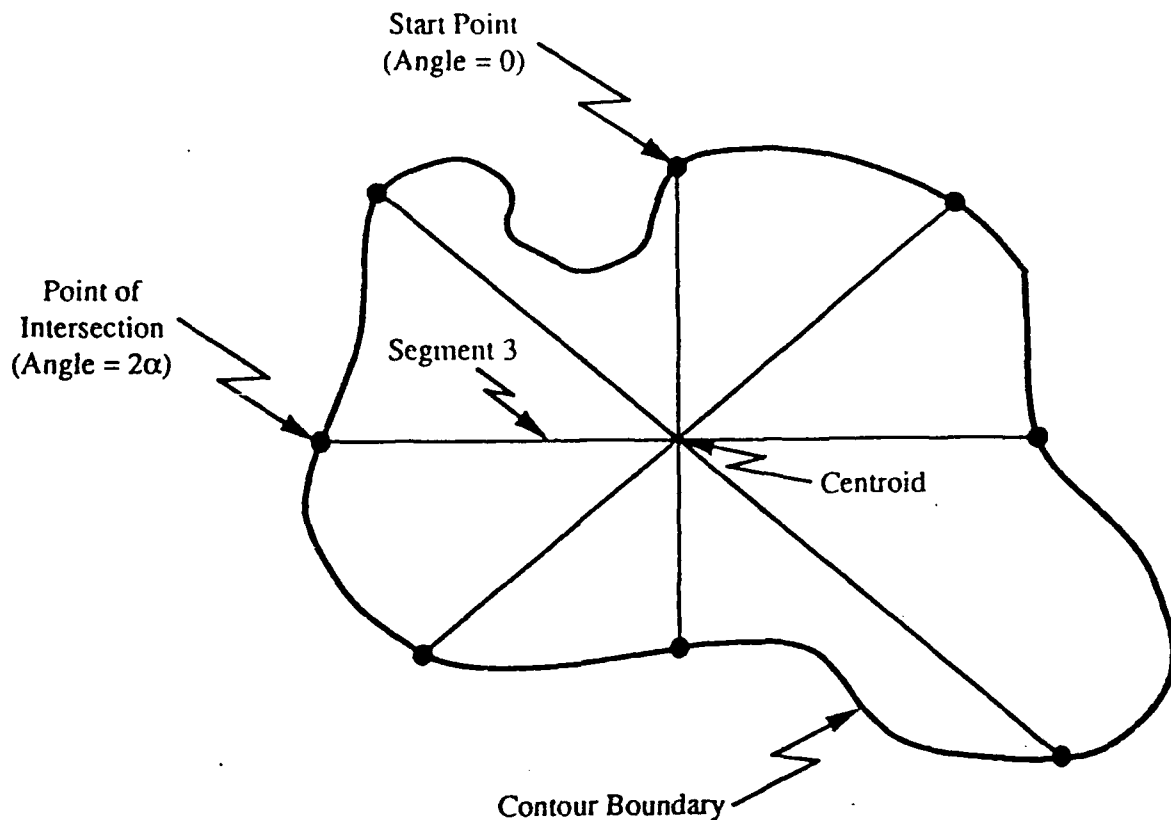


Figure 7: Illustration of the concept of defining a contour using a centroid and a set of line lengths radiating from the centroid.

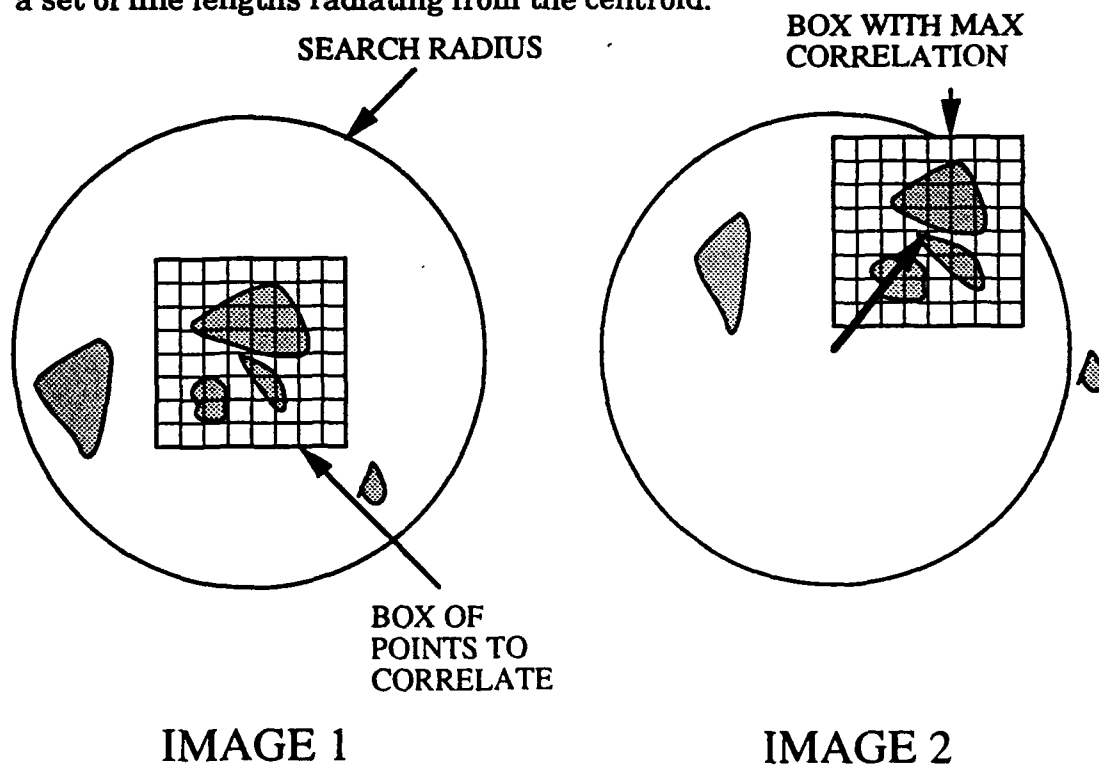


Figure 8: Illustration of correlation analysis and derivation of the displacement vector. The displacement vector is directed from the center of the correlation box in Image 1 to the center of the correlation box in Image 2 most highly correlated with Image 1.

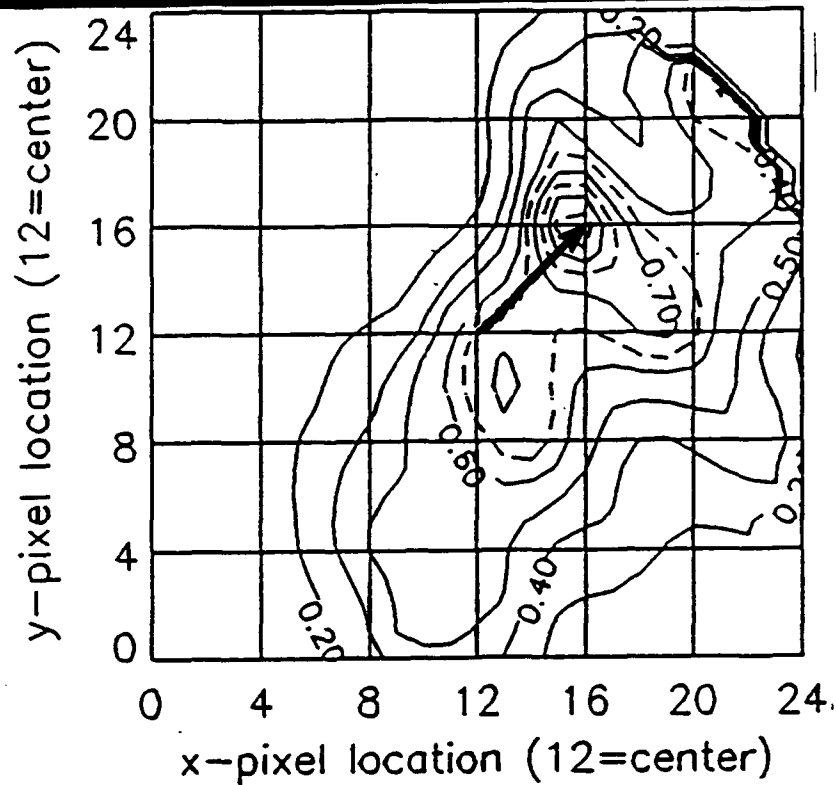


Figure 9: Example of a correlation field used in the derivation of a displacement vector. The point (12,2) is the center of the original correlation box. The displacement vector originates at this point and ends at the point with the highest correlation.

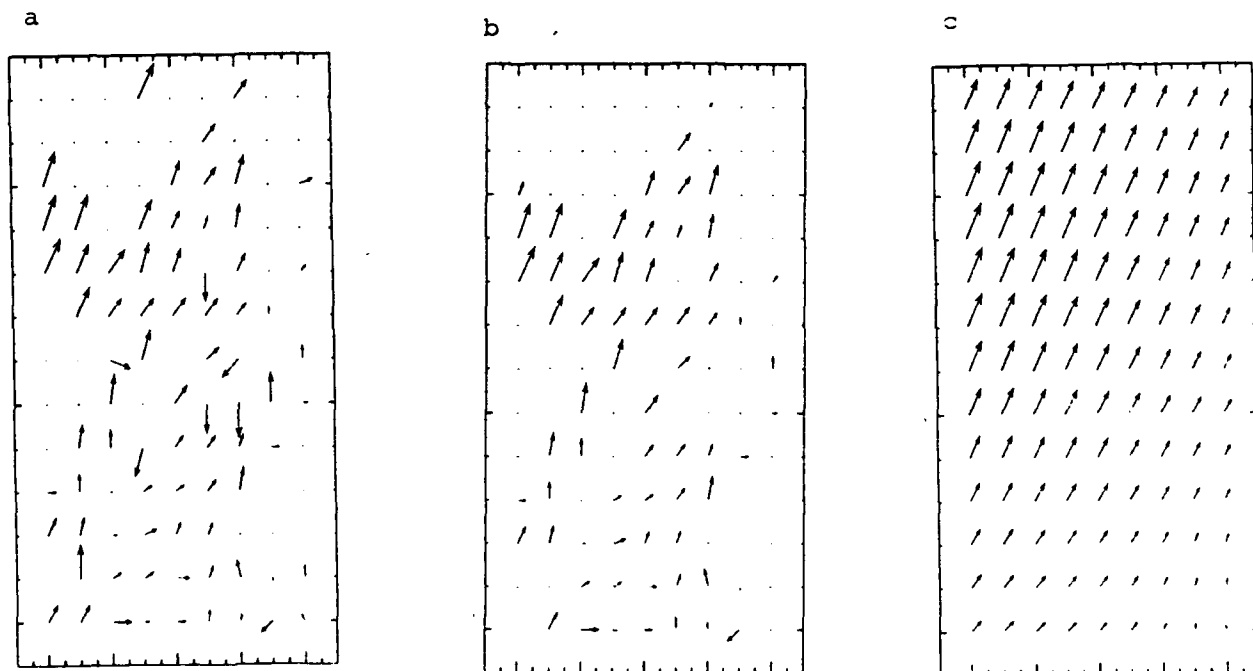
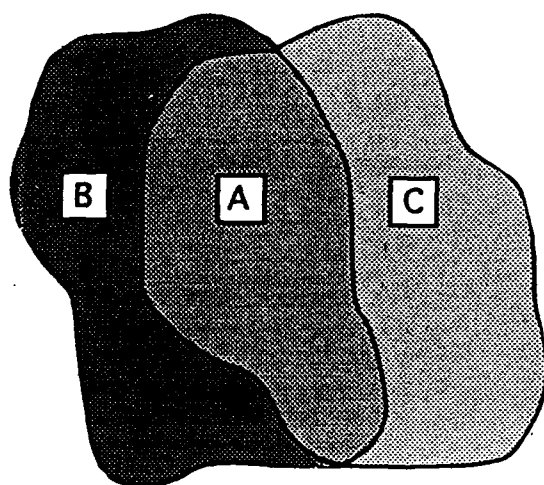


Figure 10: (a) Raw displacement vectors, (b) displacement vectors after a quality control, and (c) objectively analyzed displacement vectors for the same satellite scene as shown in Figure 5.



**Figure 11:** Illustration of two contours bounding a forecast area ( $A+C$ ), and a verification area ( $A+B$ ), and the breakdown into regions of hits ( $A$ ), misses ( $B$ ), and false alarms ( $C$ ).

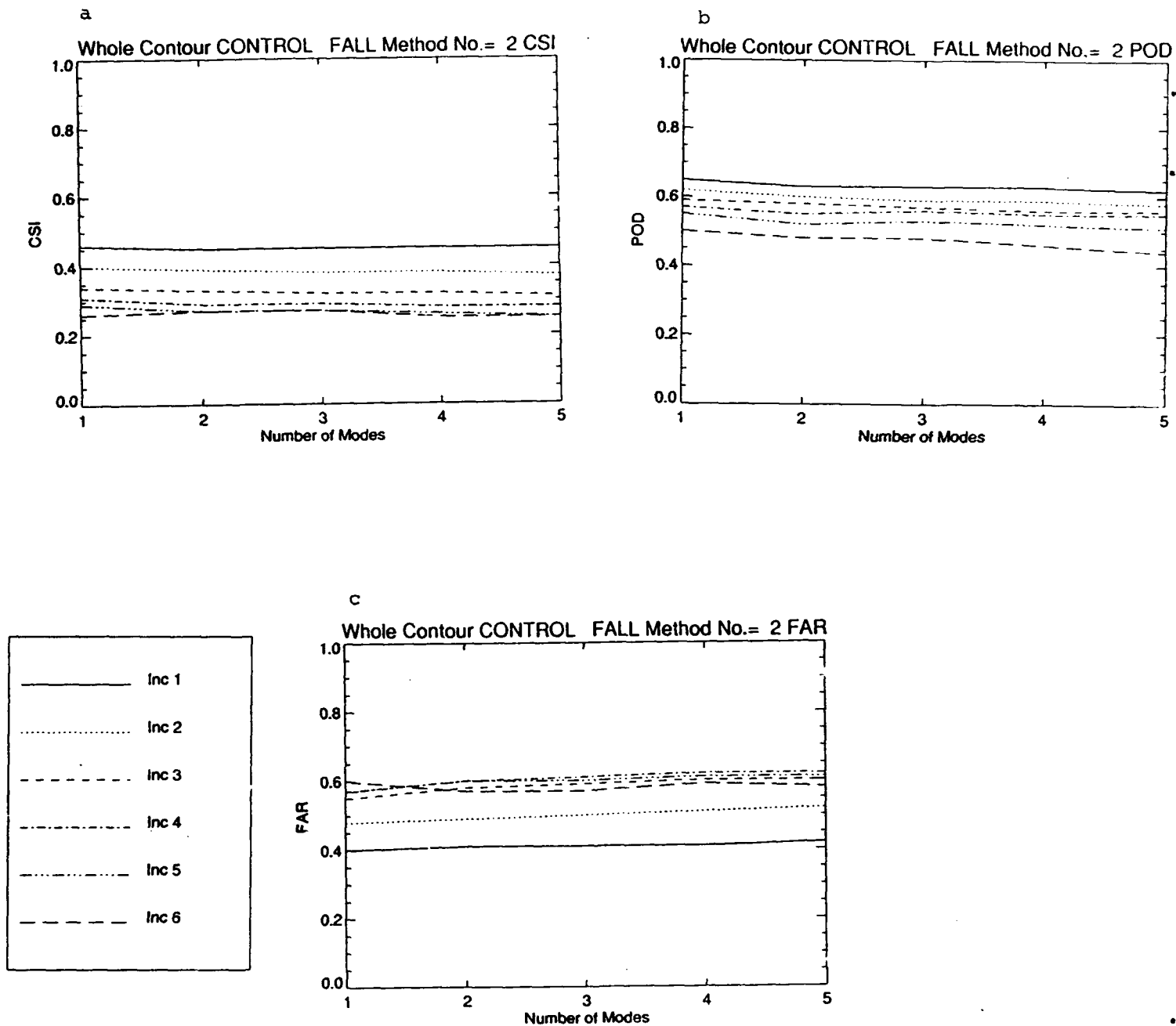


Figure 12: Verification scores for the CONTROL sample for fall, for the whole contour method with method number = 2. Shown are CSI (a), POD (b), FAR (c), BIAS (d), and RMSE (e) as a function of frequency (number of modes). The different lines correspond to different forecast increments: increment 1 (solid), increment 2 (dotted), increment 3 (short dashes), increment 4 (dash-dot), increment 5 (dash-dot-dot-dot), and increment 6 (long dashes).

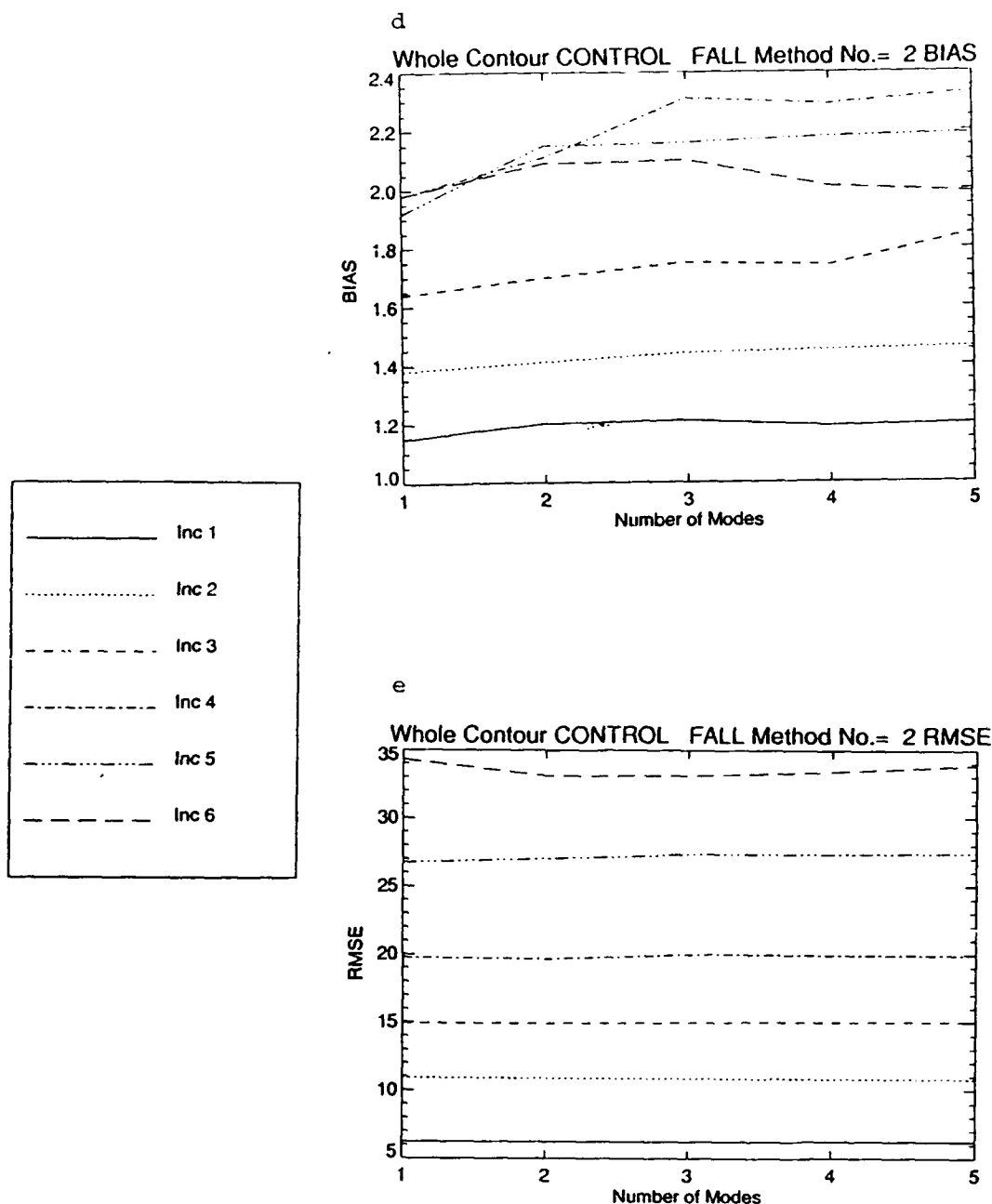


Figure 12: Verification scores for the CONTROL sample for fall, for the whole contour method with method number = 2. Shown are CSI (a), POD (b), FAR (c), BIAS (d), and RMSE (e) as a function of frequency (number of modes). The different lines correspond to different forecast increments: increment 1 (solid), increment 2 (dotted), increment 3 (short dashes), increment 4 (dash-dot), increment 5 (dash-dot-dot-dot), and increment 6 (long dashes).

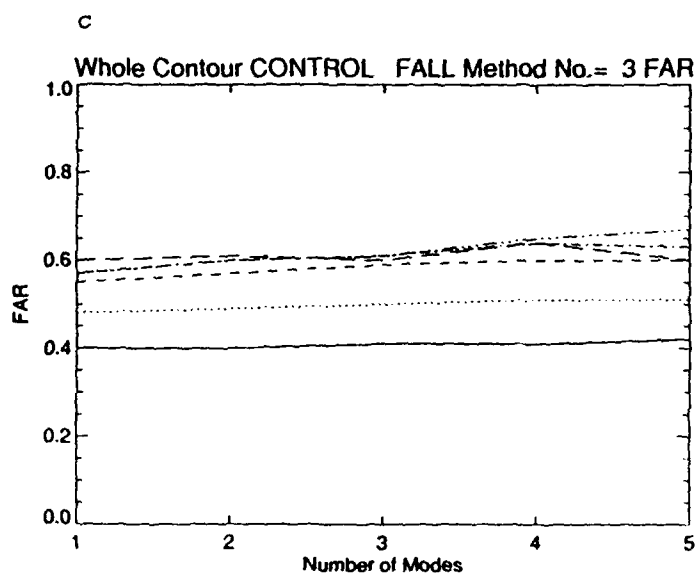
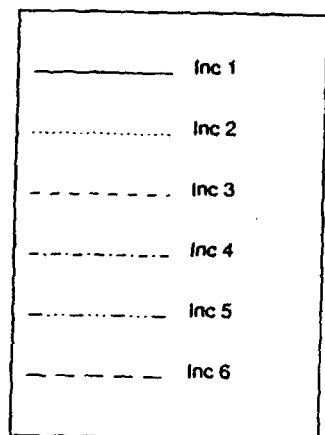
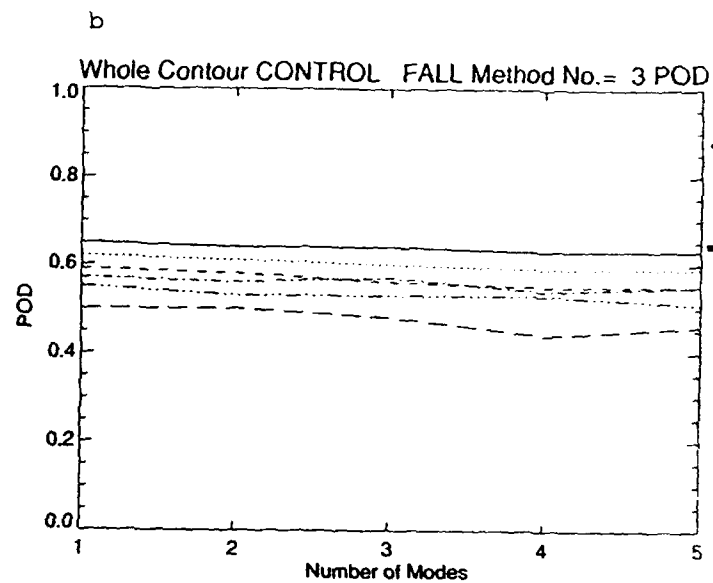
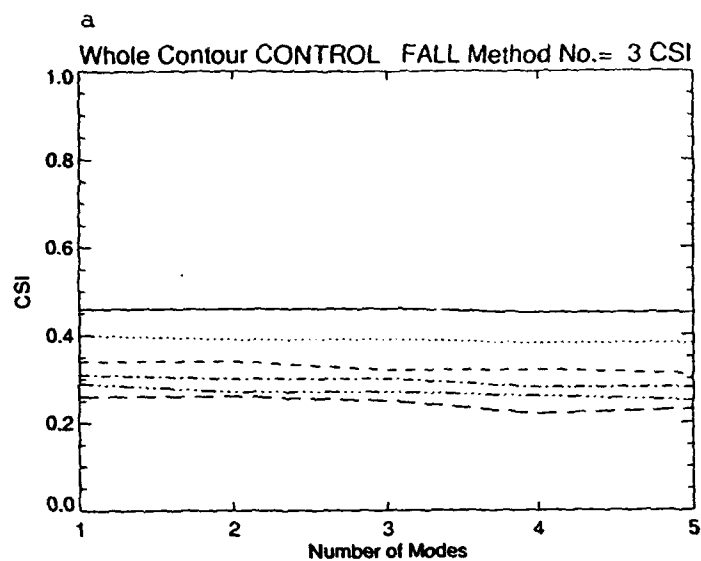


Figure 13: Same as Figure 12, except for method number = 3.

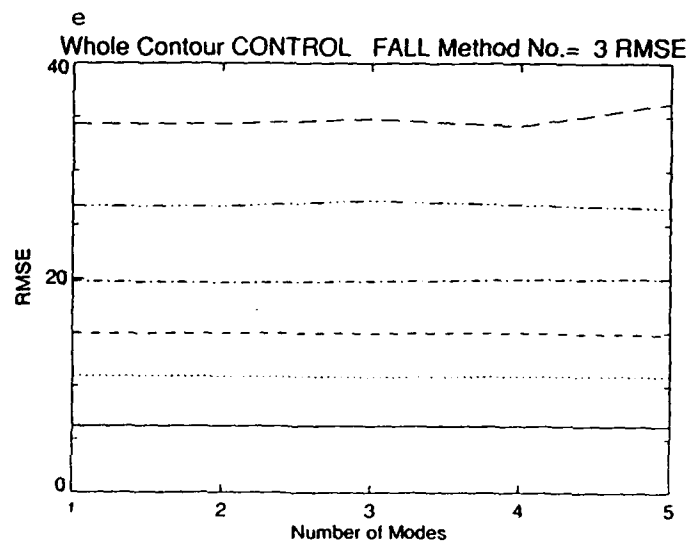
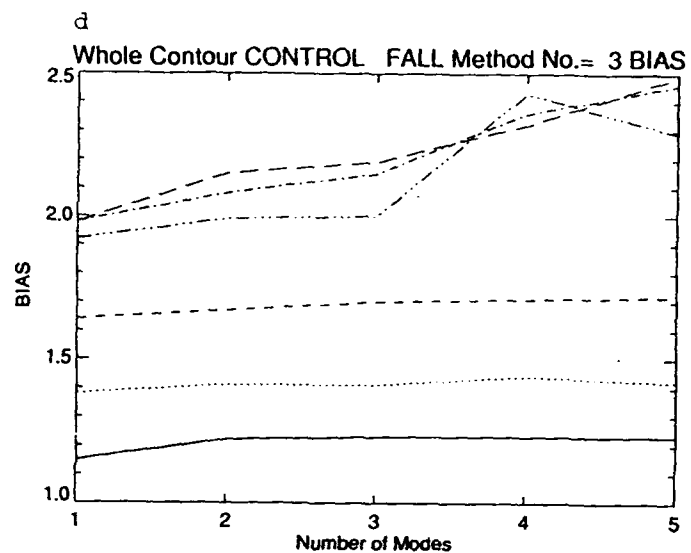
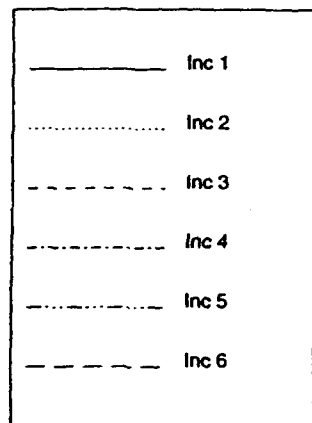


Figure 13: Same as Figure 12, except for method number = 3.



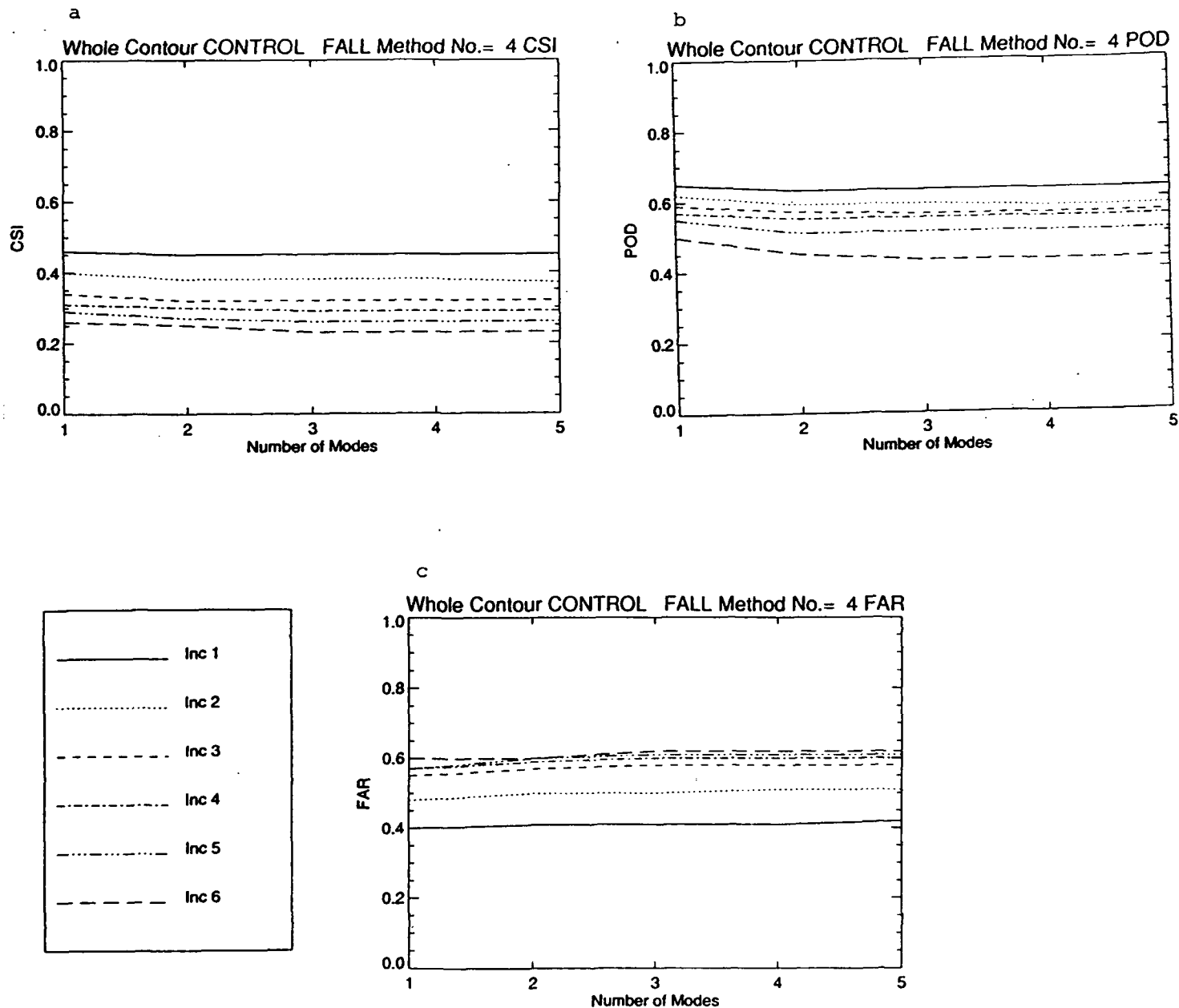


Figure 14: Same as Figure 12, except for method number = 4.

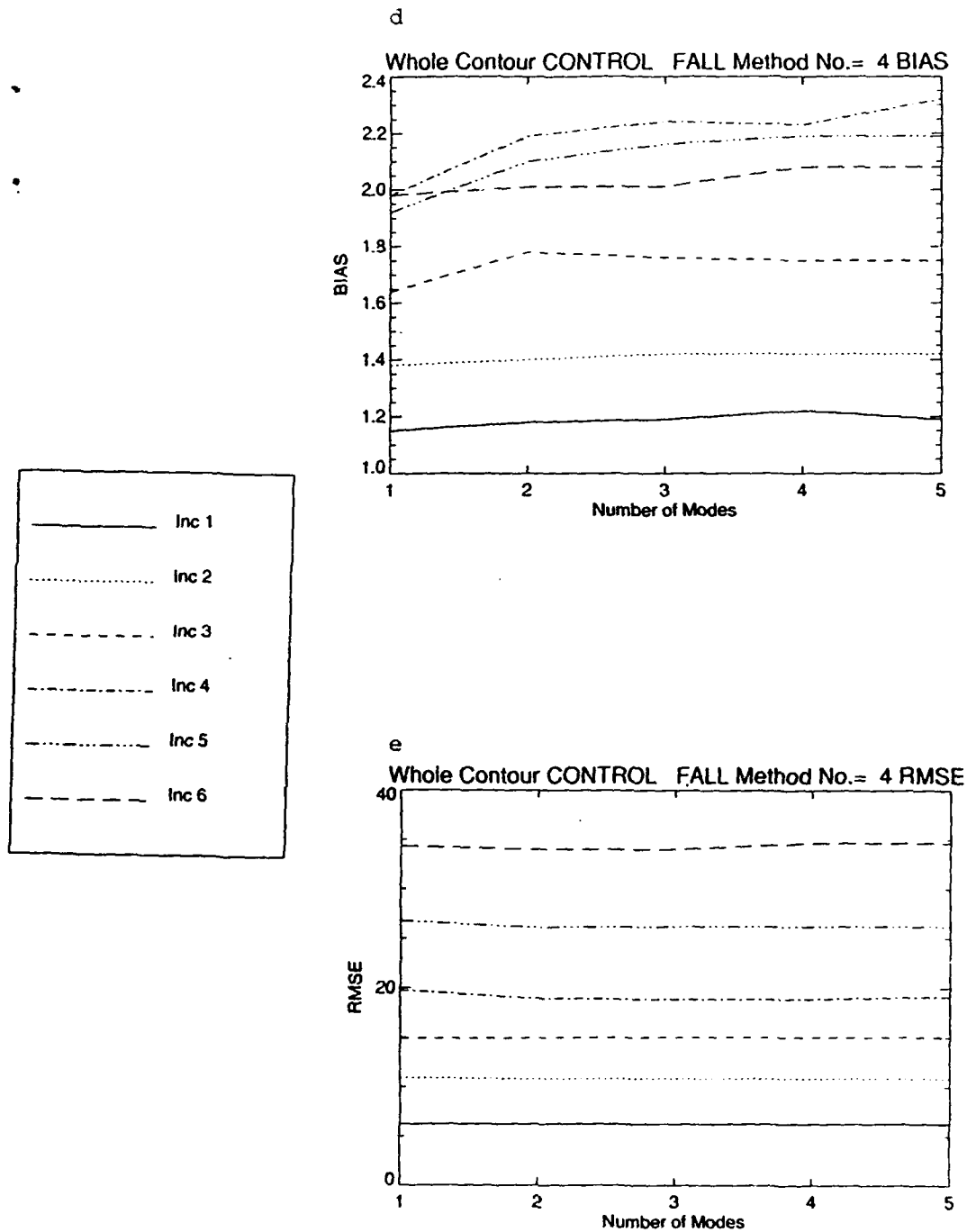


Figure 14: Same as Figure 12, except for method number = 4.

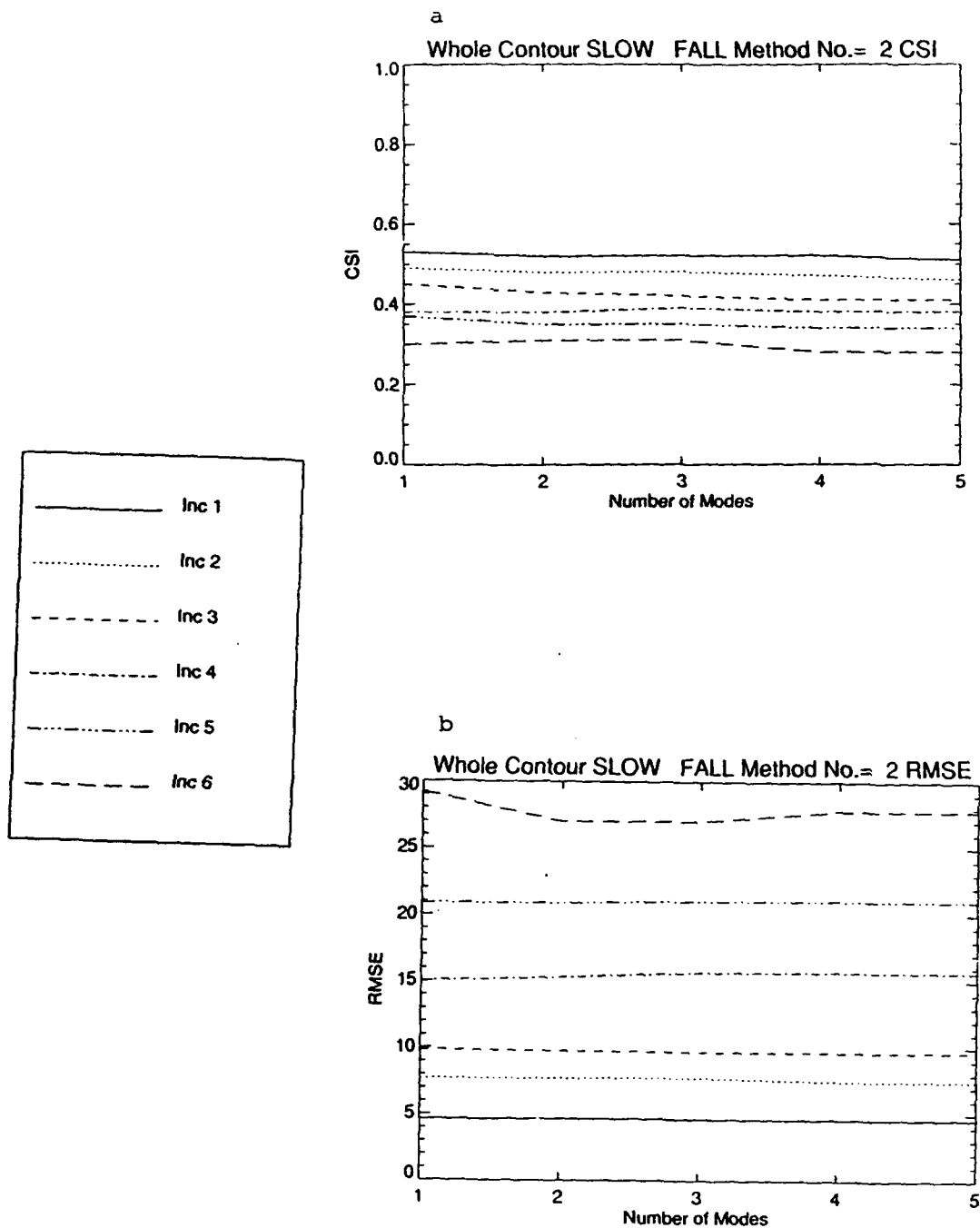


Figure 15: Verification scores for the SLOW feature sample for fall, for the whole contour method with method number = 2. Shown are CSI (a) and RMSE (b) as a function of frequency (number of modes). The different lines correspond to different forecast increments, as in Figure 12.

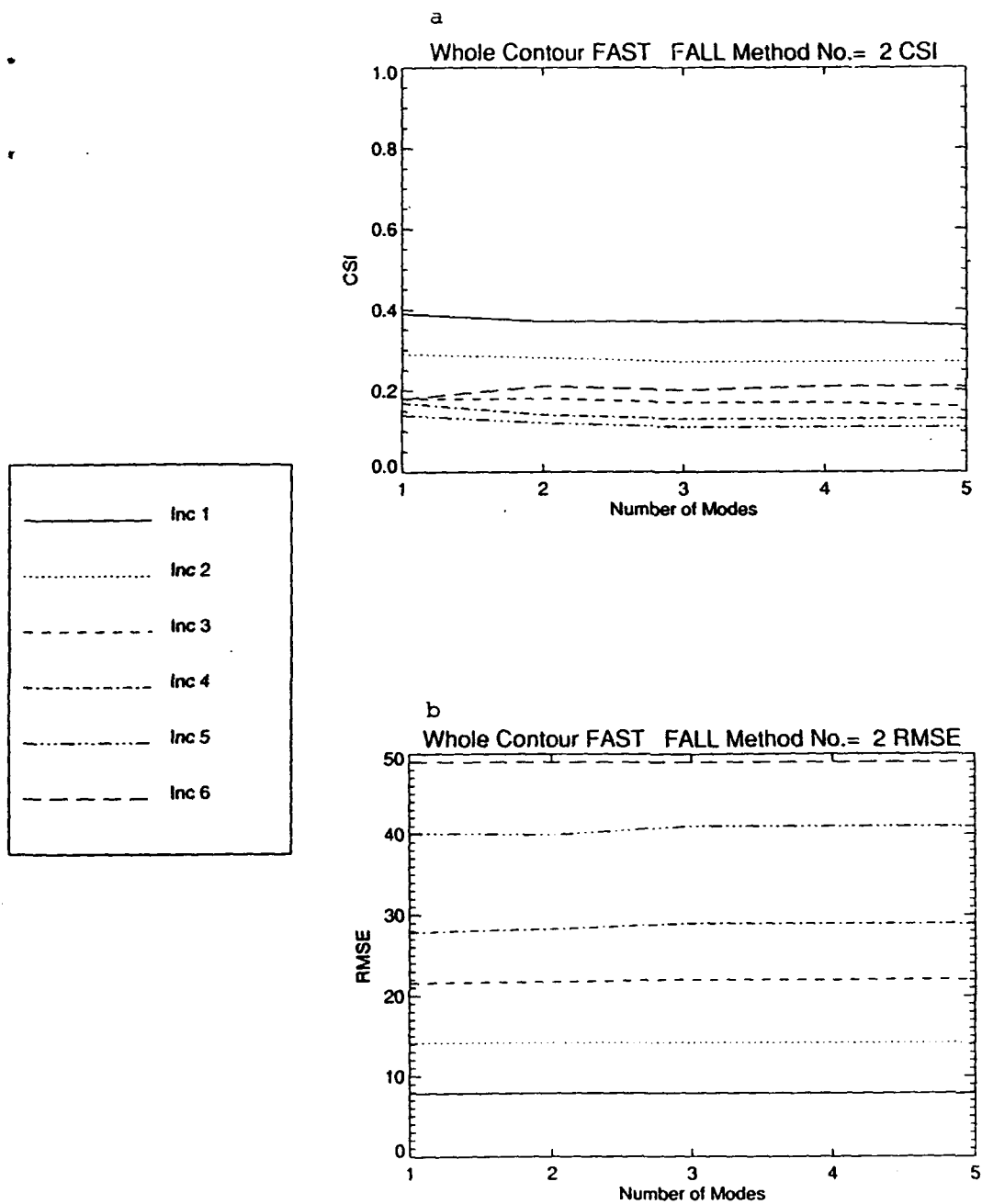


Figure 16: Same as Figure 15, except for the FAST feature subsample.

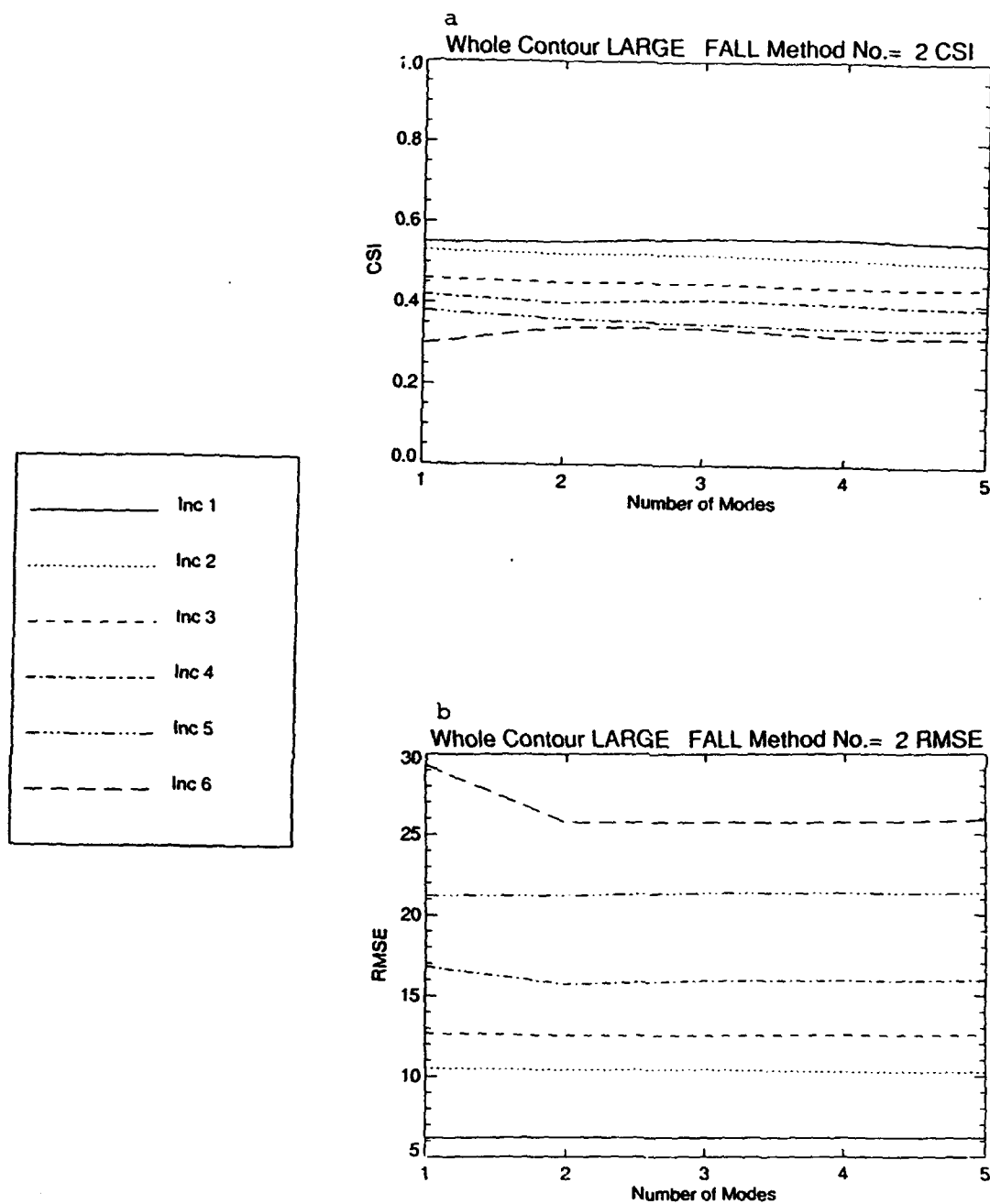


Figure 17: Same as Figure 15, except for the LARGE feature subsample.

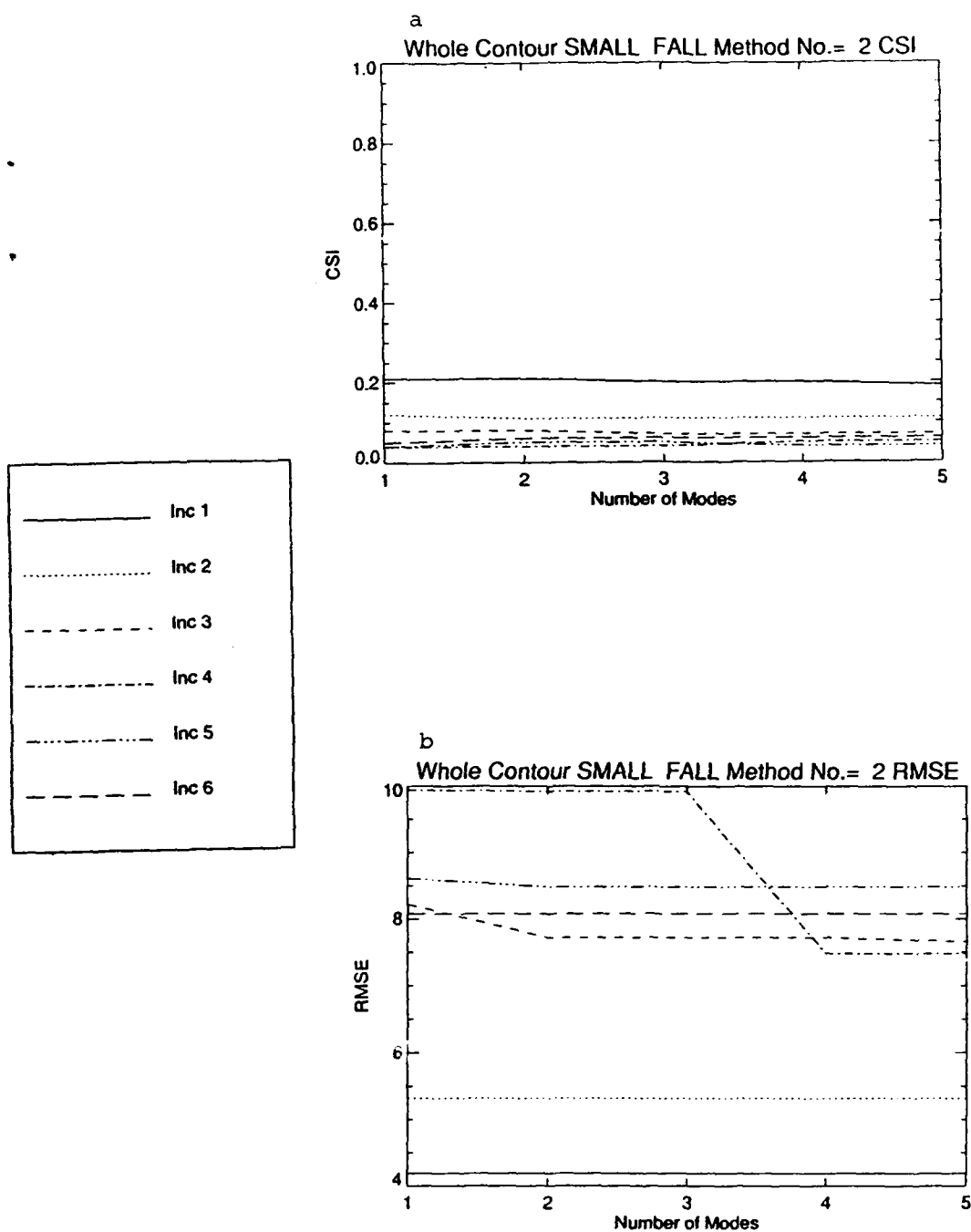


Figure 18: Same as Figure 15, except for the SMALL feature subsample.

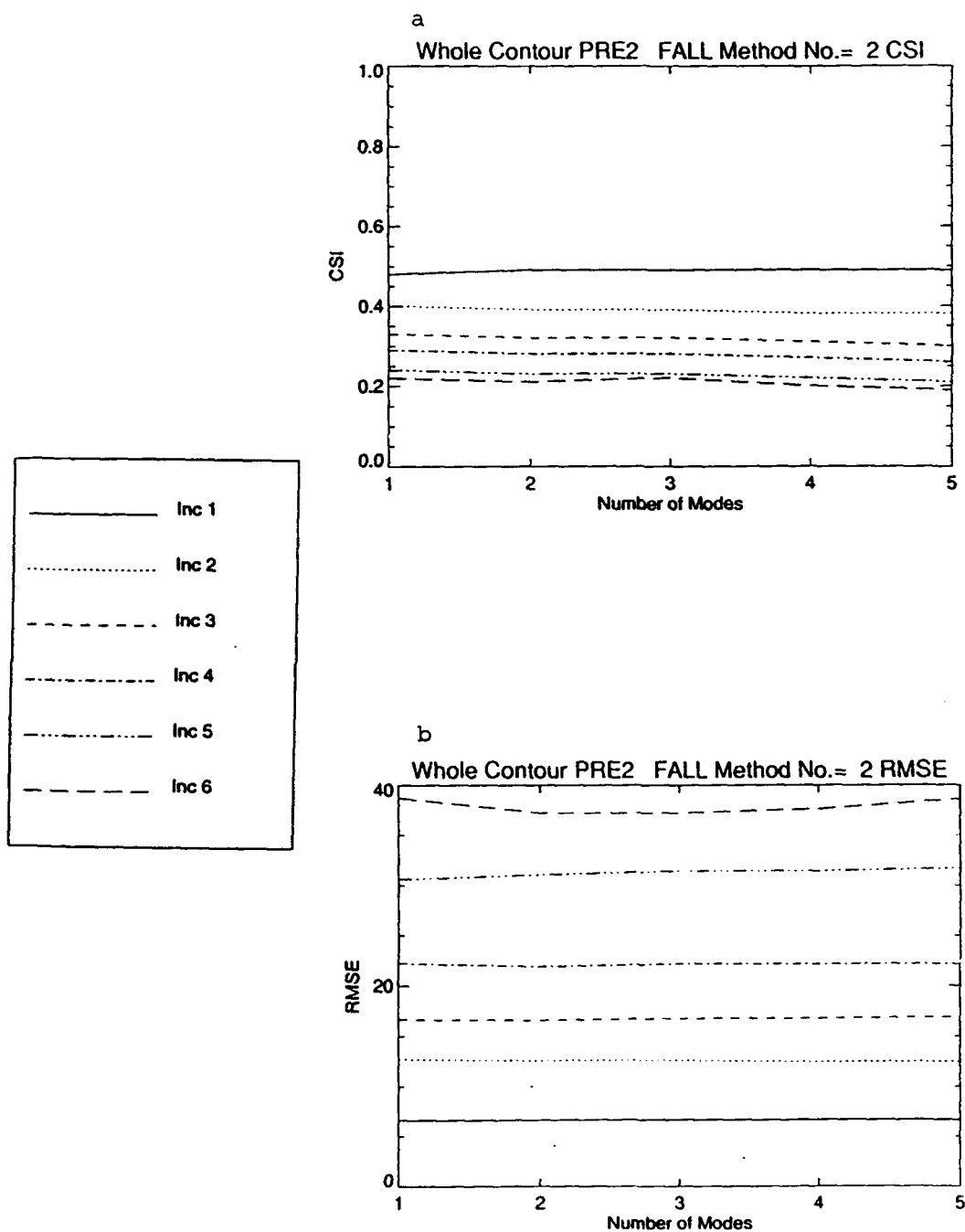


Figure 19: Same as Figure 15, except for the PRE2 subsample.

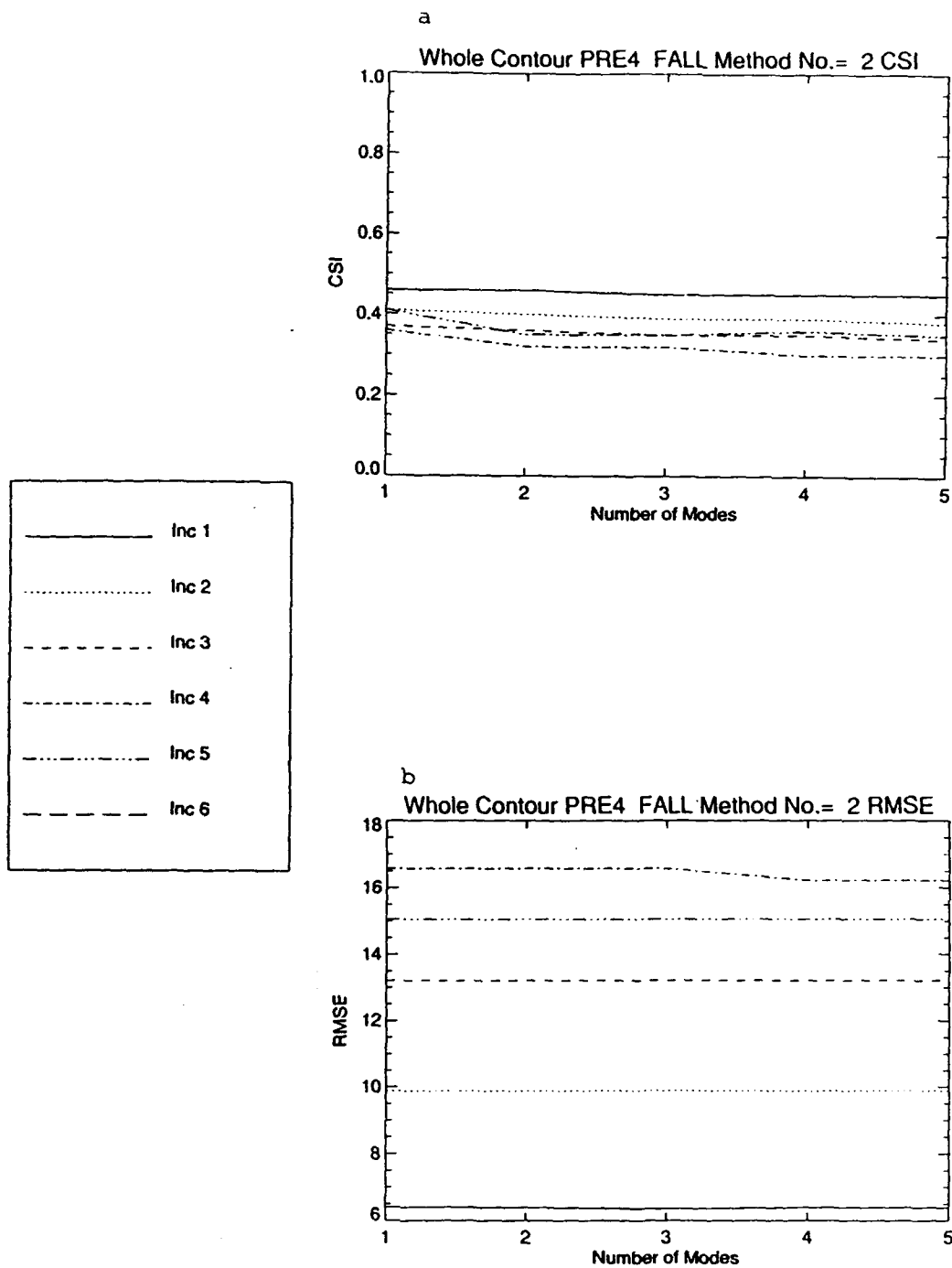


Figure 20: Same as Figure 15, except for the PRE4 subsample.



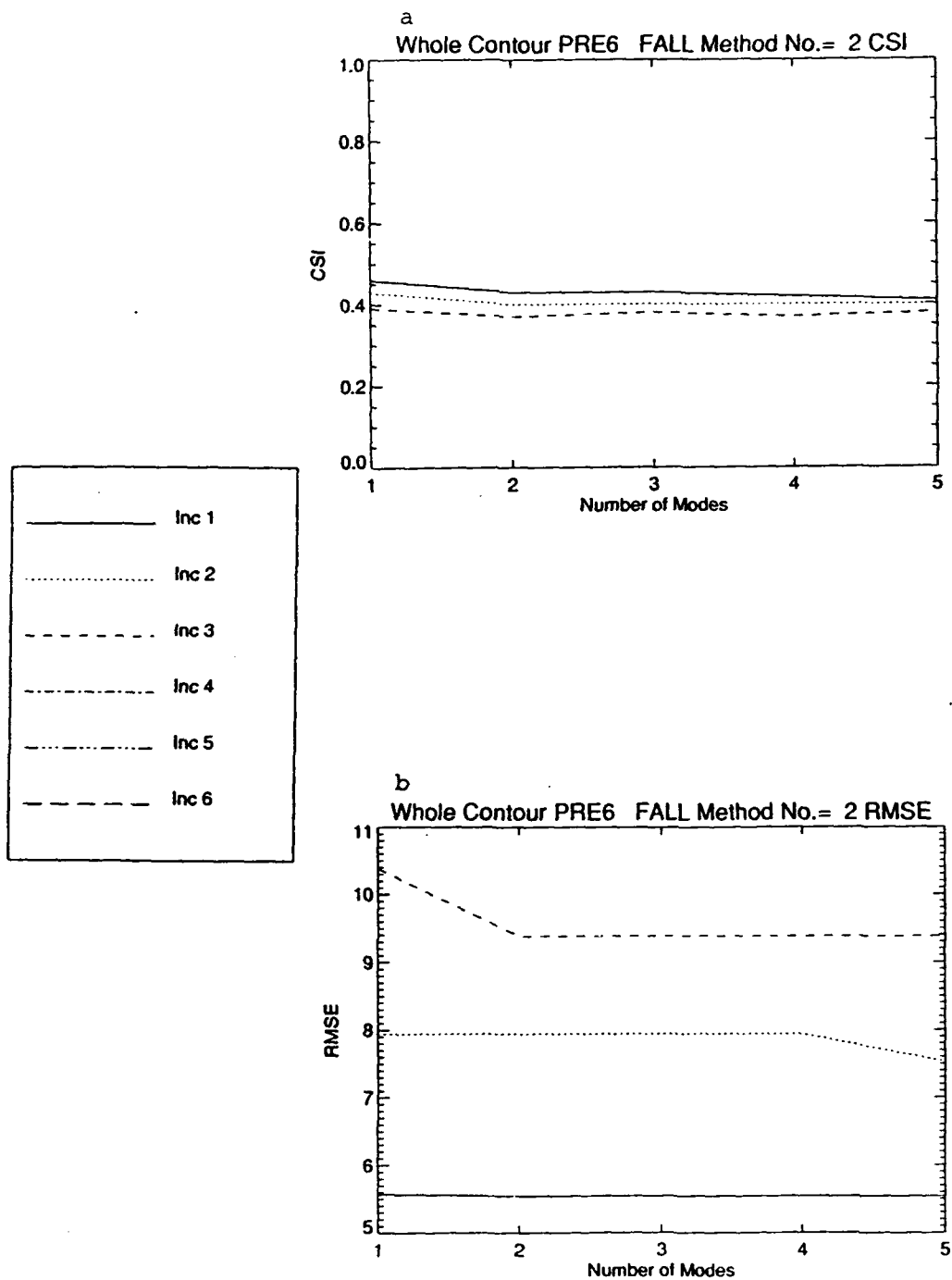
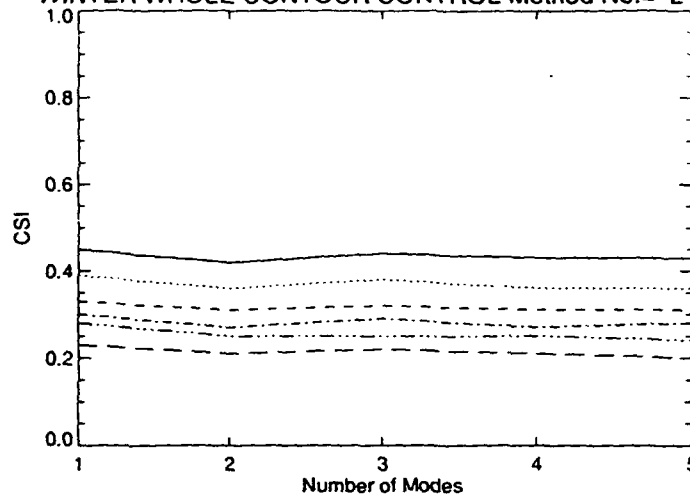


Figure 21: Same as Figure 15, except for the PRE6 subsample.

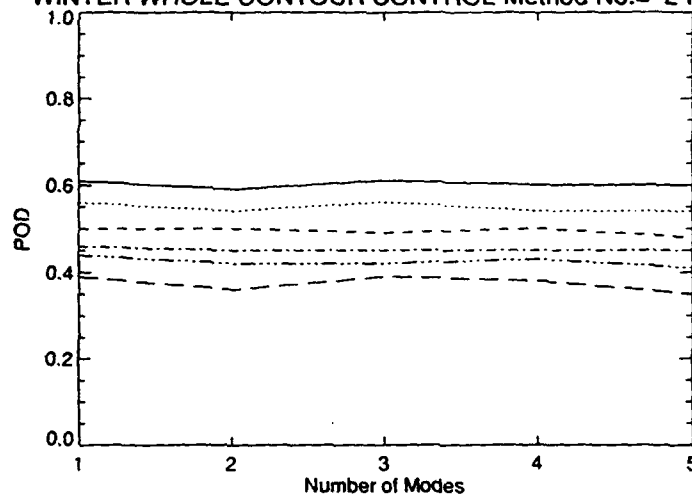
a

WINTER WHOLE CONTOUR CONTROL Method No.= 2 CSI



b

WINTER WHOLE CONTOUR CONTROL Method No.= 2 POD



c

WINTER WHOLE CONTOUR CONTROL Method No.= 2 FAR

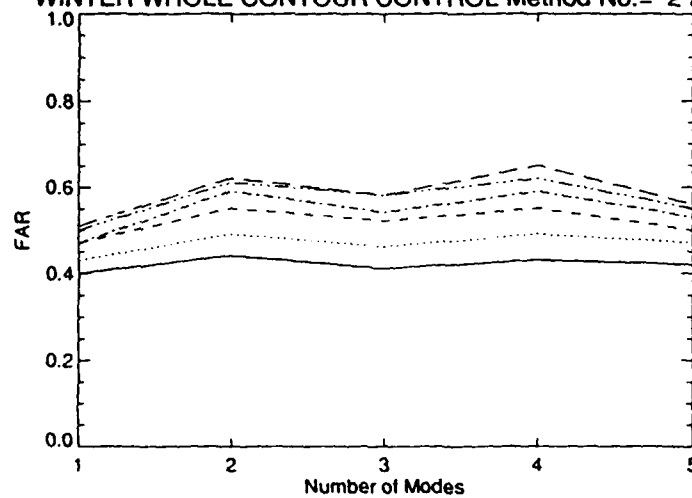


Figure 22: Same as Figure 12, except for winter.

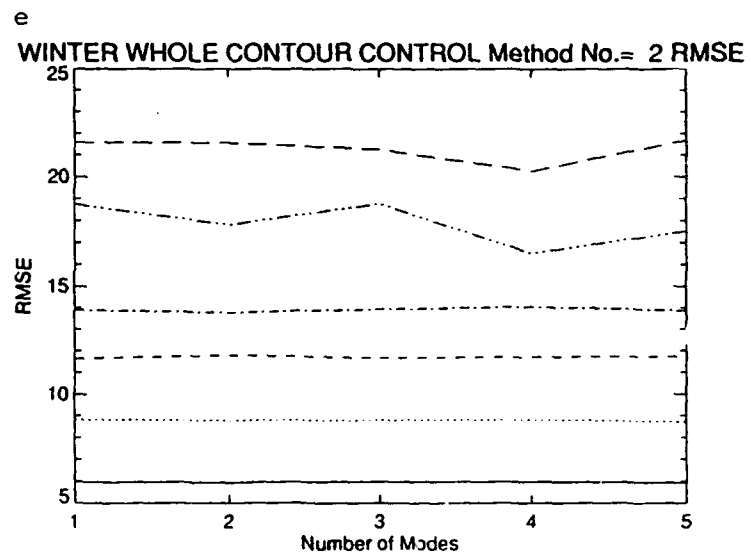
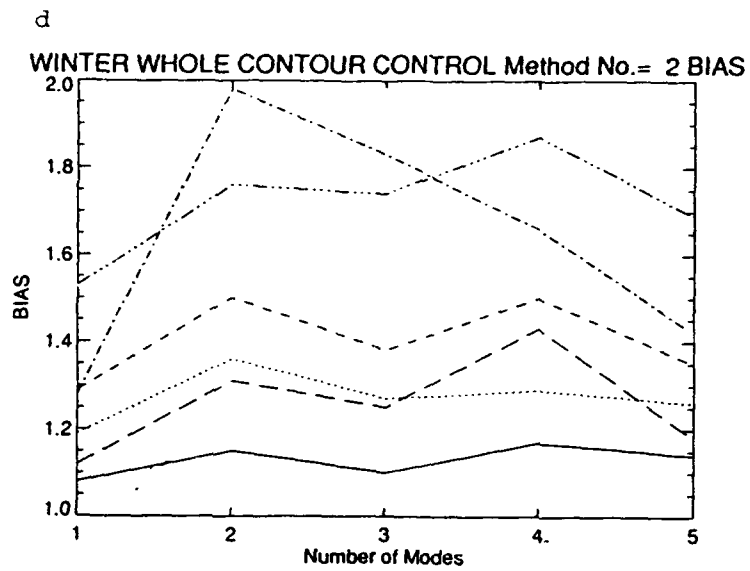


Figure 22: Same as Figure 12, except for winter.

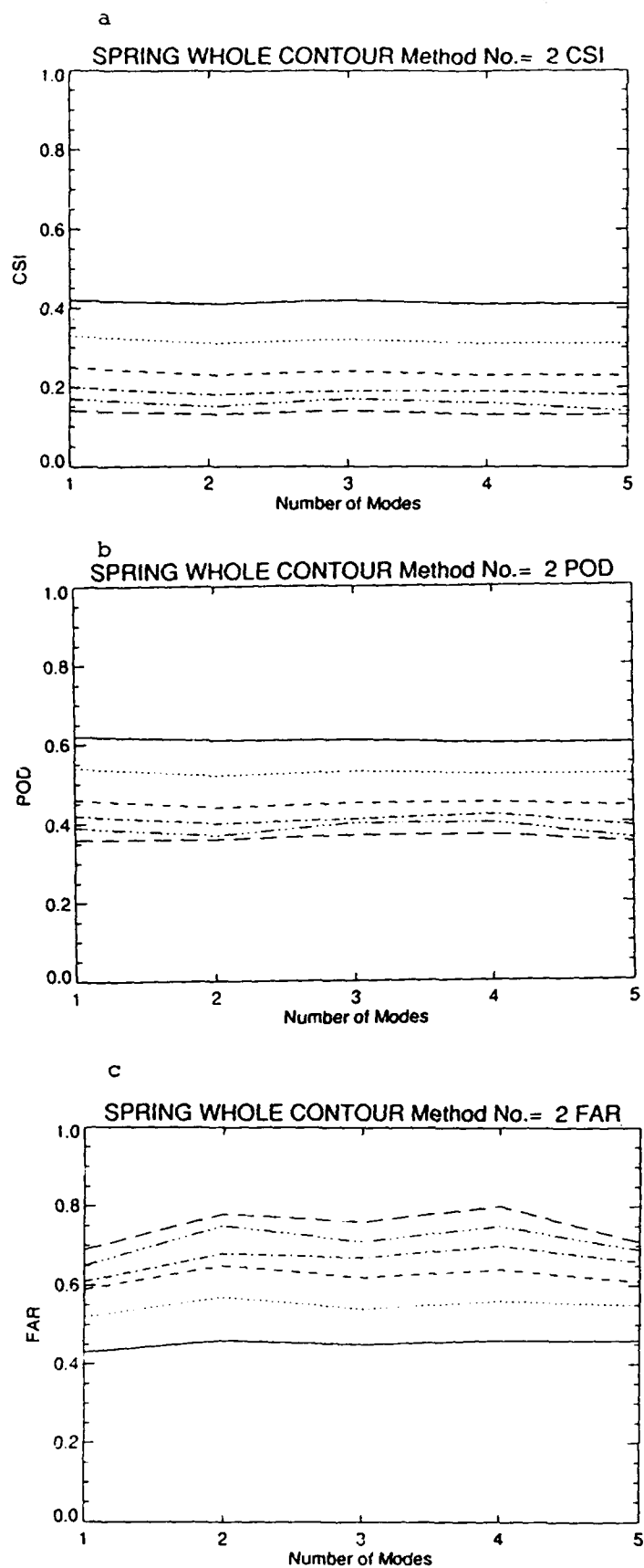
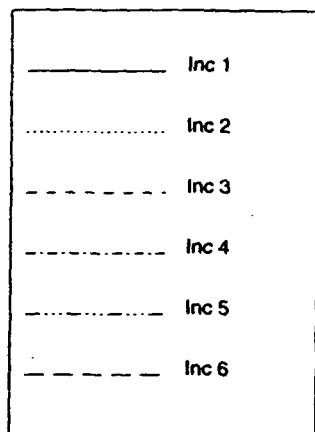


Figure 23: Same as Figure 12, except for spring.

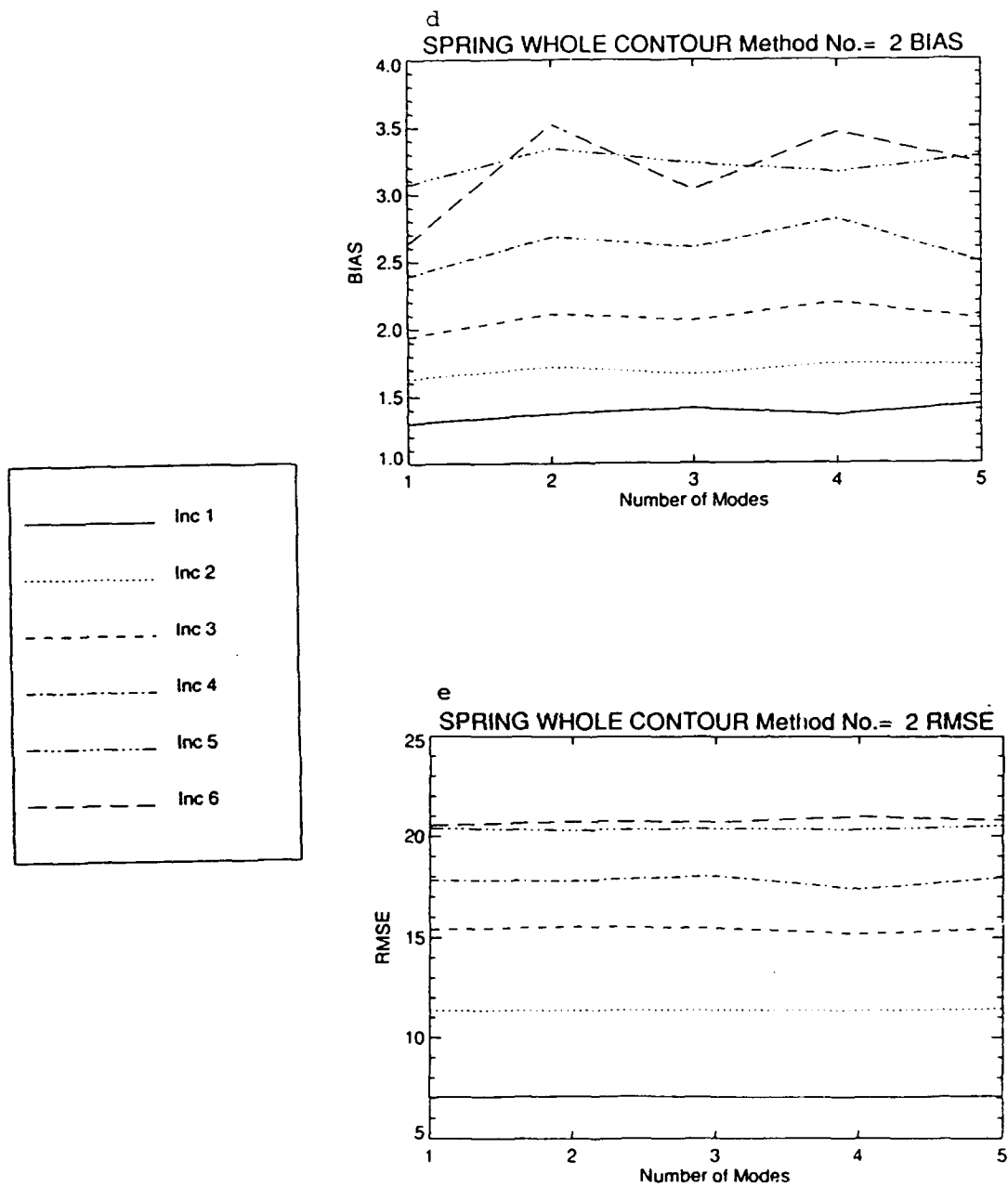


Figure 23: Same as Figure 12, except for spring.

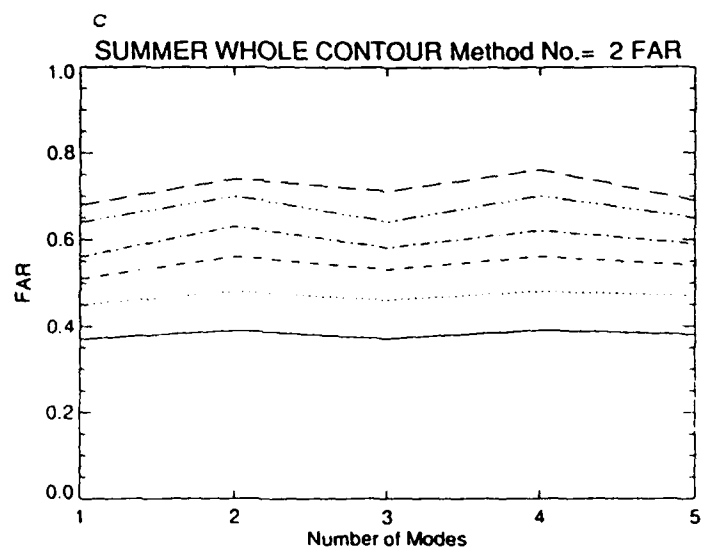
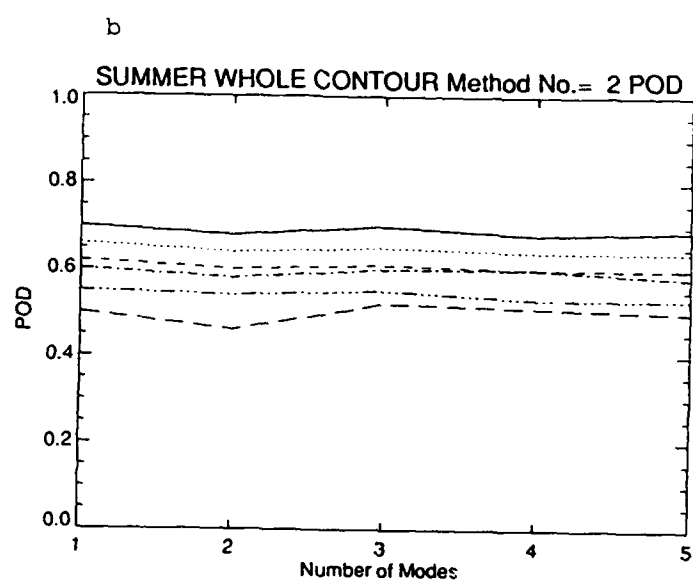
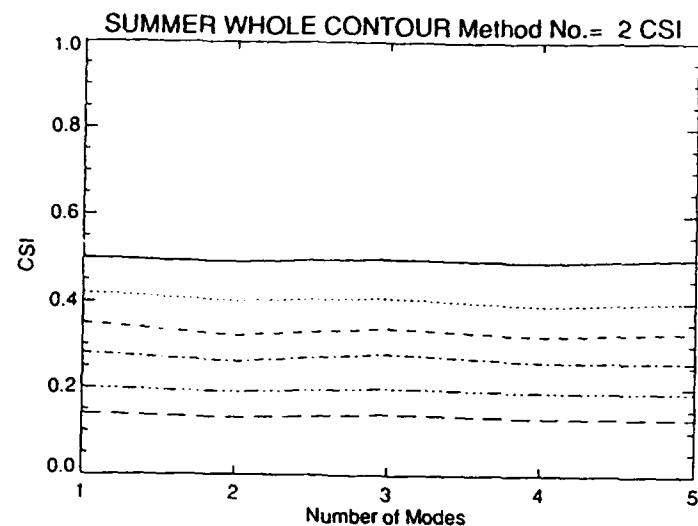
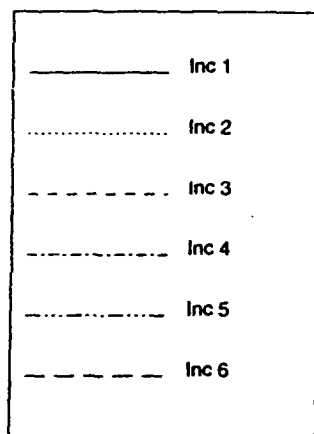


Figure 24: Same as Figure 12, except for summer.

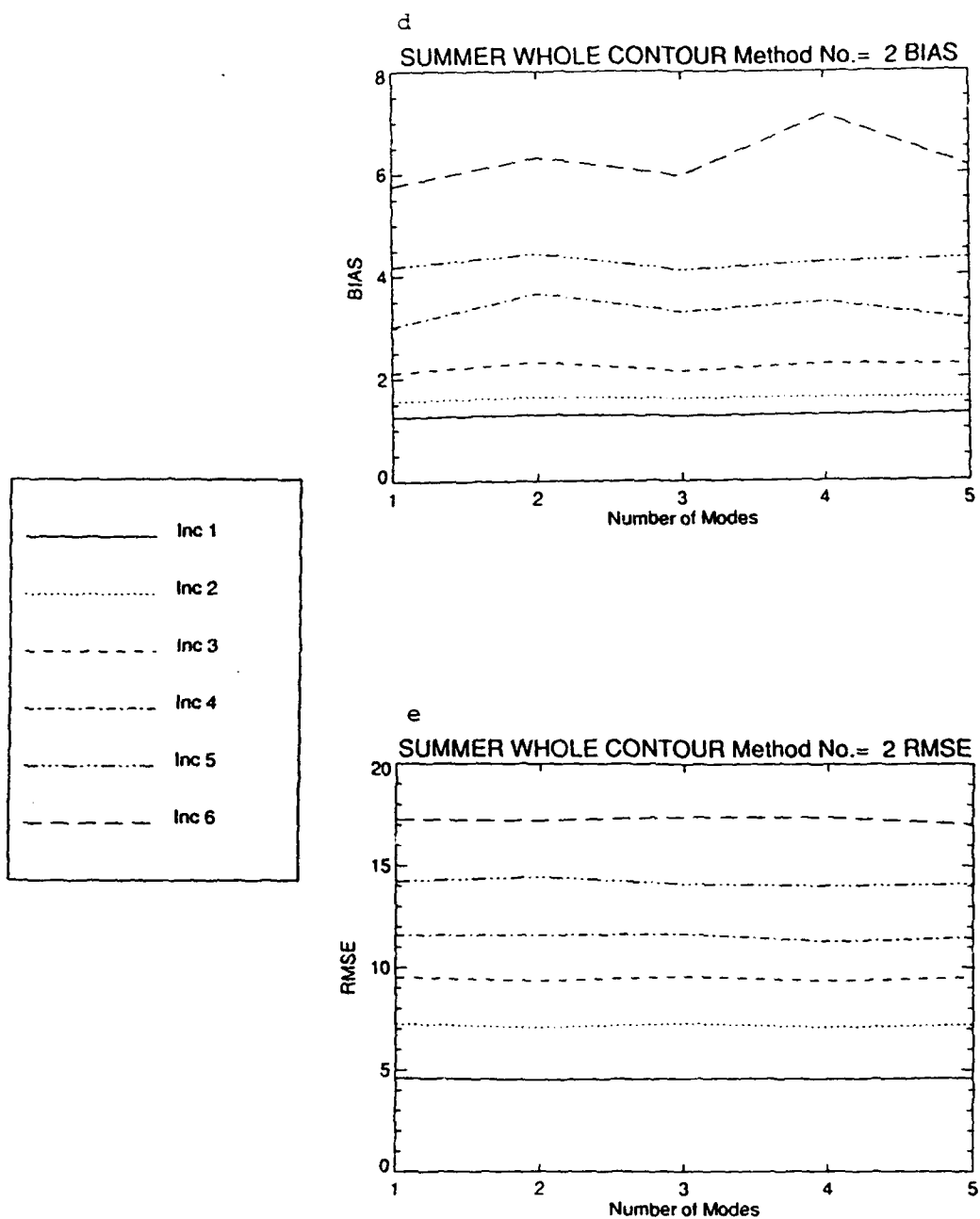


Figure 24: Same as Figure 12, except for summer.

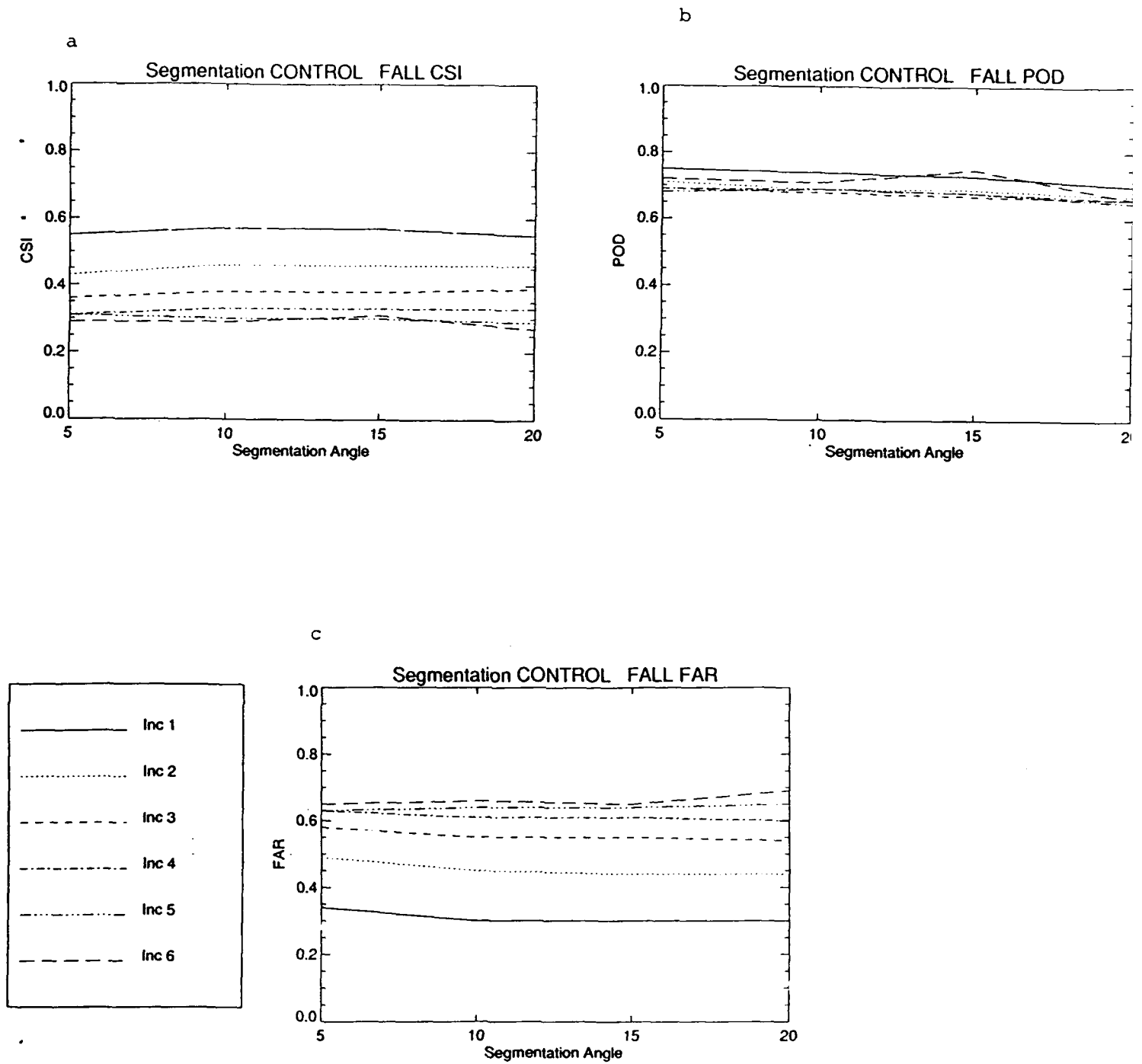


Figure 25: Verification scores for the CONTROL sample for fall, for the segmentation method. Shown are CSI (a), POD (b), FAR (c), BIAS (d), and RMSE (e) as a function of the segmentation angle (in  $^{\circ}$ ). The different lines correspond to different forecast increments, as in Figure 12.



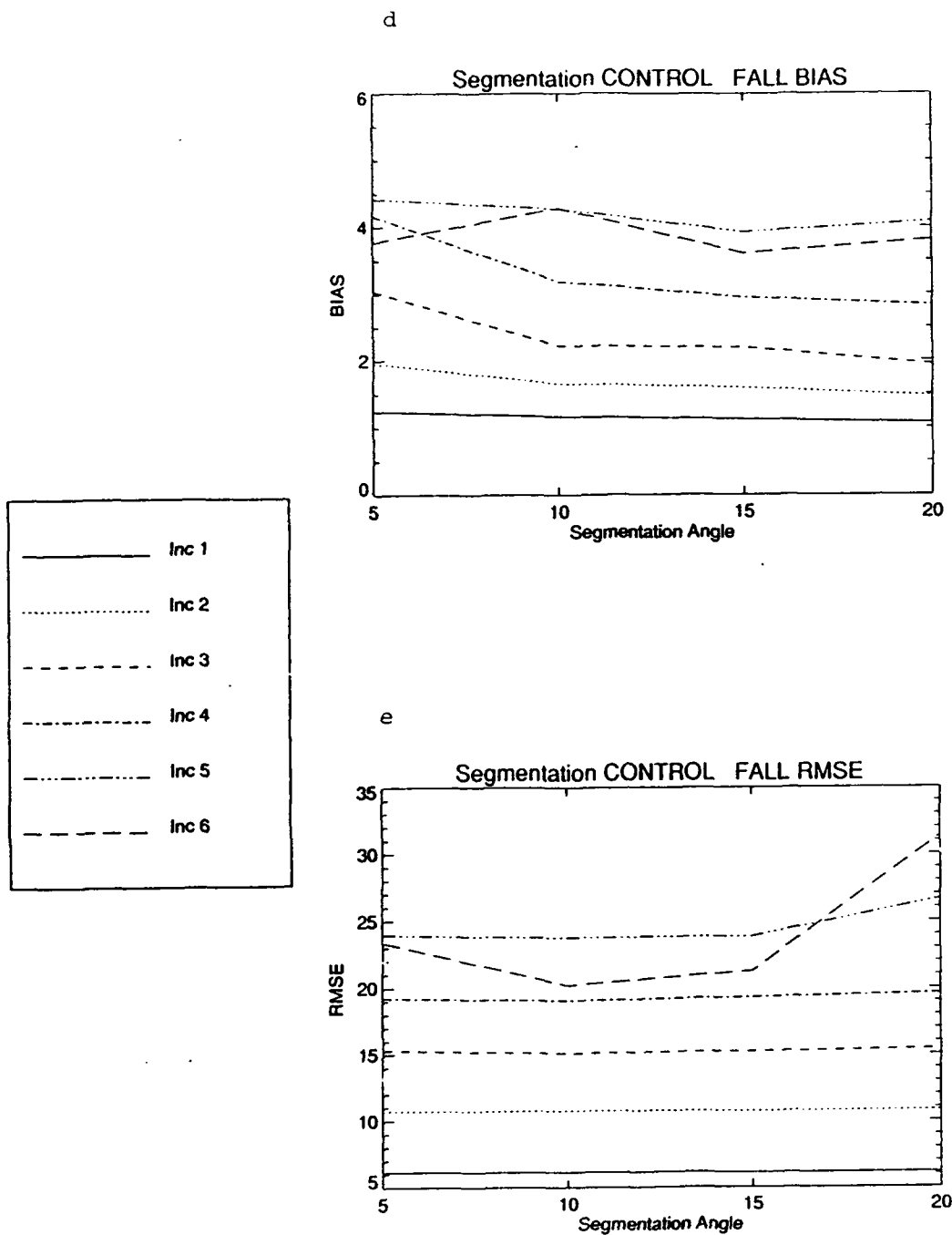


Figure 25: Verification scores for the CONTROL sample for fall, for the segmentation method. Shown are CSI (a), POD (b), FAR (c), BIAS (d), and RMSE (e) as a function of the segmentation angle (in  $^{\circ}$ ). The different lines correspond to different forecast increments, as in Figure 12.

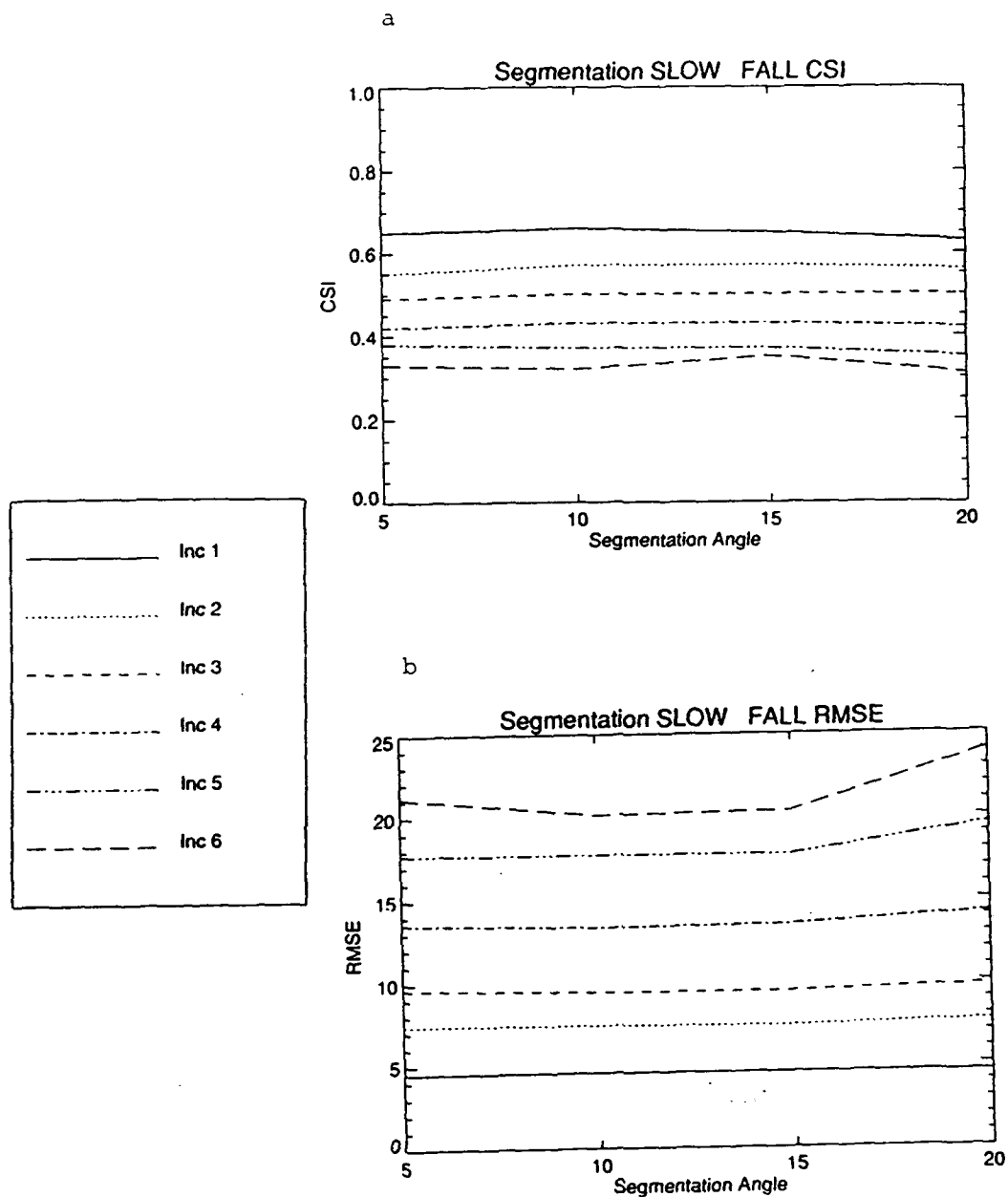


Figure 26: Verification scores for the SLOW feature sample for fall, for the segmentation method. Shown are CSI (a) and RMSE (b) as a function of the segmentation angle (in °). The different lines correspond to different forecast increments, as in Figure 12.

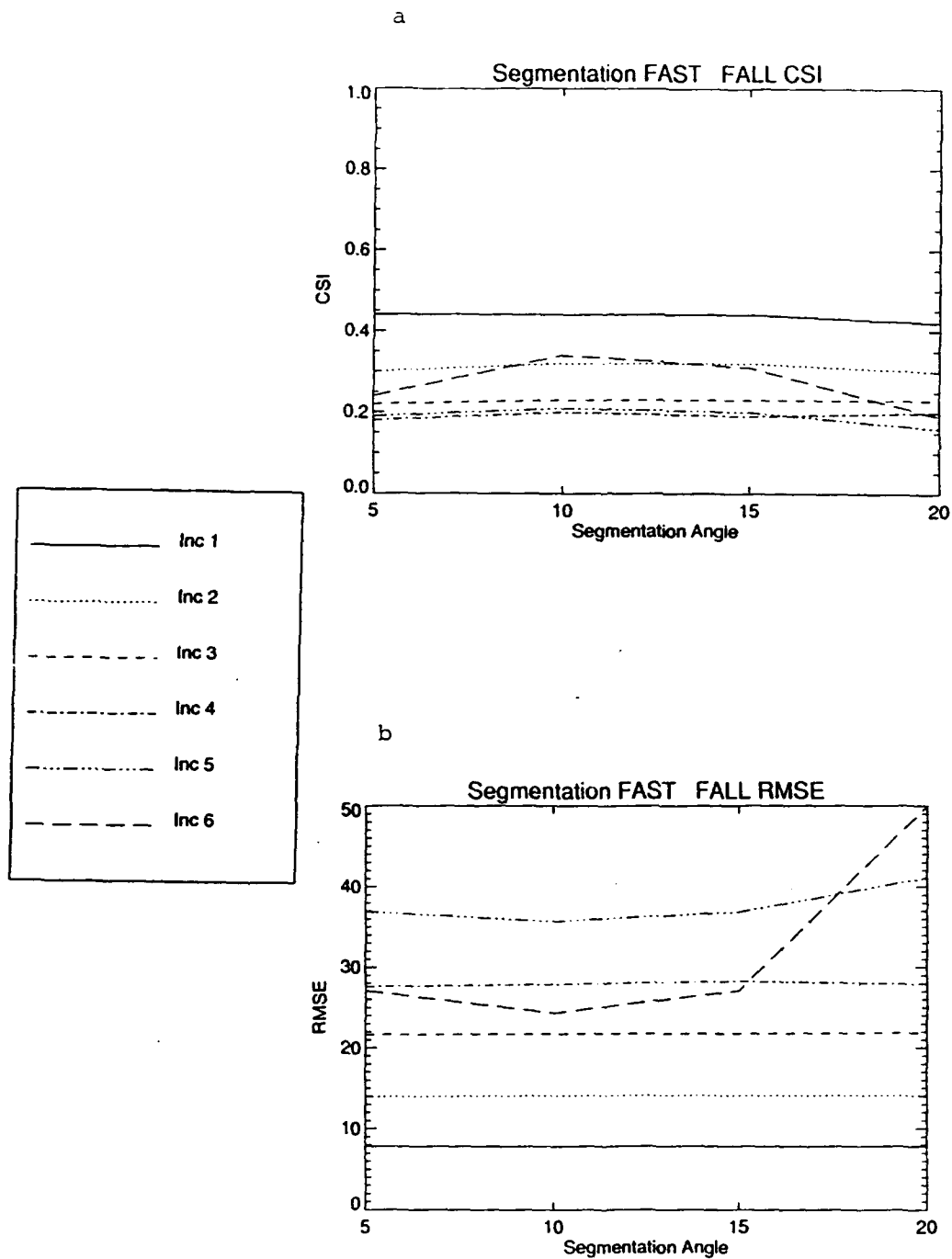


Figure 27: Same as Figure 26, except for the FAST feature subsample.

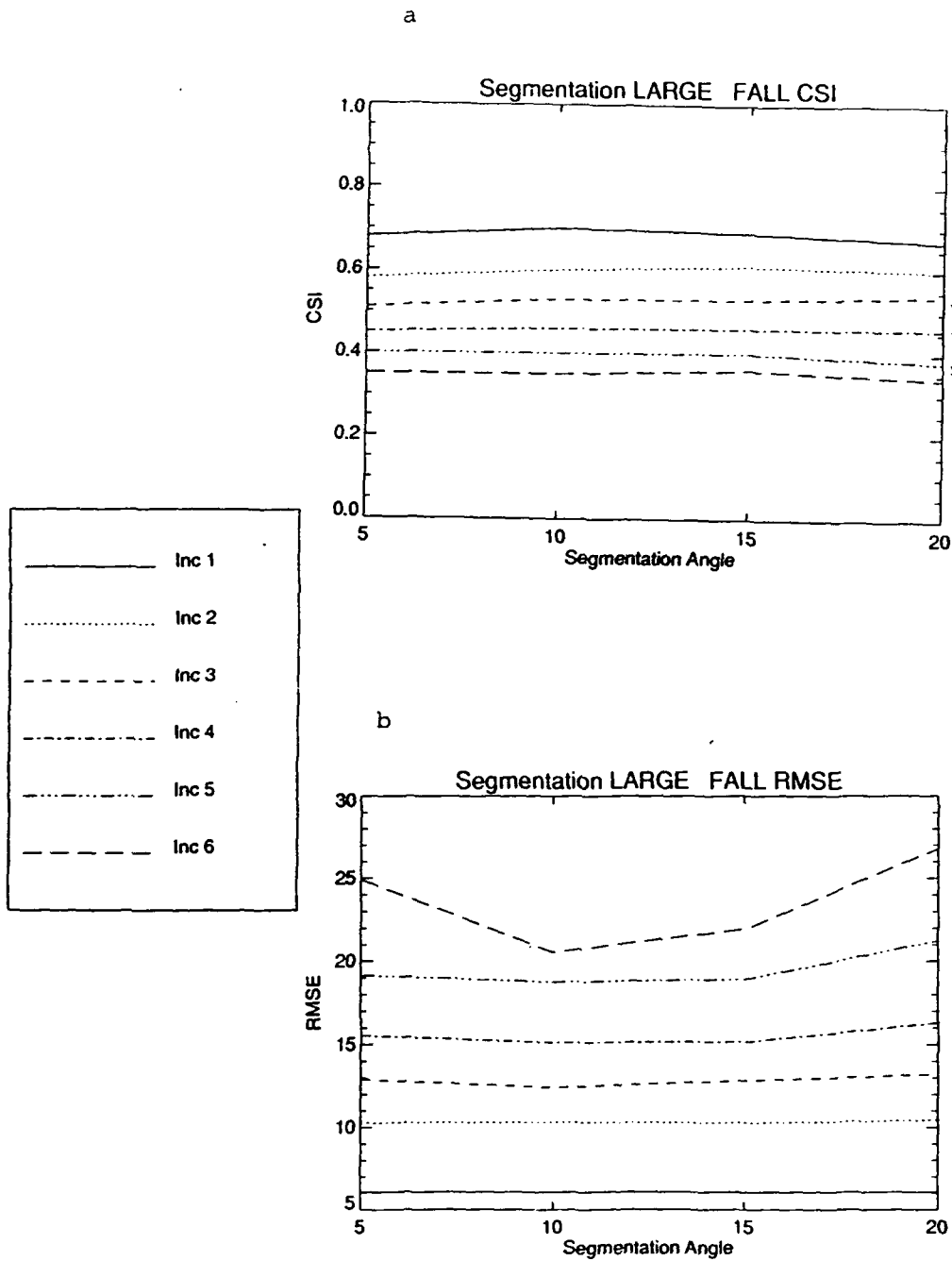


Figure 28: Same as Figure 26, except for the LARGE feature subsample.

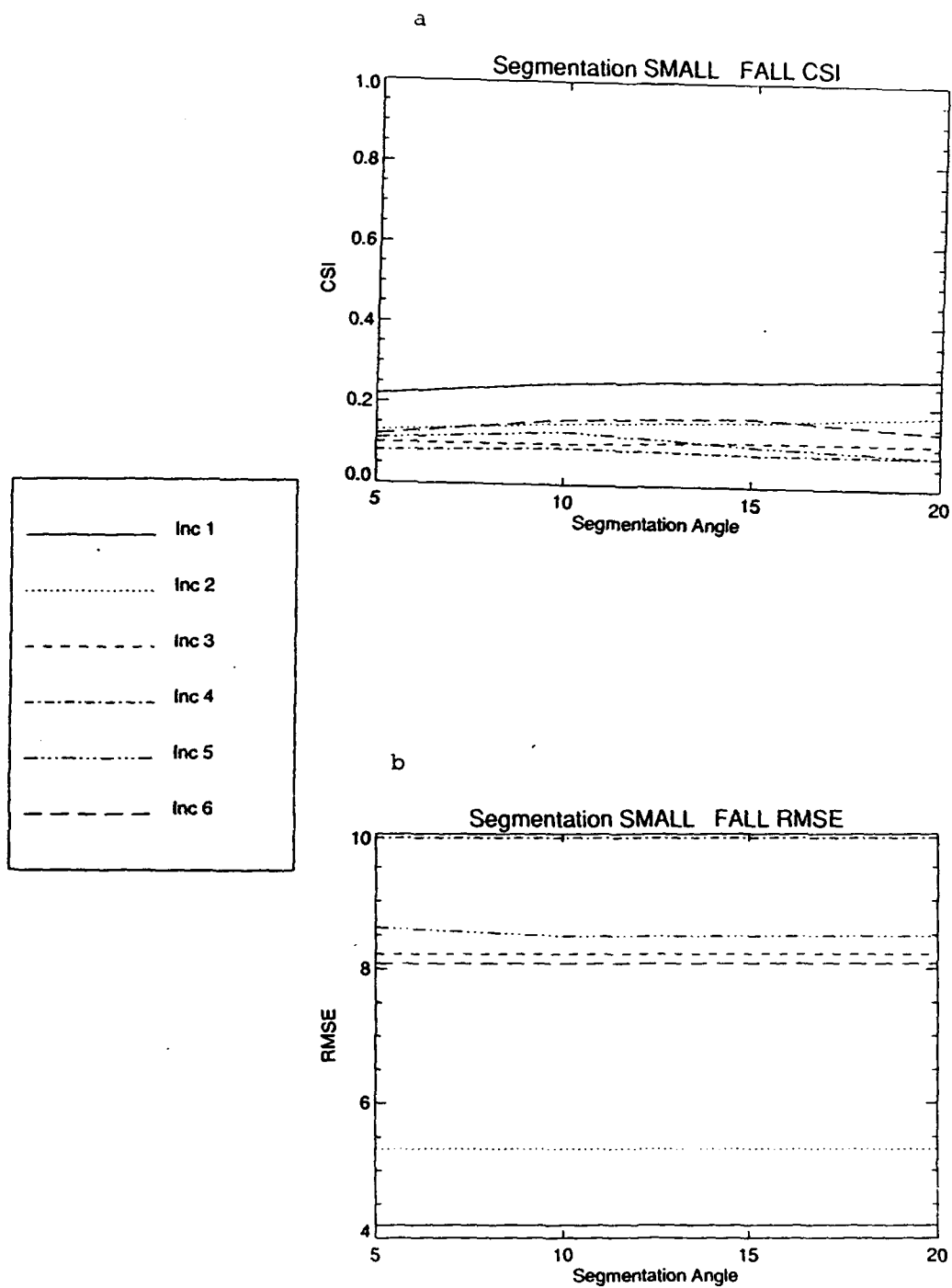


Figure 29: Same as Figure 26, except for the SMALL feature subsample.

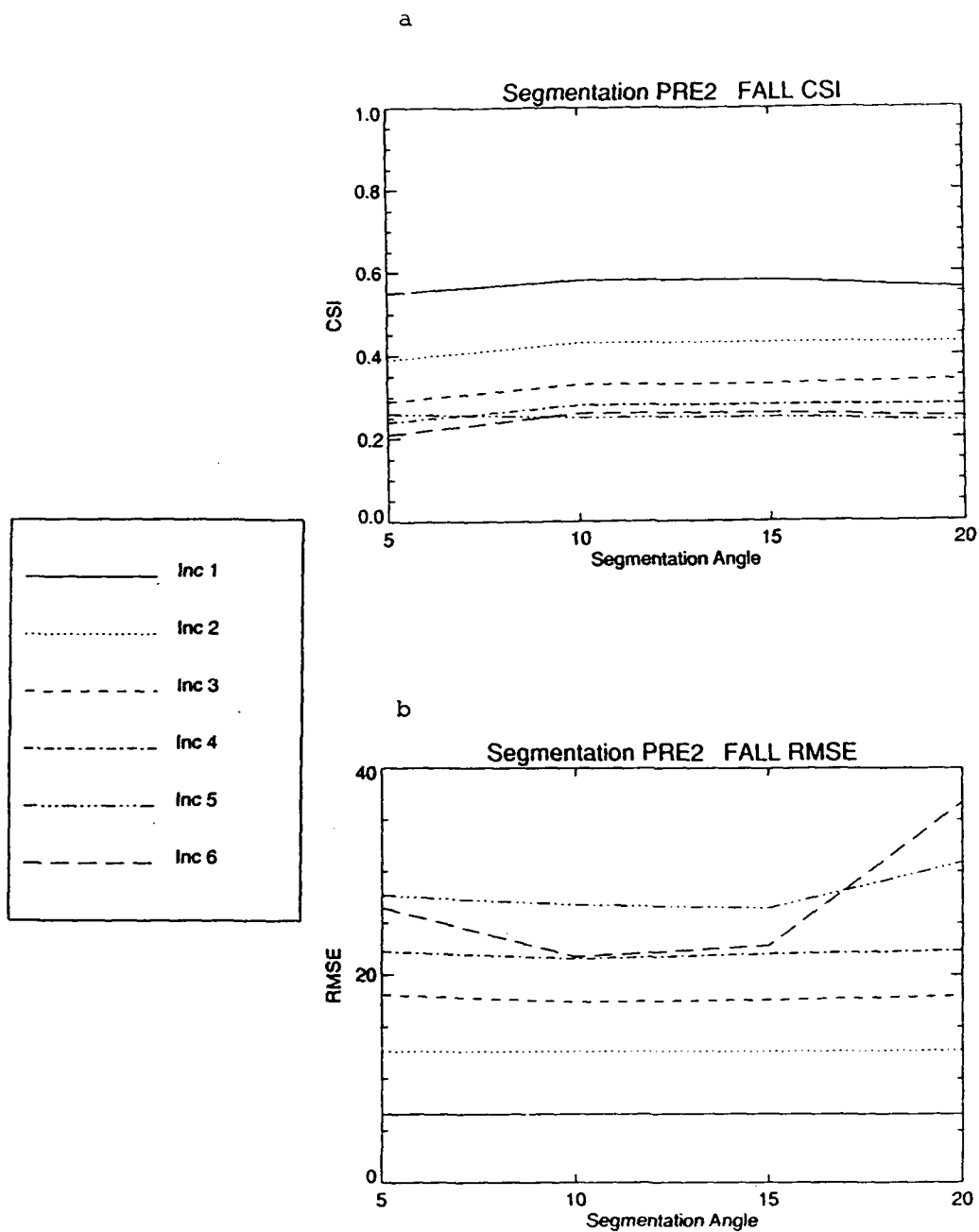


Figure 30: Same as Figure 26, except for the PRE2 subsample.

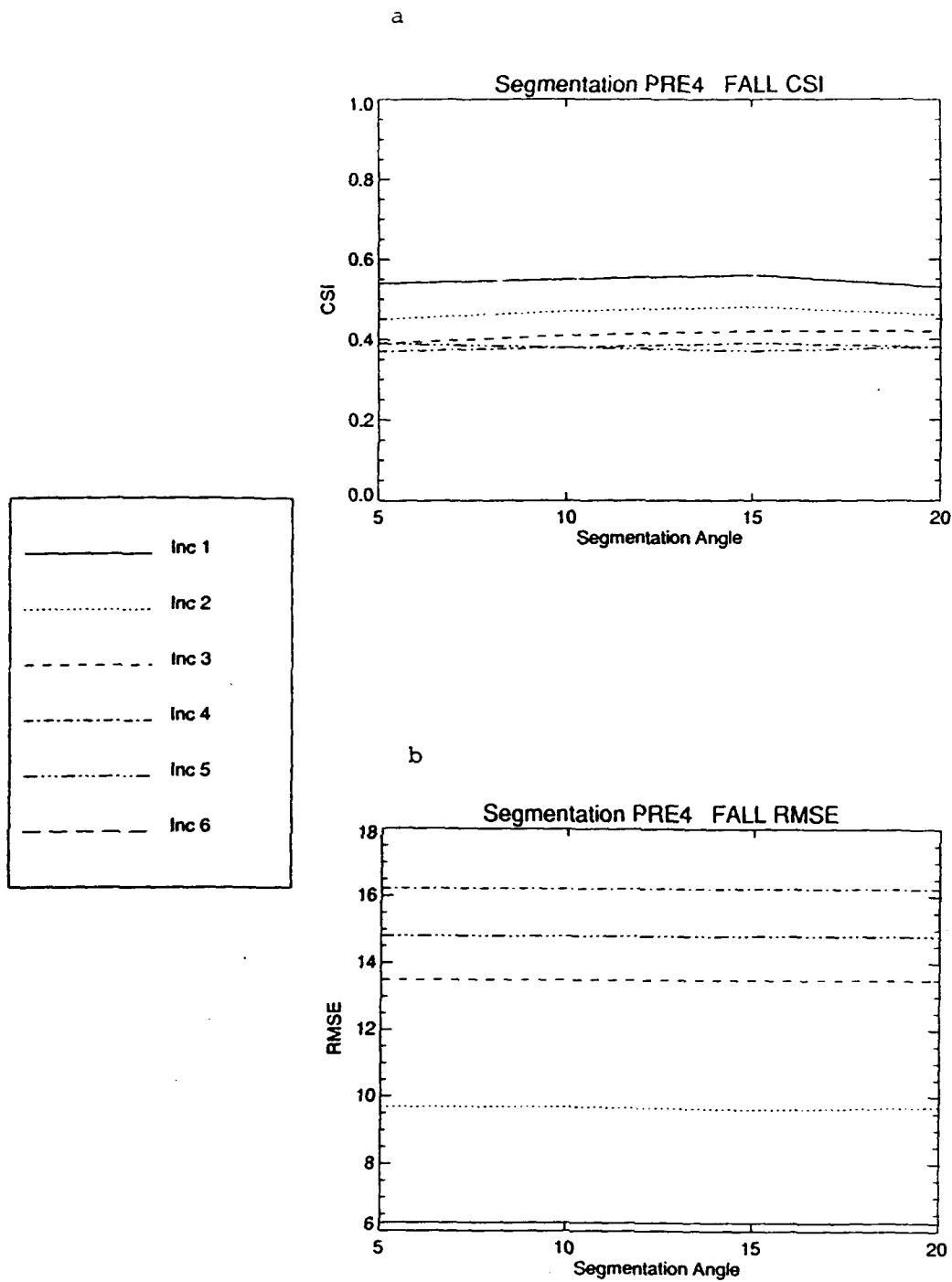


Figure 31: Same as Figure 26, except for the PRE4 subsample.

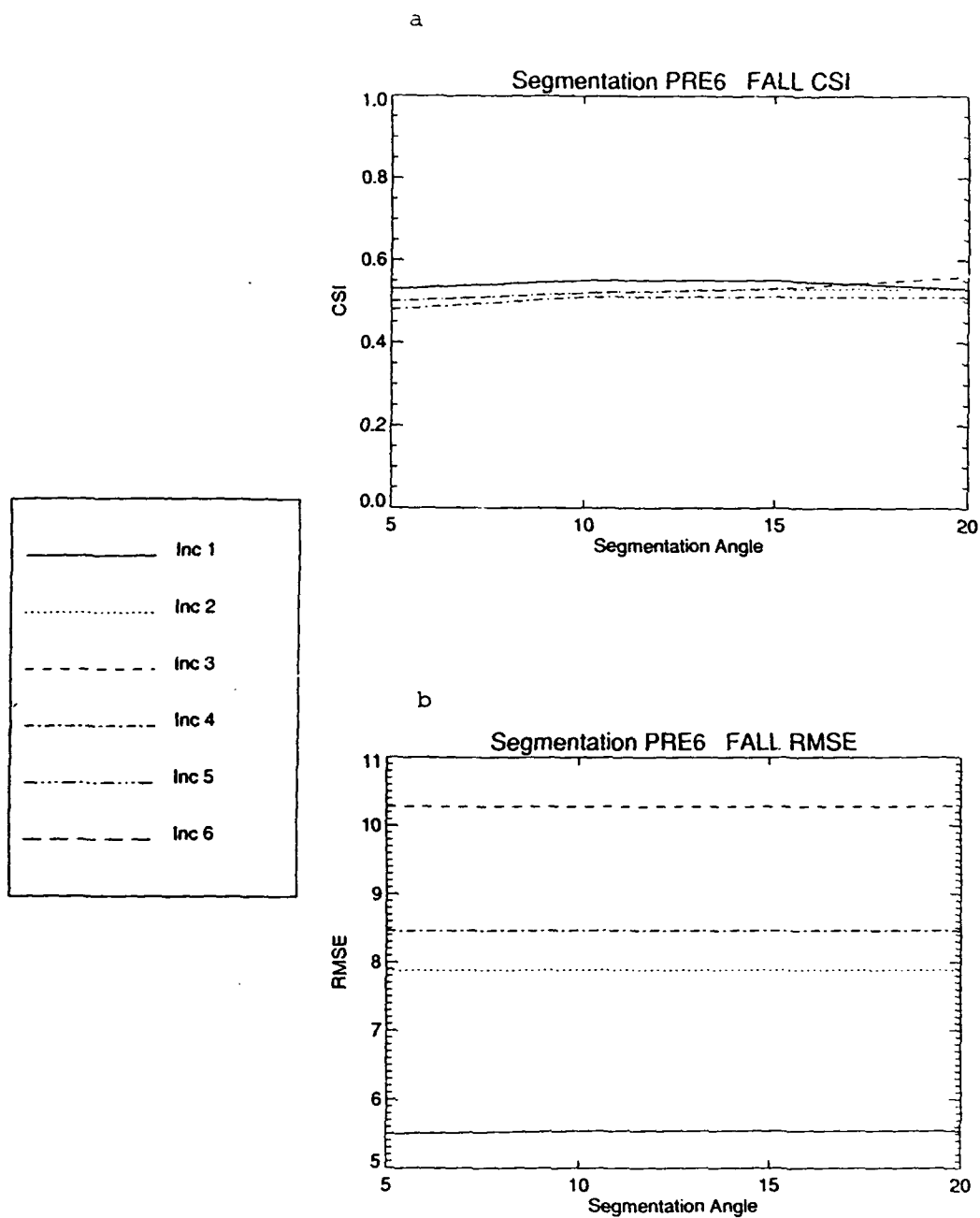


Figure 32: Same as Figure 26, except for the PRE6 subsample.



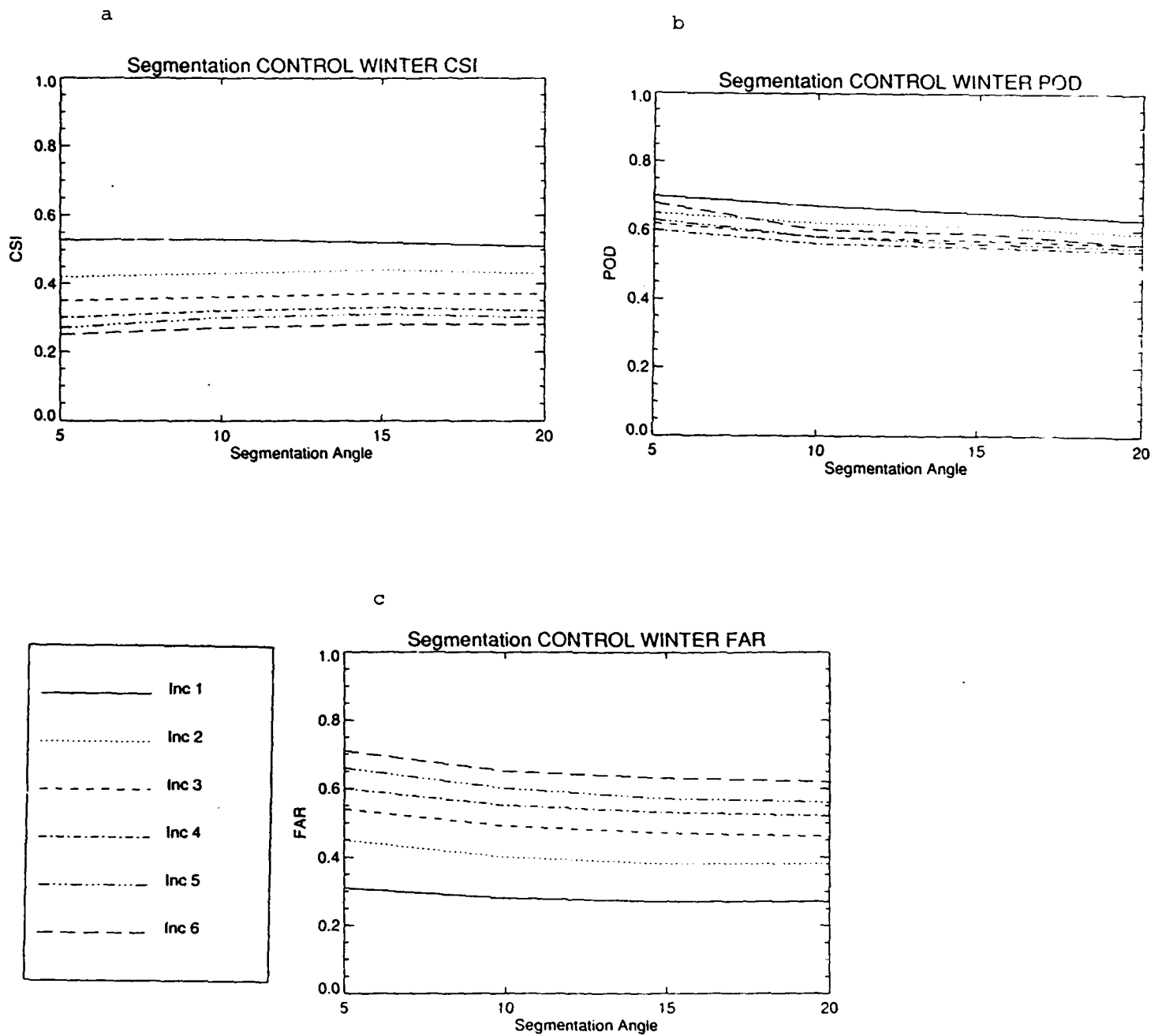


Figure 33: Same as Figure 25, except for winter.

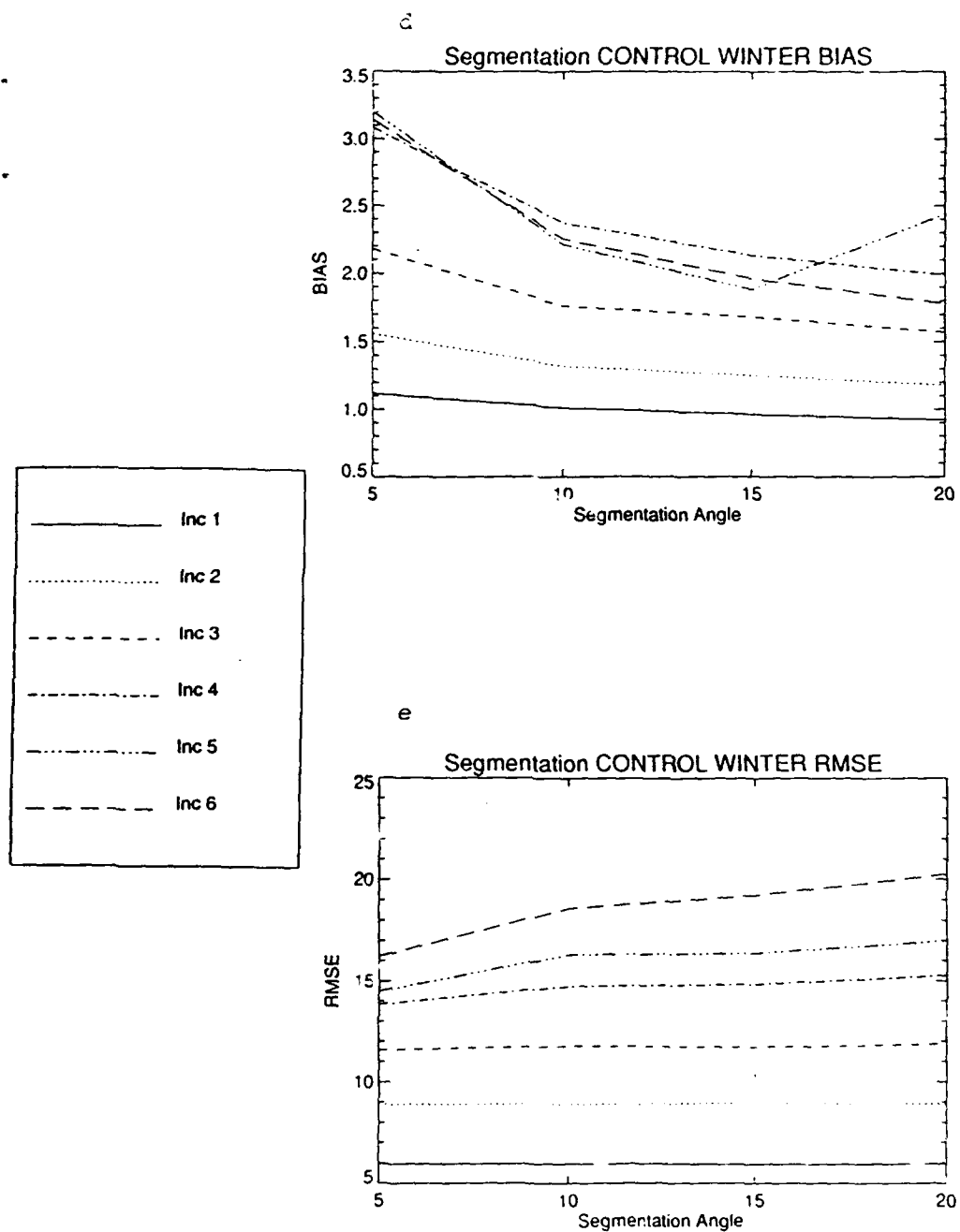


Figure 33: Same as Figure 25, except for winter.

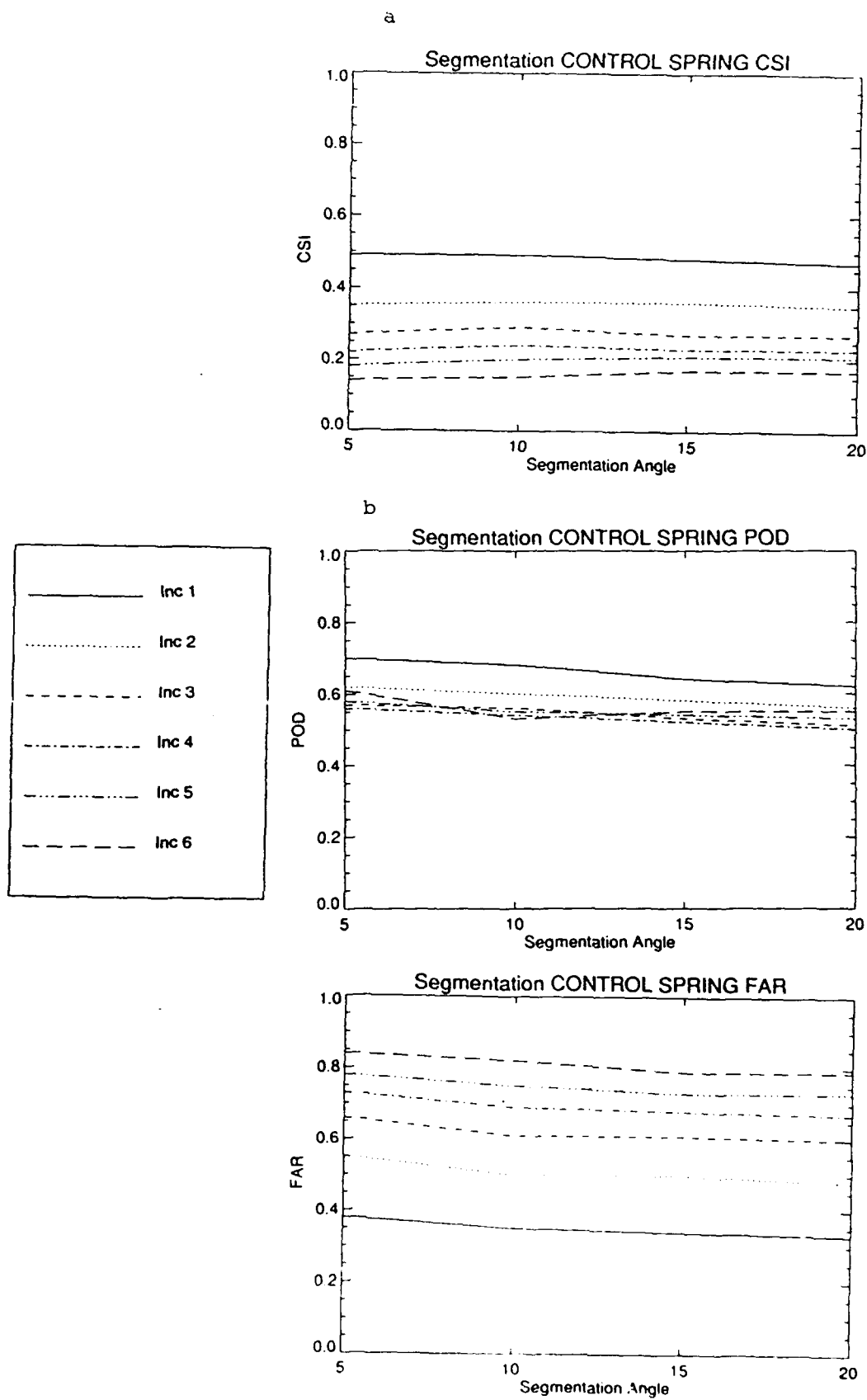


Figure 34: Same as Figure 25, except for spring.

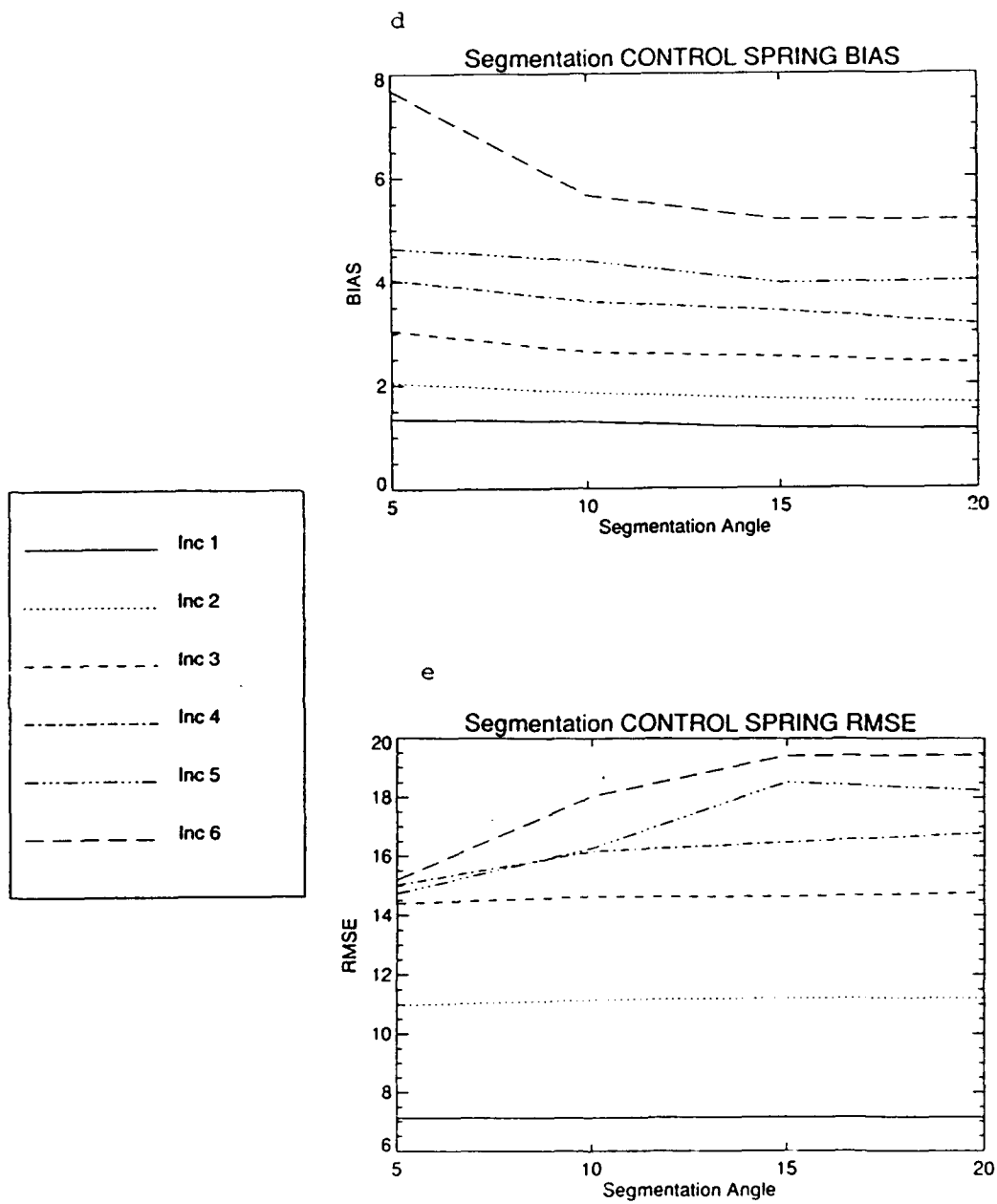


Figure 34: Same as Figure 25, except for spring.

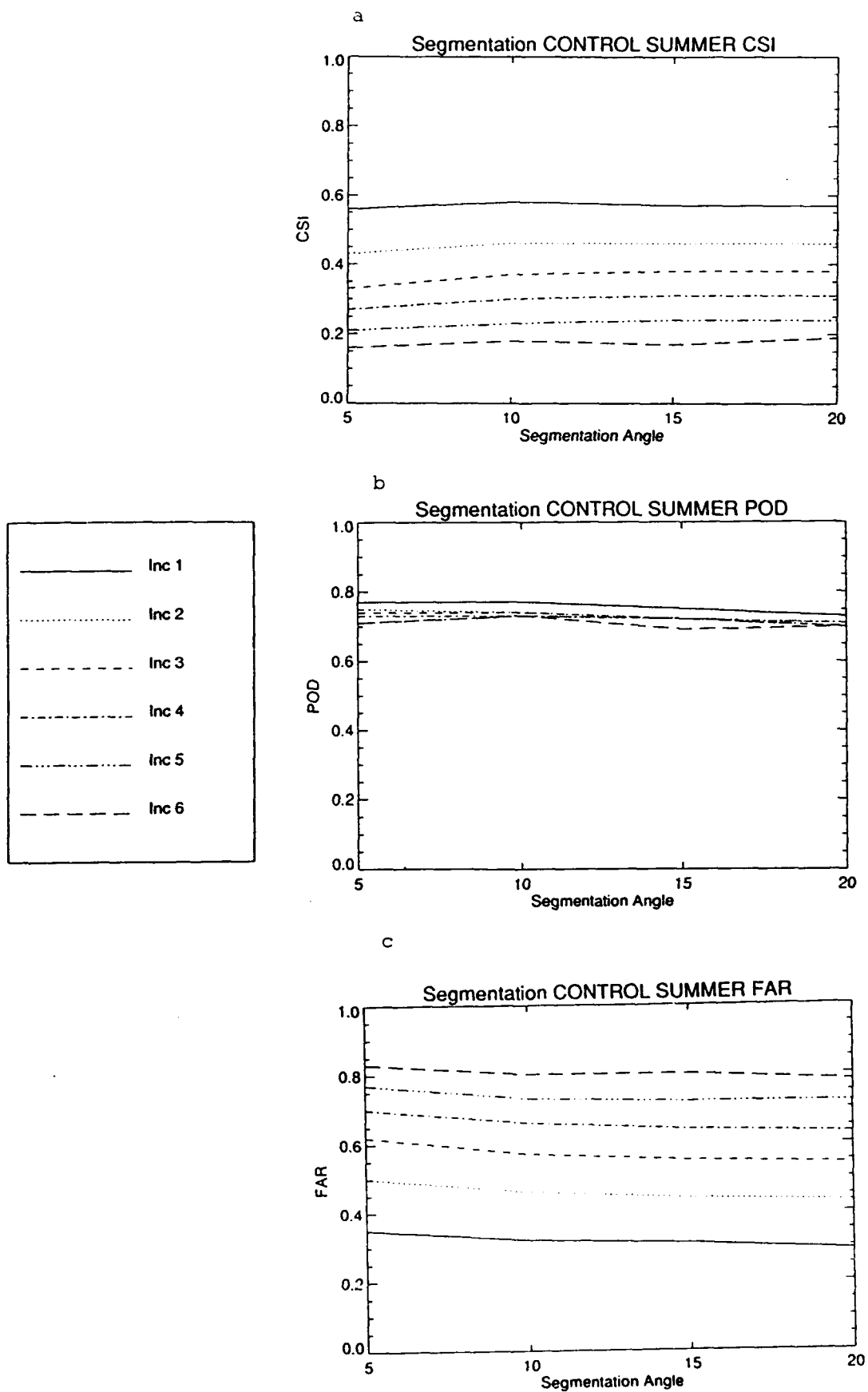


Figure 35: Same as Figure 25, except for summer.

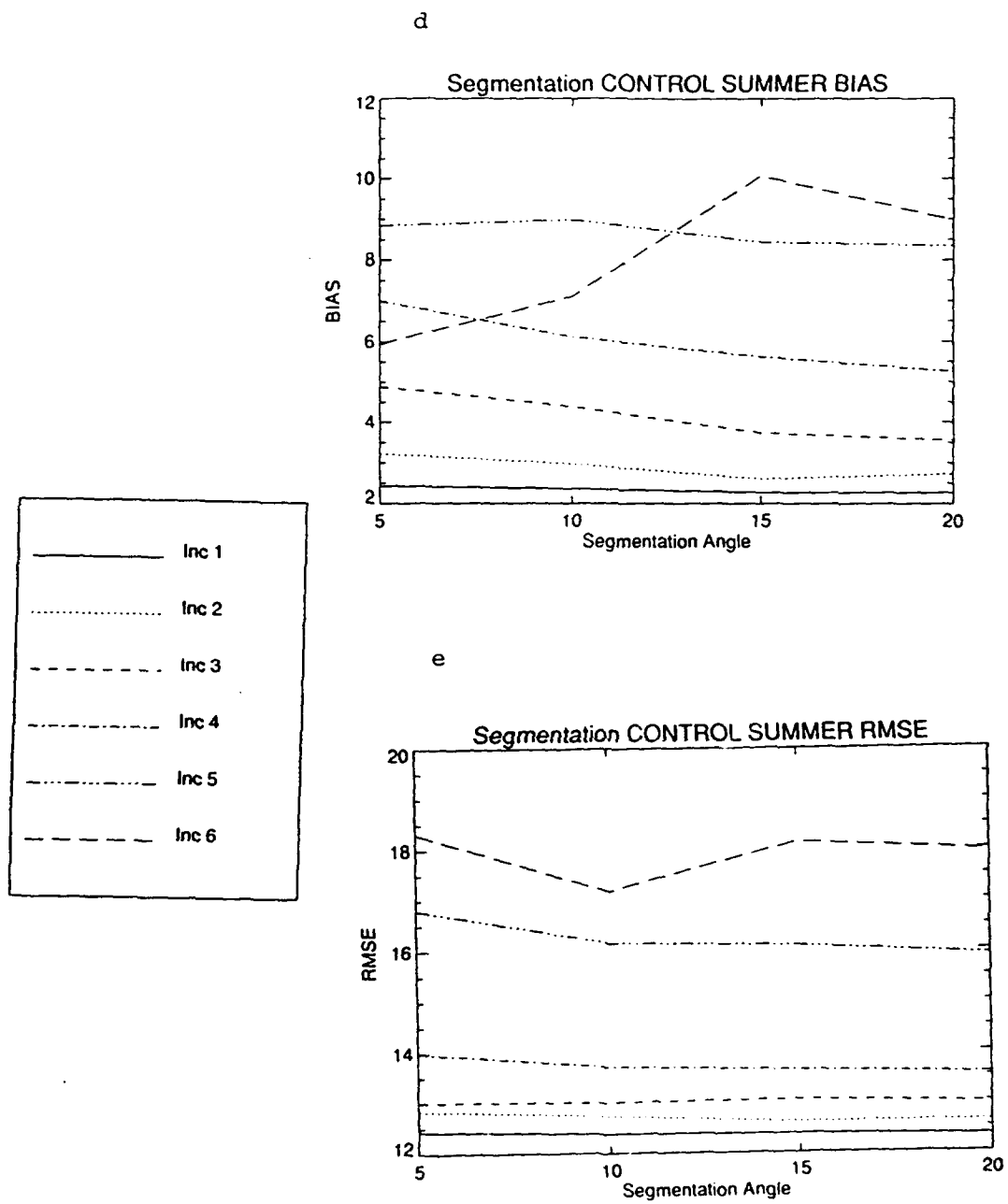


Figure 35: Same as Figure 25, except for summer.

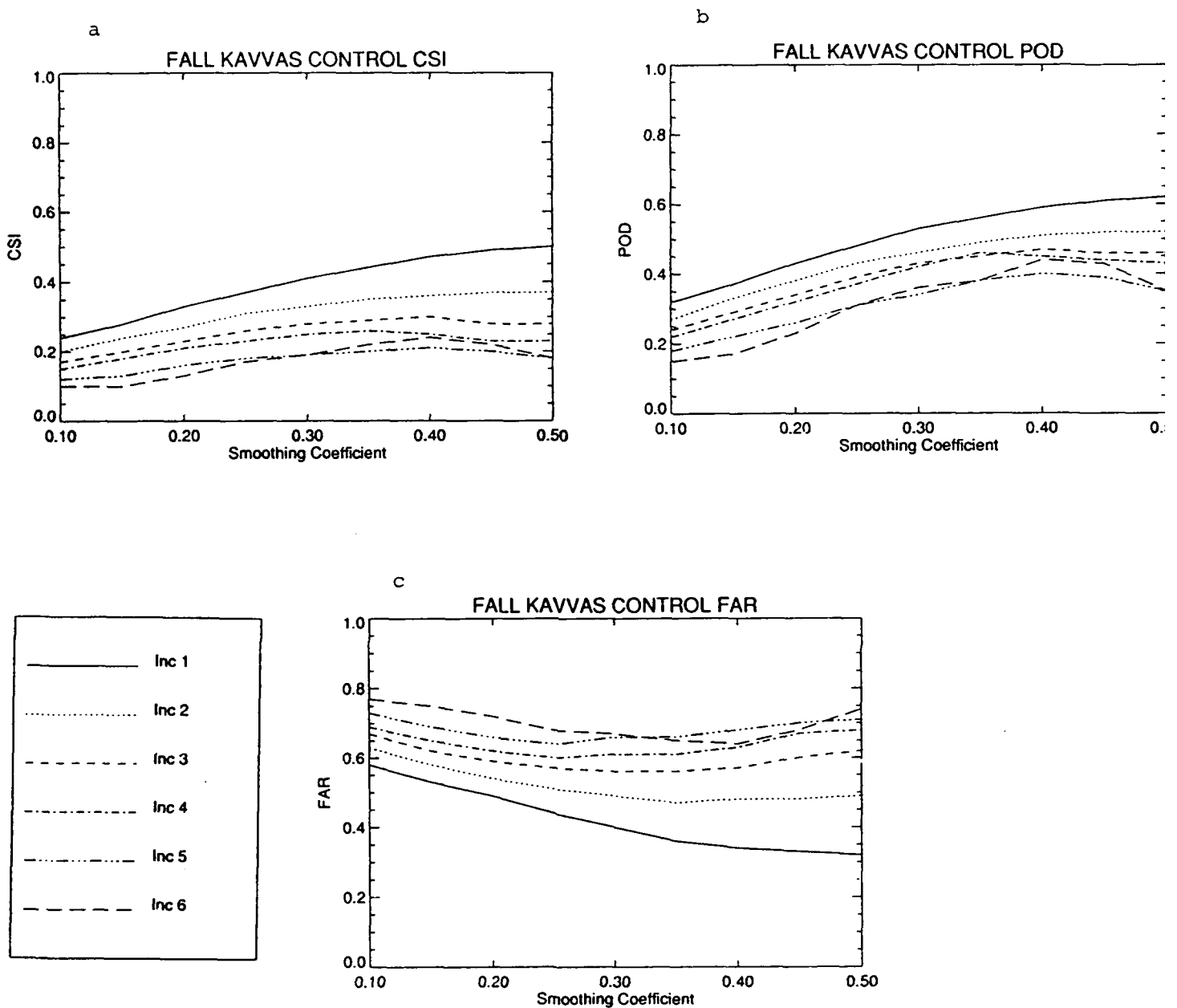


Figure 36: Verification scores for the CONTROL sample for fall, for the Kavvas method. Shown are CSI (a), POD (b), FAR (c), BIAS (d), and RMSE (e) as a function of the smoothing coefficient. The different lines correspond to different forecast increments, as in Figure 12.

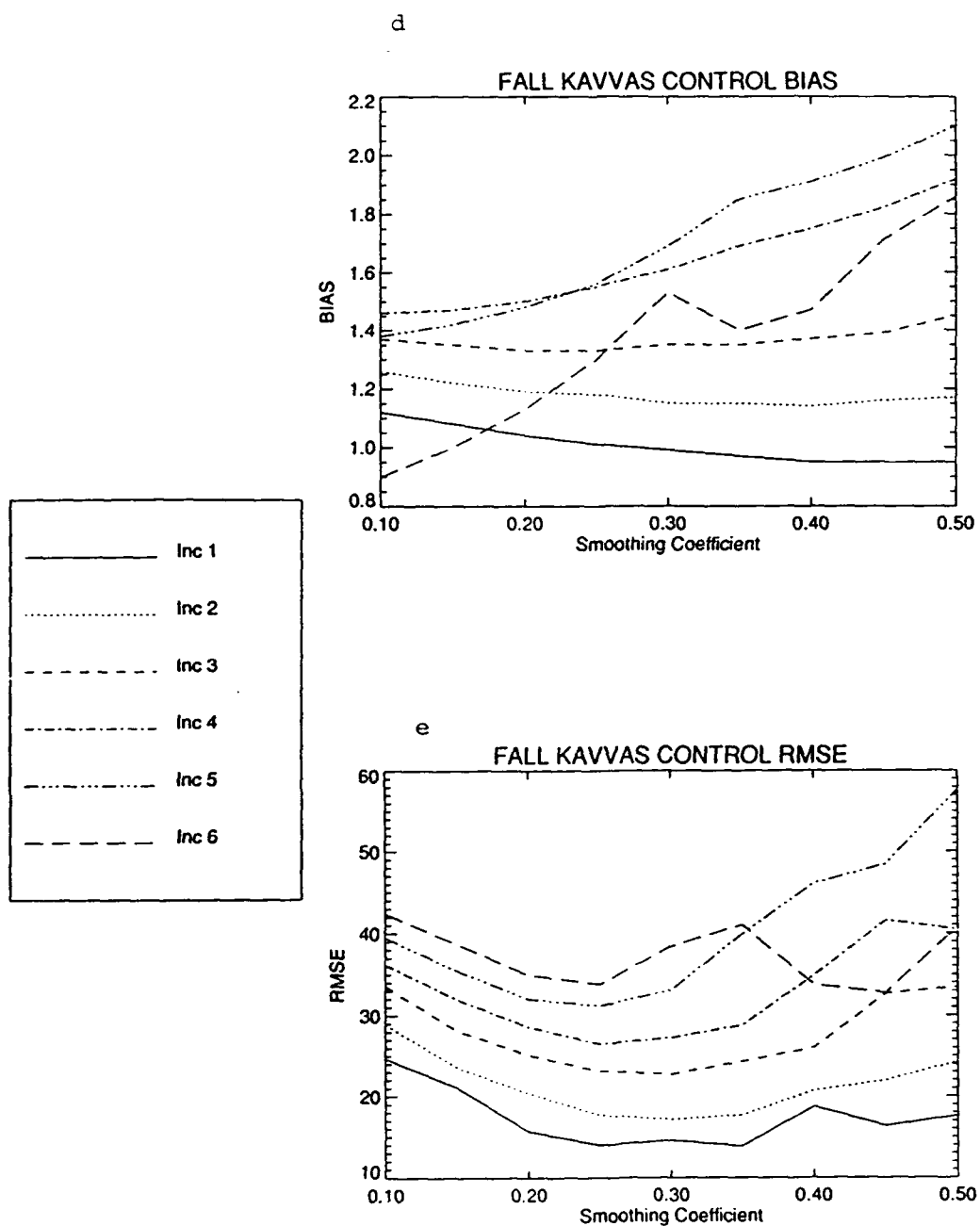


Figure 36: Verification scores for the CONTROL sample for fall, for the Kavvas method. Shown are CSI (a), POD (b), FAR (c), BIAS (d), and RMSE (e) as a function of the smoothing coefficient. The different lines correspond to different forecast increments, as in Figure 12.



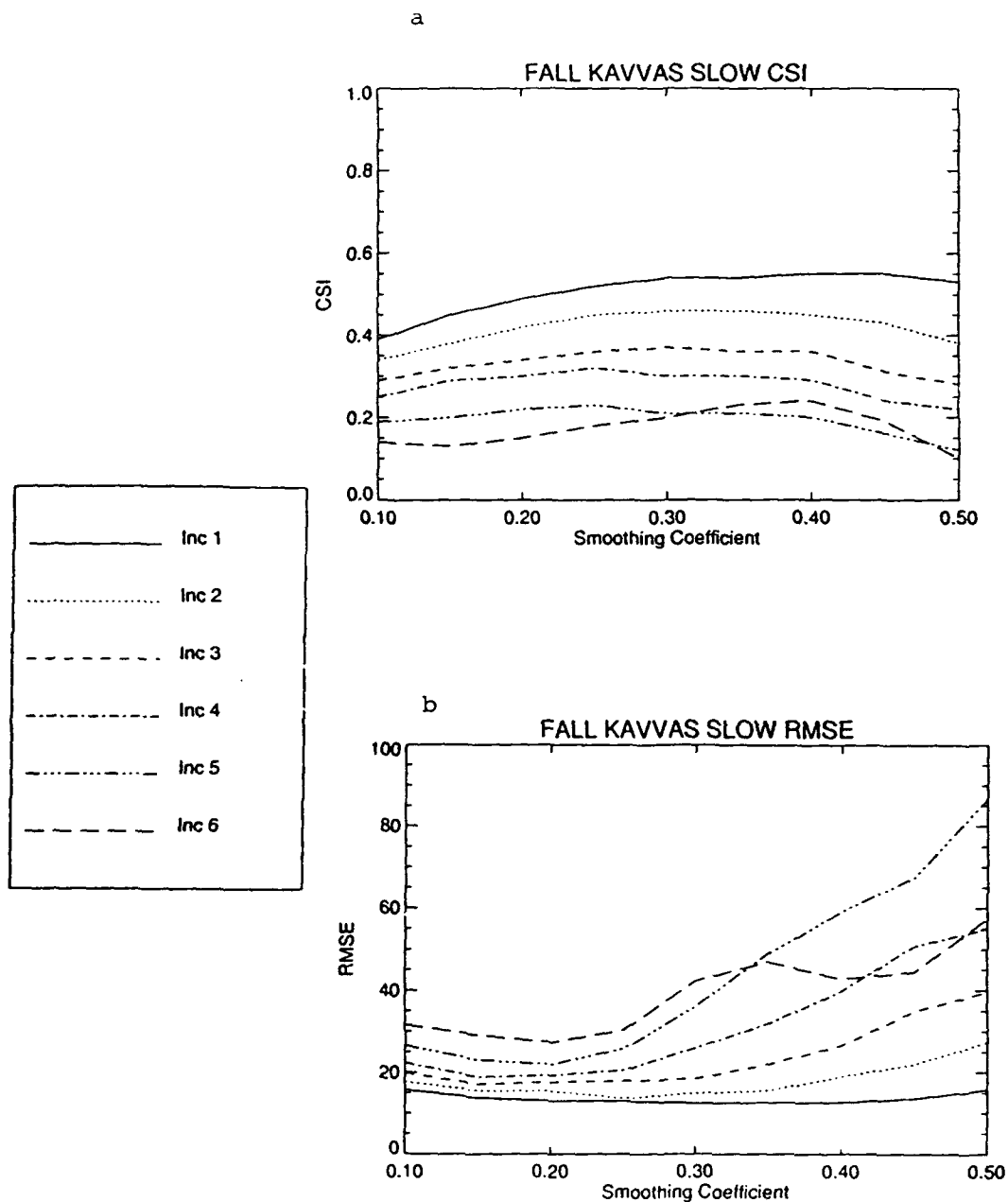


Figure 37: Verification scores for the SLOW feature sample for fall, for the Kavvas method. Shown are CSI (a) and RMSE (b) as a function of the smoothing coefficient. The different lines correspond to different forecast increments, as in Figure 12.

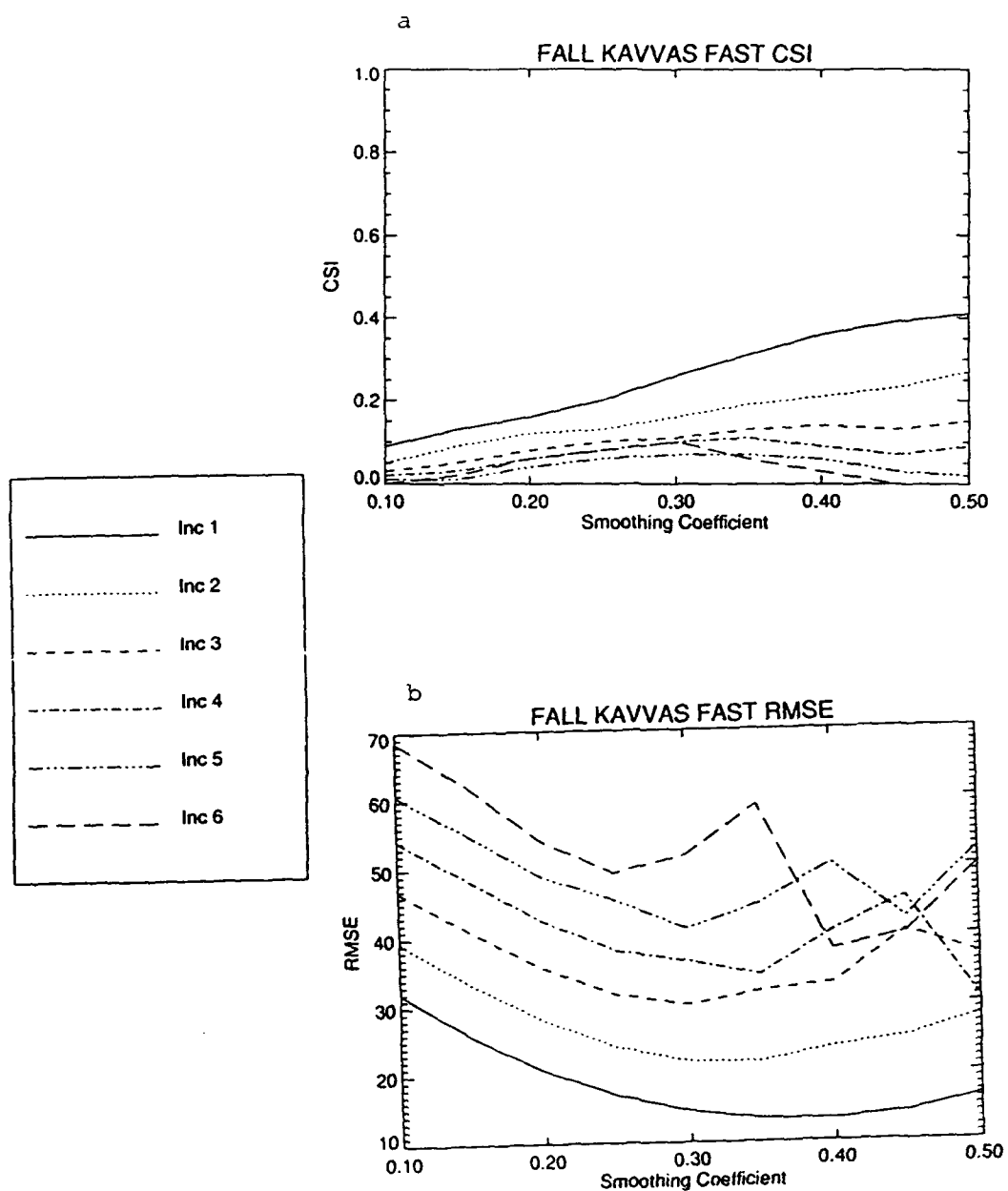


Figure 38: Same as Figure 37, except for the FAST feature subsample.

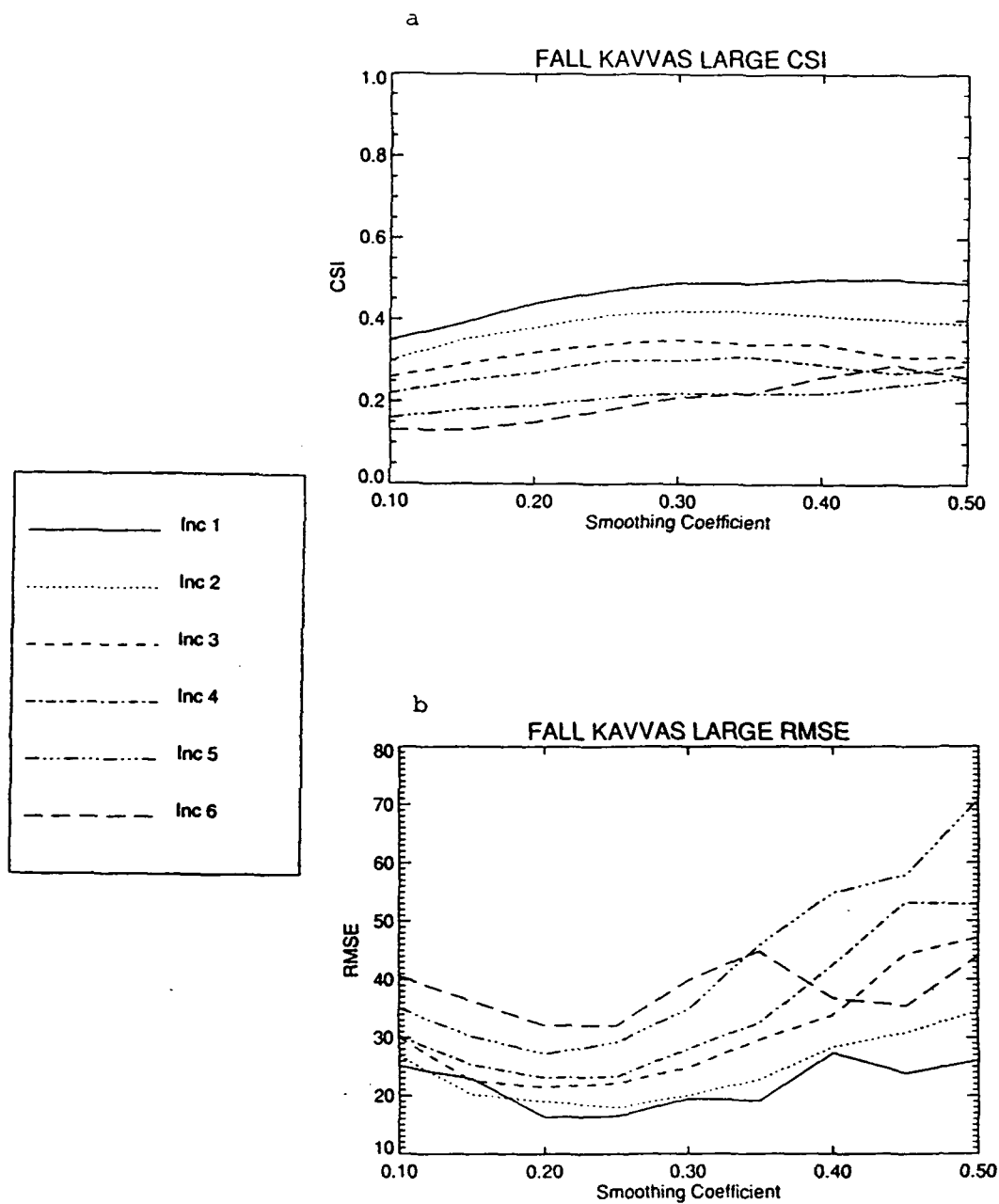


Figure 39: Same as Figure 37, except for the LARGE feature subsample.

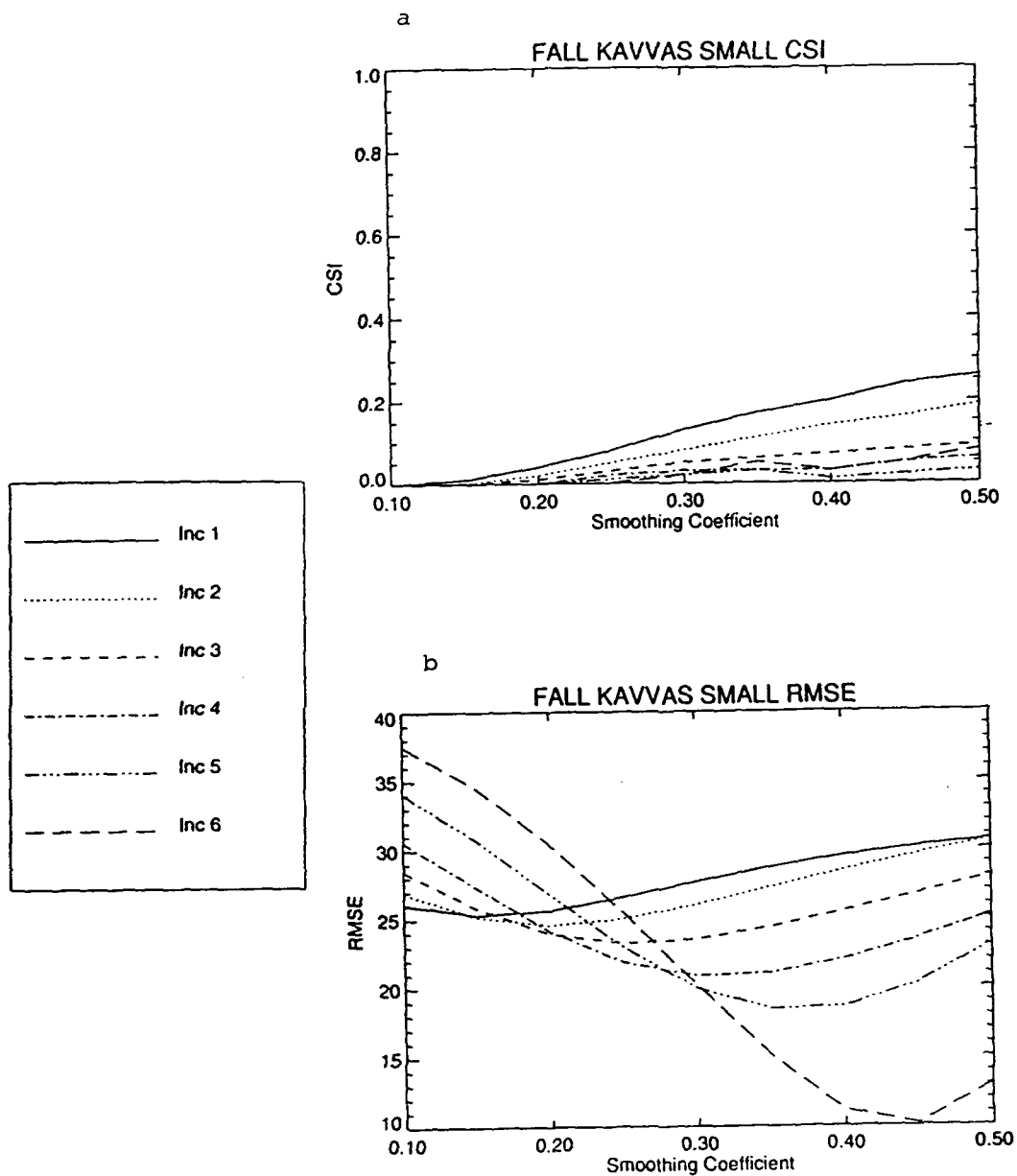


Figure 40: Same as Figure 37, except for the SMALL feature subsample.

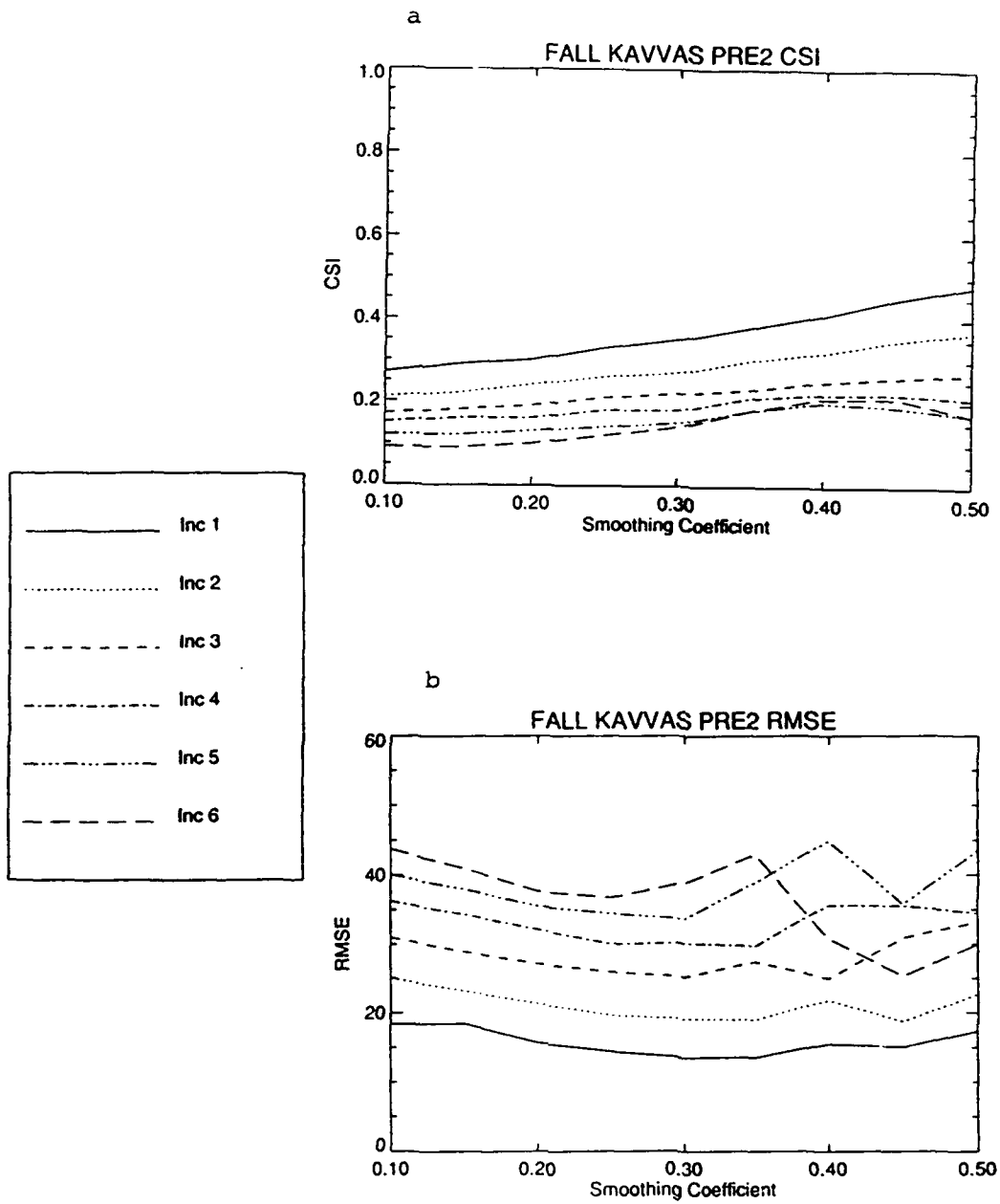


Figure 41: Same as Figure 37, except for the PRE2 subsample.

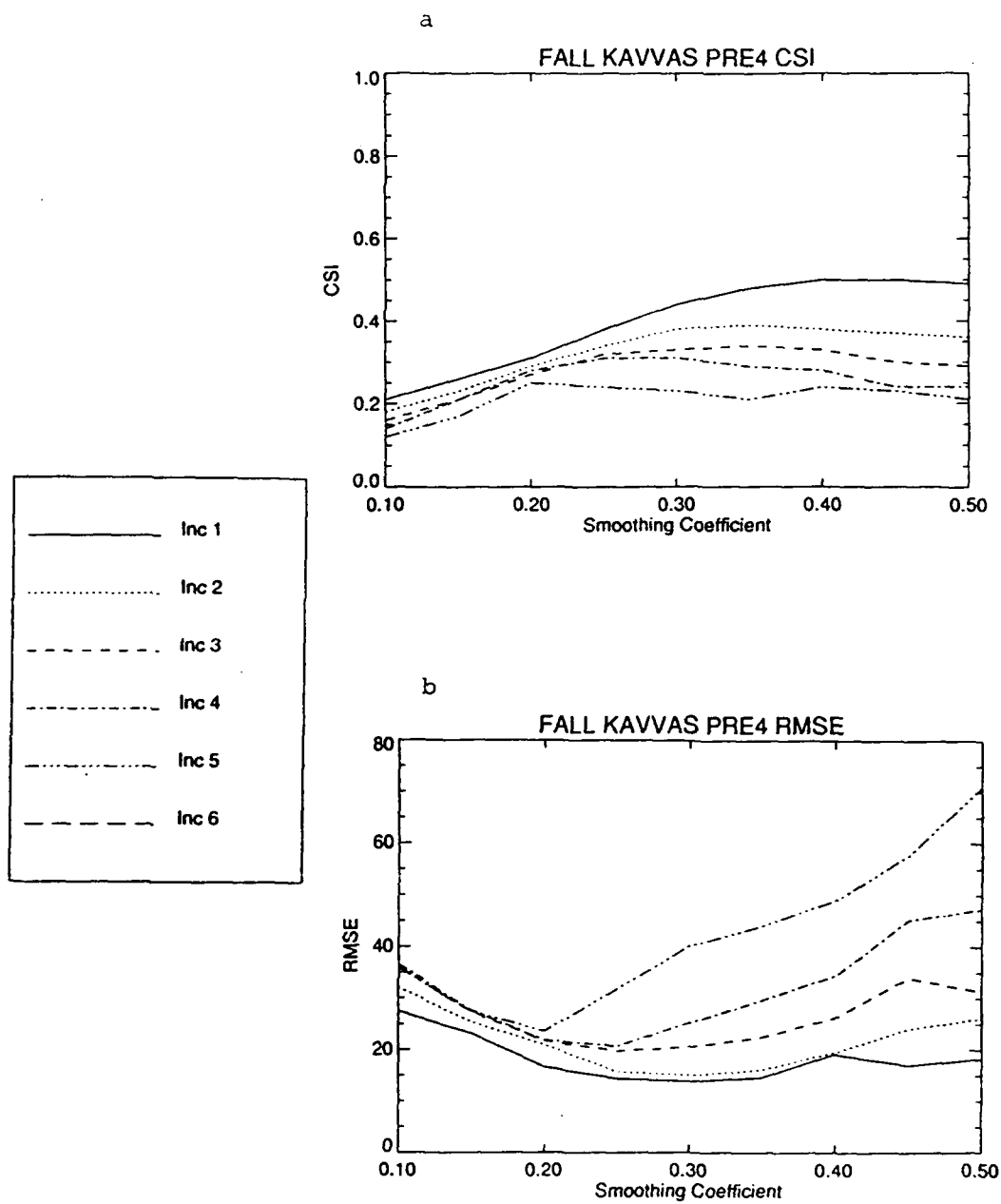


Figure 42: Same as Figure 37, except for the PRE4 subsample.

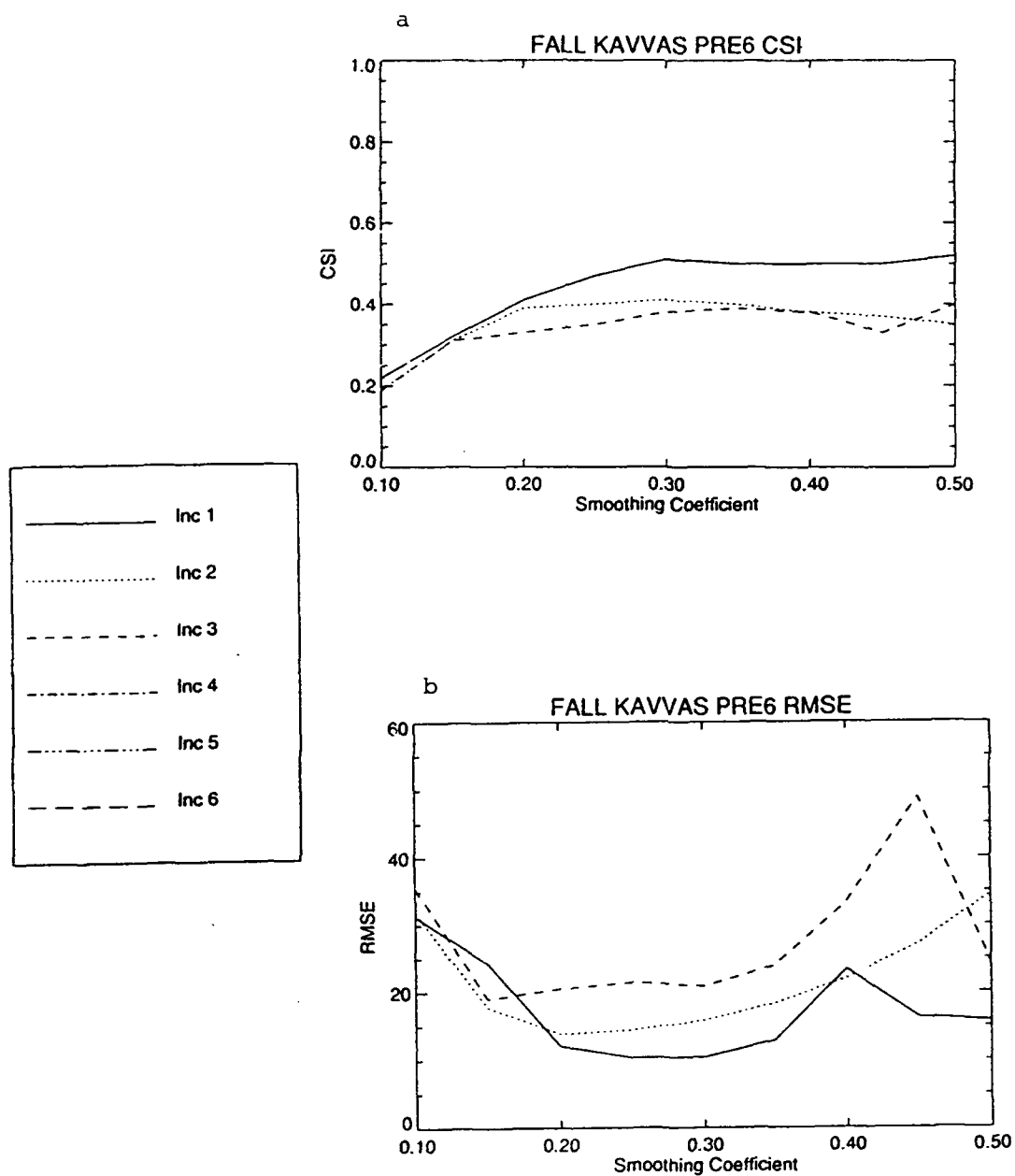


Figure 43: Same as Figure 37, except for the PRE6 subsample.

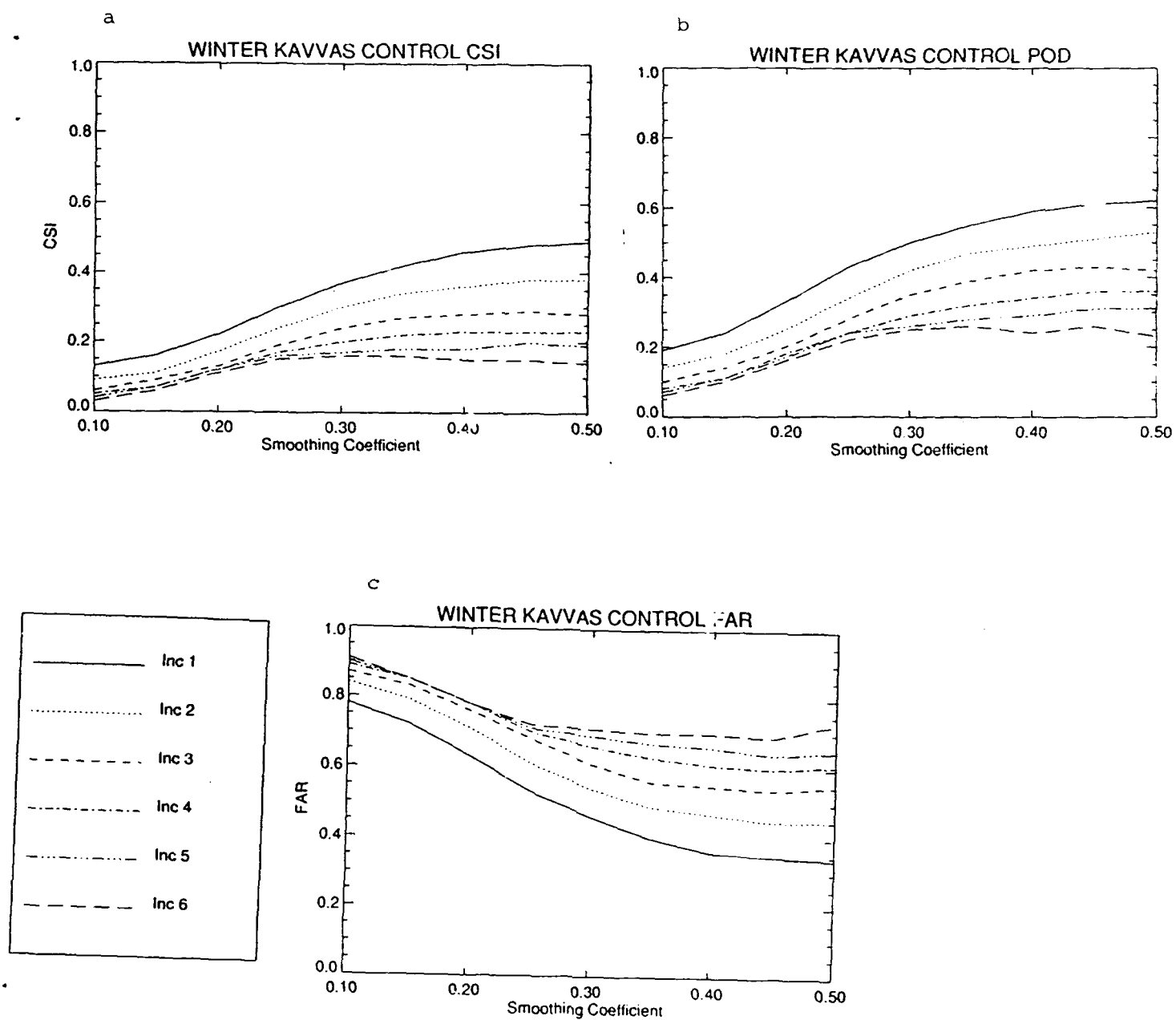


Figure 44: Same as Figure 36, except for winter.



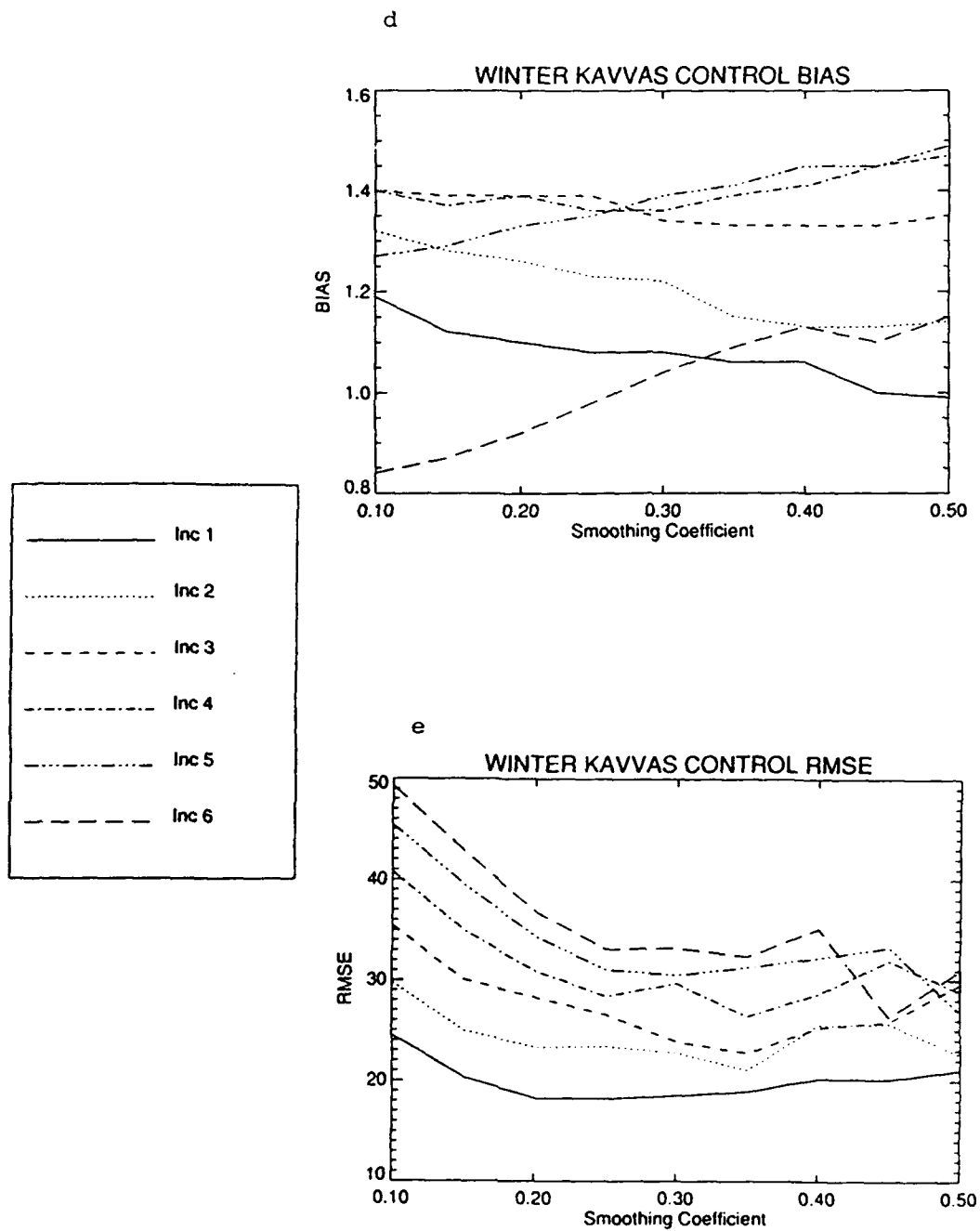


Figure 44: Same as Figure 36, except for winter.

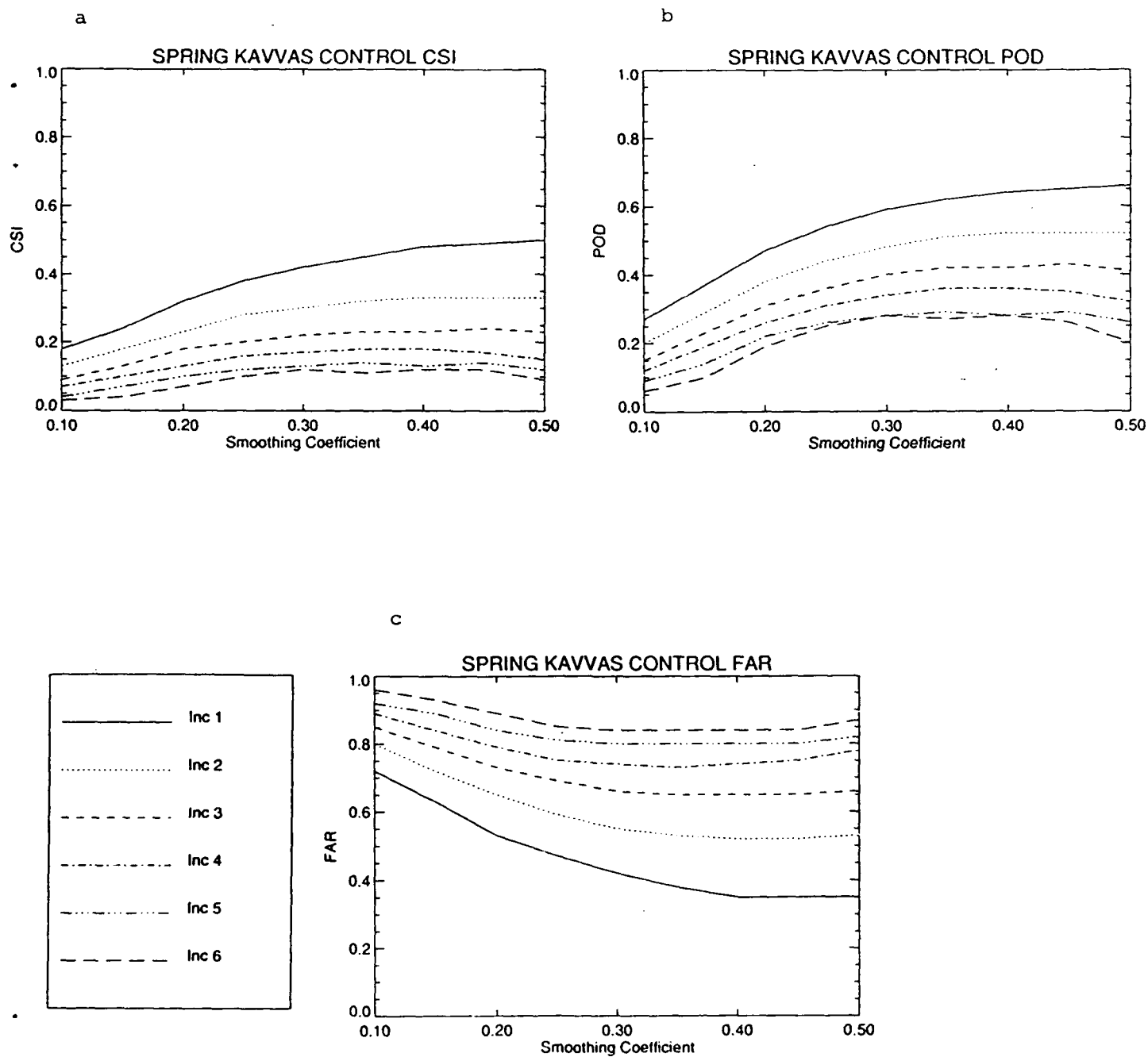
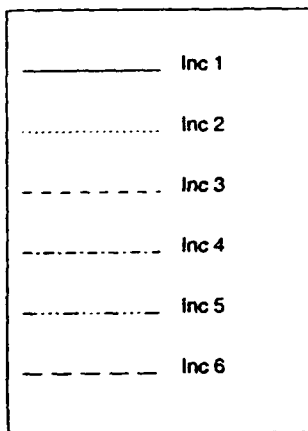
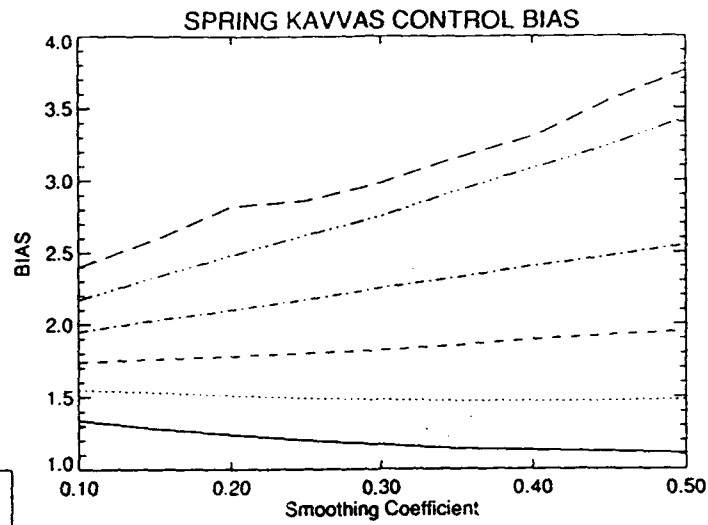


Figure 45: Same as Figure 36, except for spring.

d



e

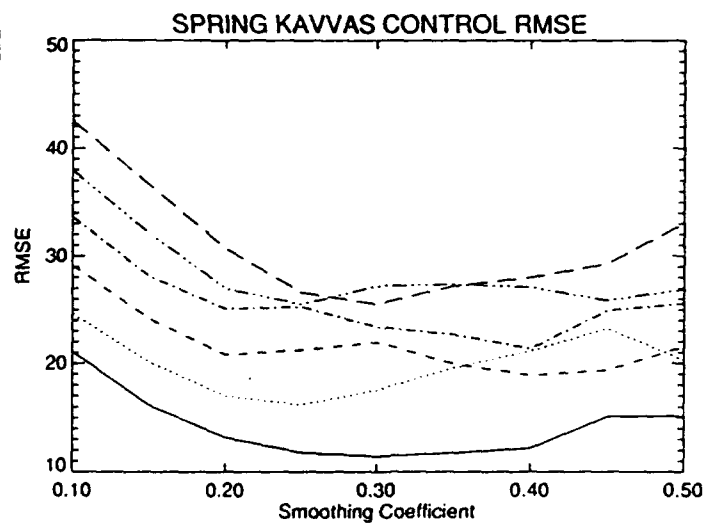


Figure 45: Same as Figure 36, except for spring.

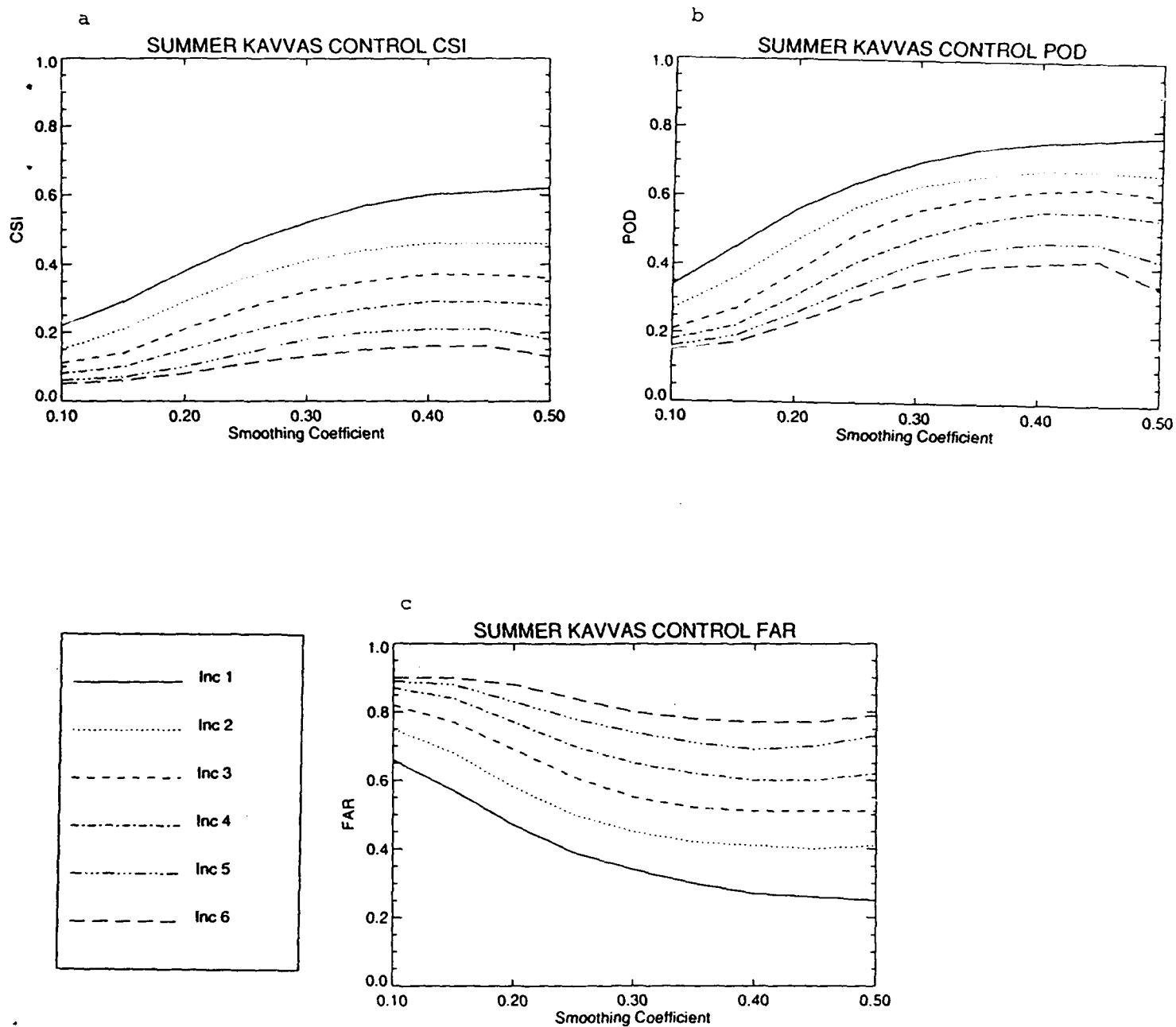


Figure 46: Same as Figure 36, except for summer.

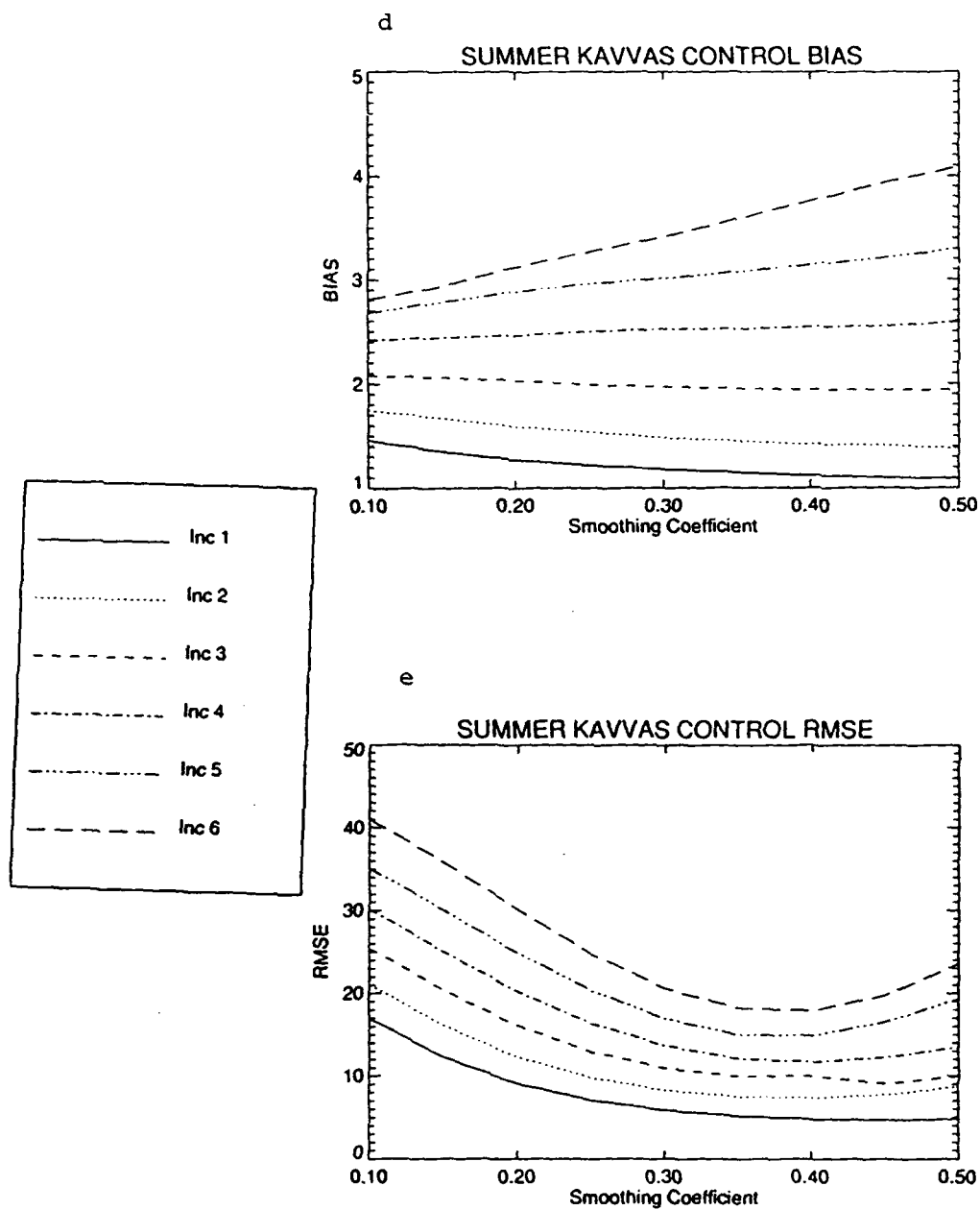


Figure 46: Same as Figure 36, except for summer.

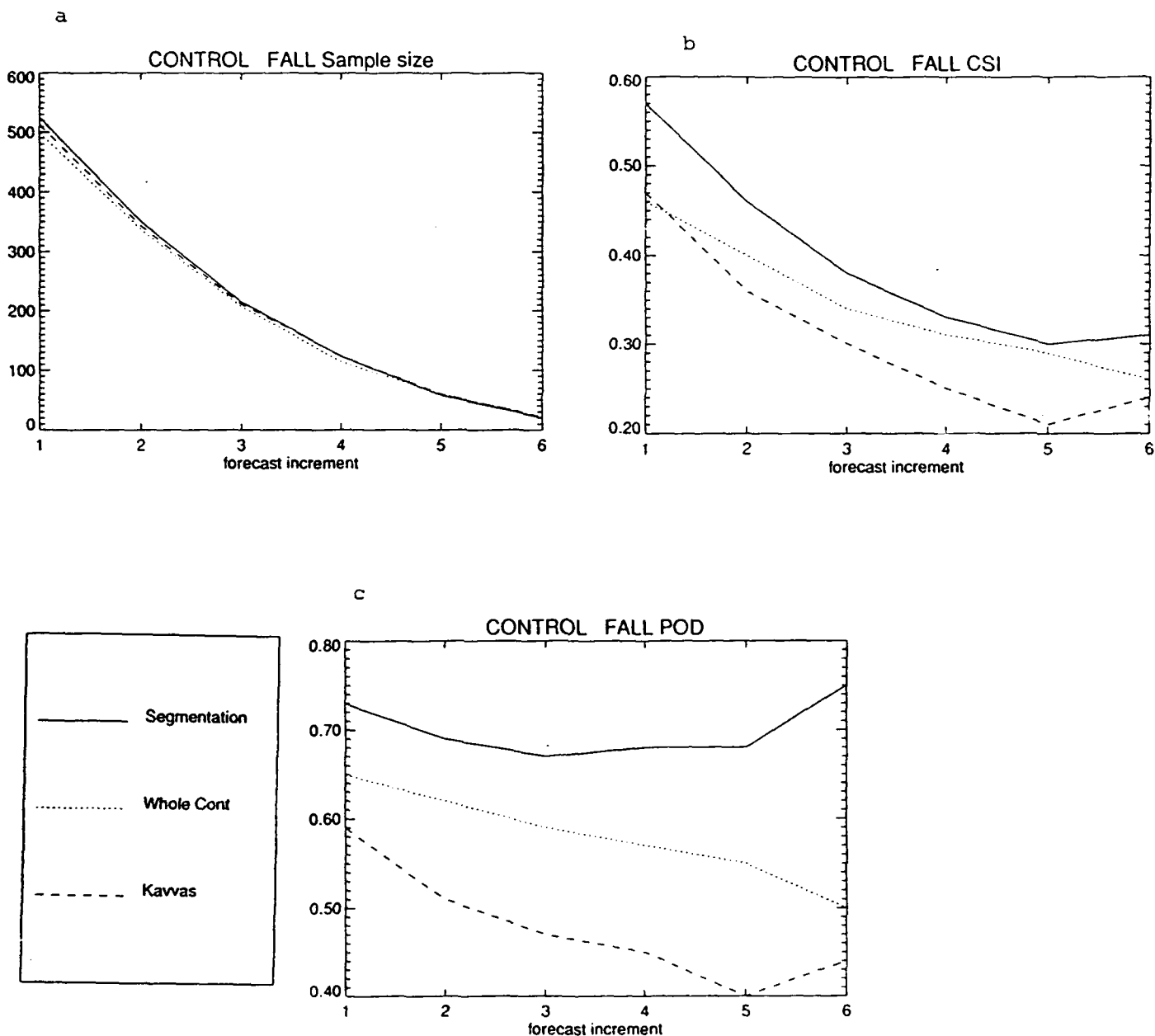
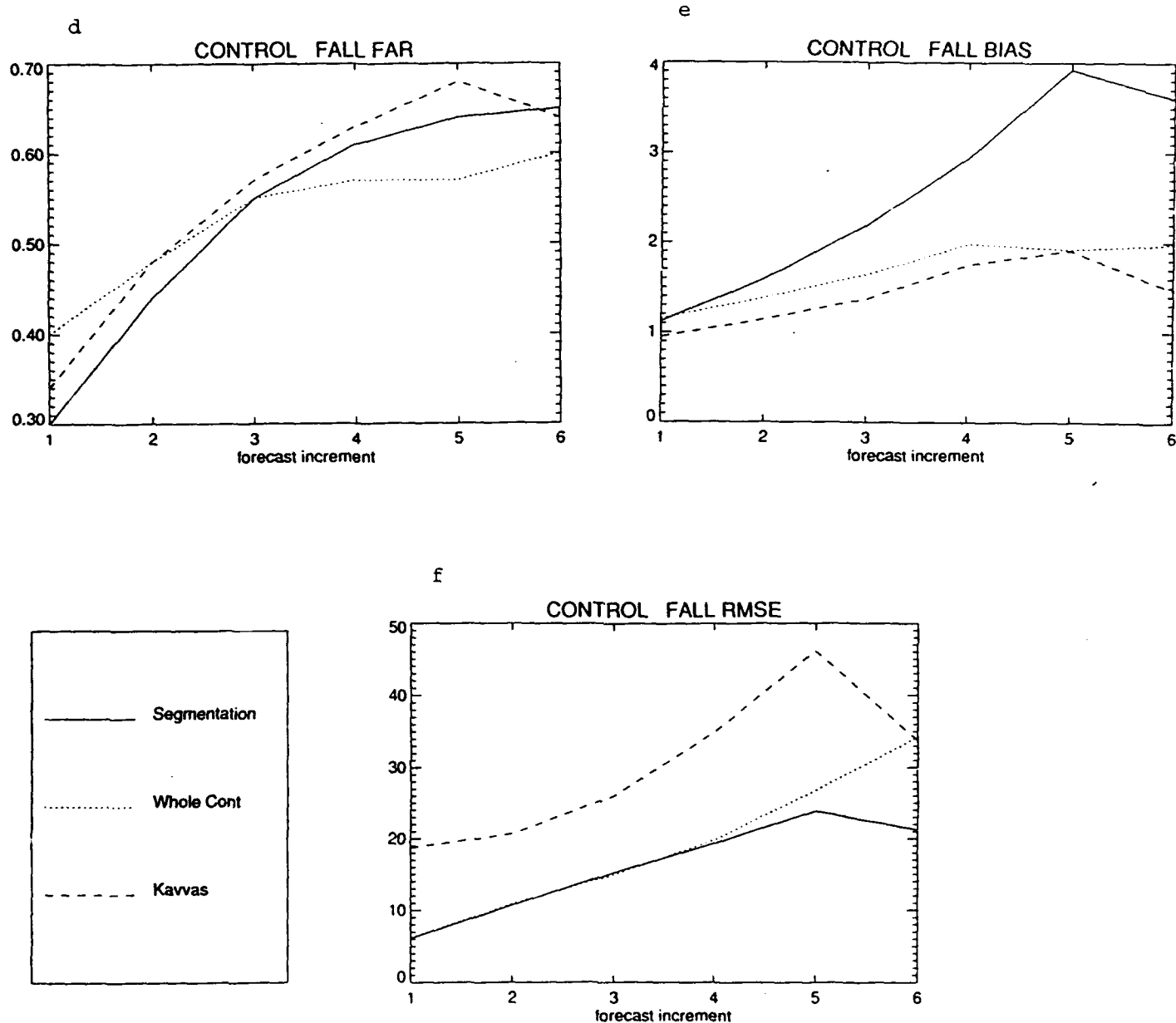


Figure 47: Verification scores for the CONTROL sample for fall as a function of forecast increment. Shown are the sample size (a), CSI (b), POD (c), FAR (d), BIAS (e), and RMSE (f). The different lines correspond to different forecast techniques: segmentation (solid), whole contour (dotted), Kavvas (dashed).



**Figure 47: Verification scores for the CONTROL sample for fall as a function of forecast increment. Shown are the sample size (a), CSI (b), POD (c), FAR (d), BIAS (e), and RMSE (f). The different lines correspond to different forecast techniques: segmentation (solid), whole contour (dotted), Kavvas (dashed).**

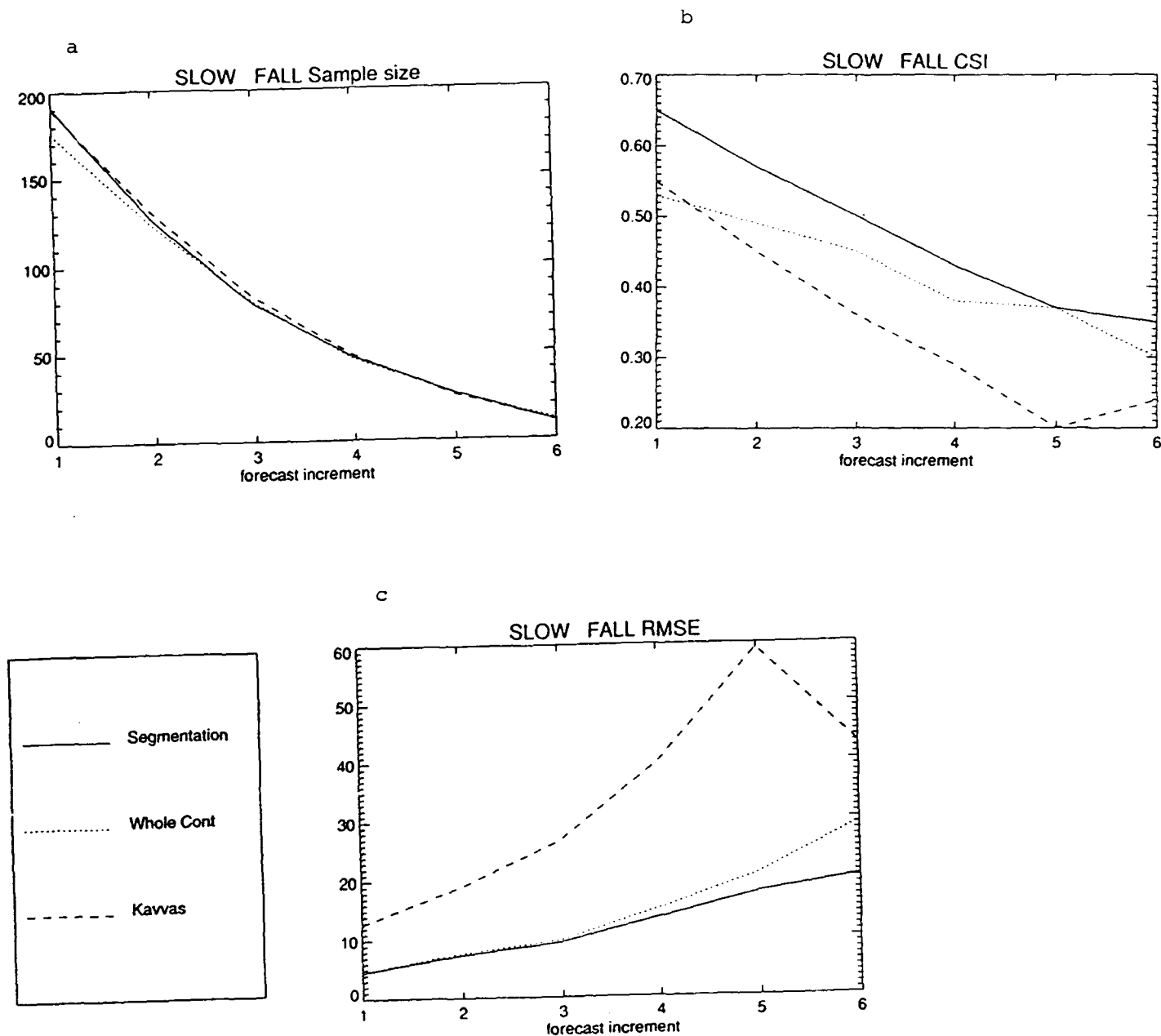


Figure 48: Verification scores for the SLOW feature subsample for fall as a function of forecast increment. Shown are the sample size (a), CSI (b), and RMSE (c). The different lines correspond to different forecast techniques, as in Figure 47.



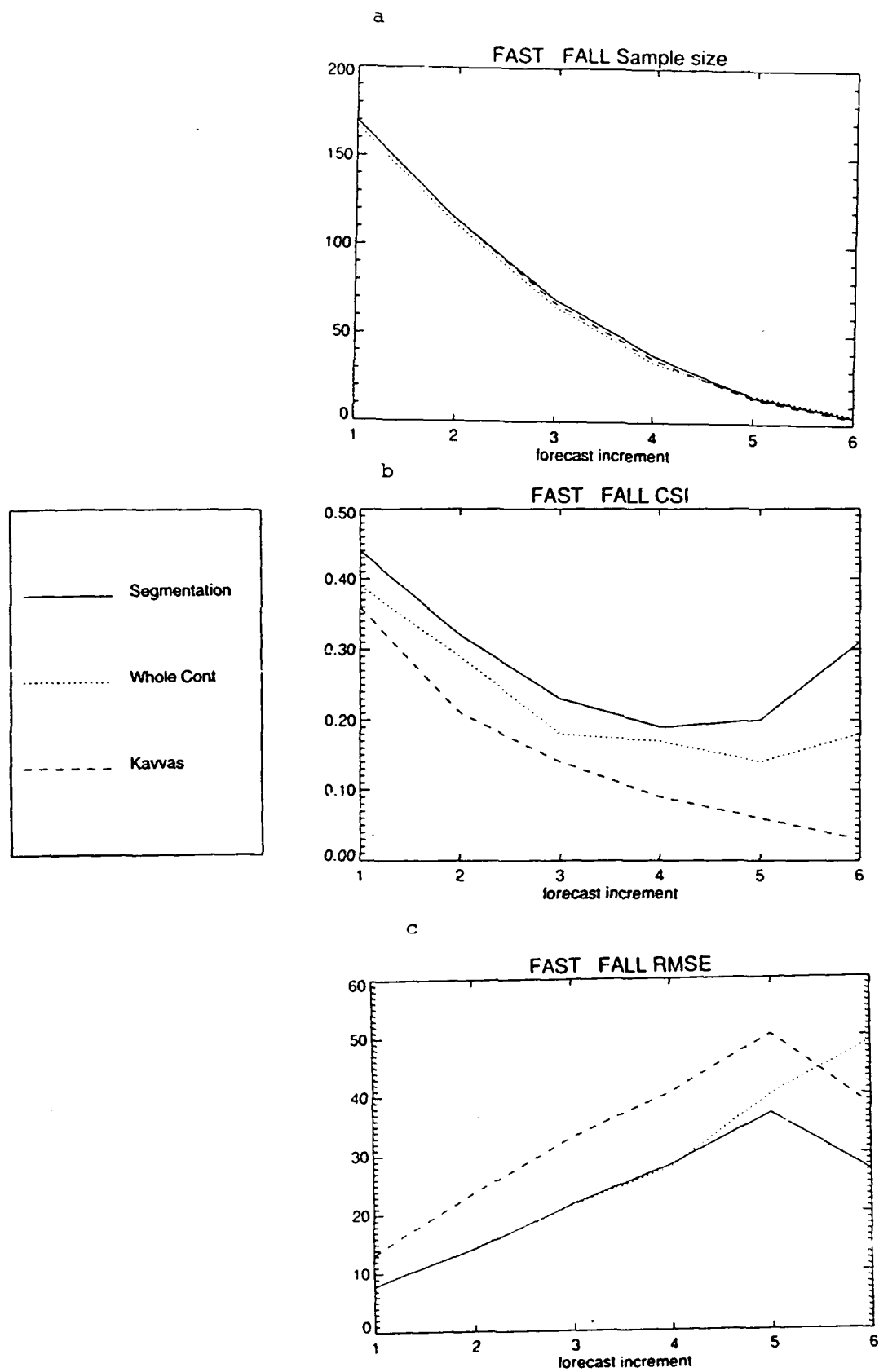


Figure 49: Same as Figure 48, except for the FAST feature subsample.

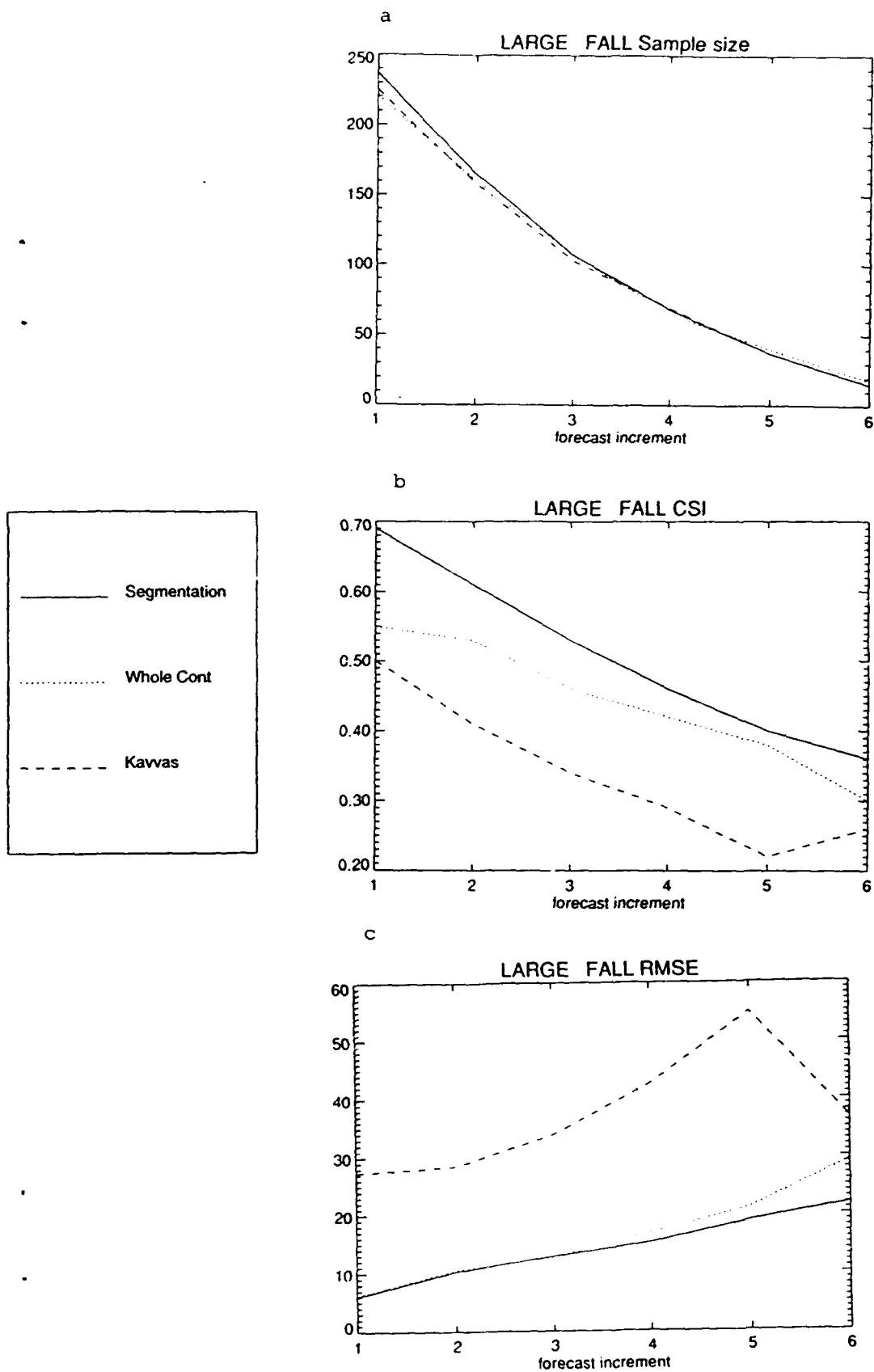


Figure 50: Same as Figure 48, except for the LARGE feature subsample.

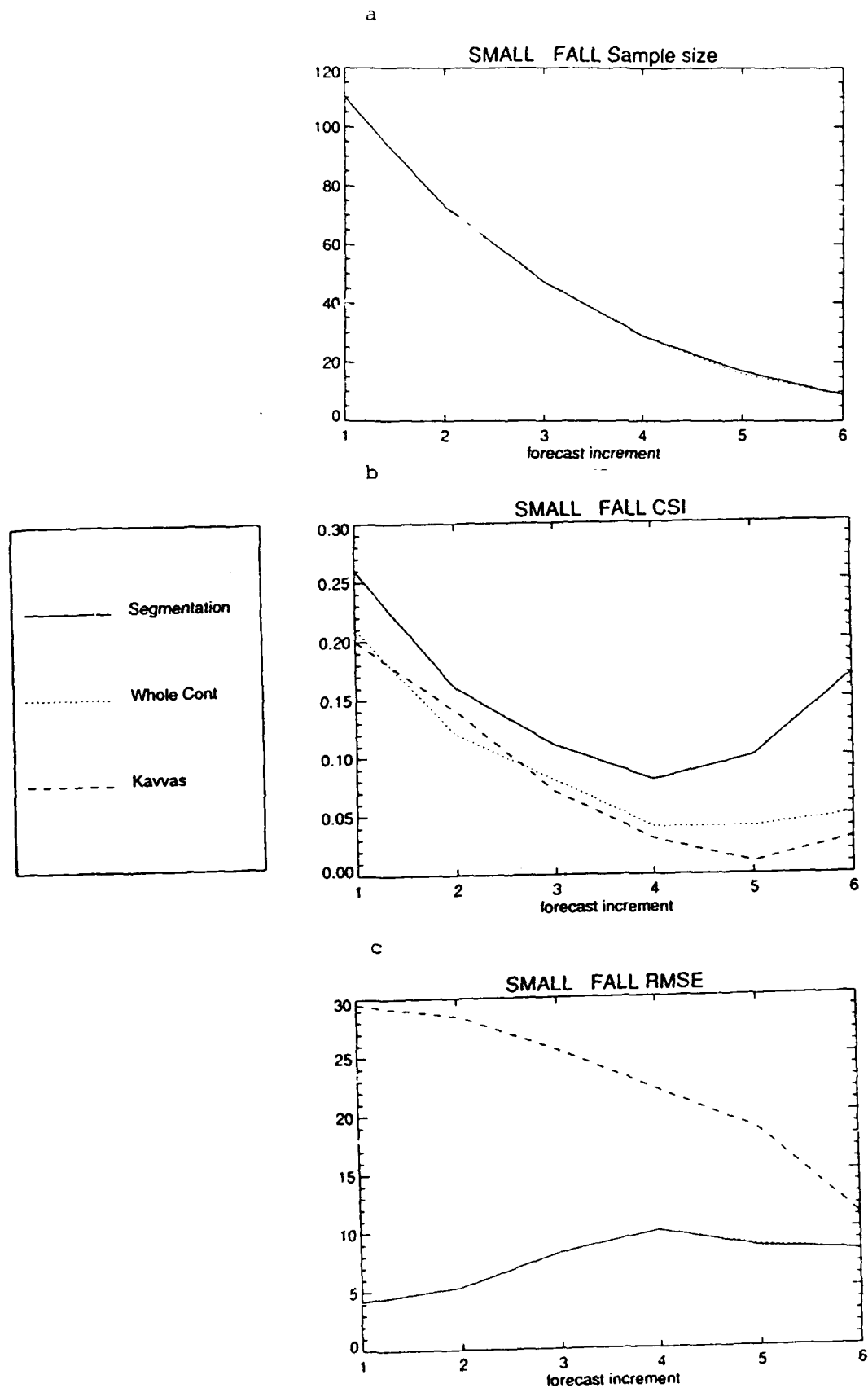


Figure 51: Same as Figure 48, except for the SMALL feature subsample.

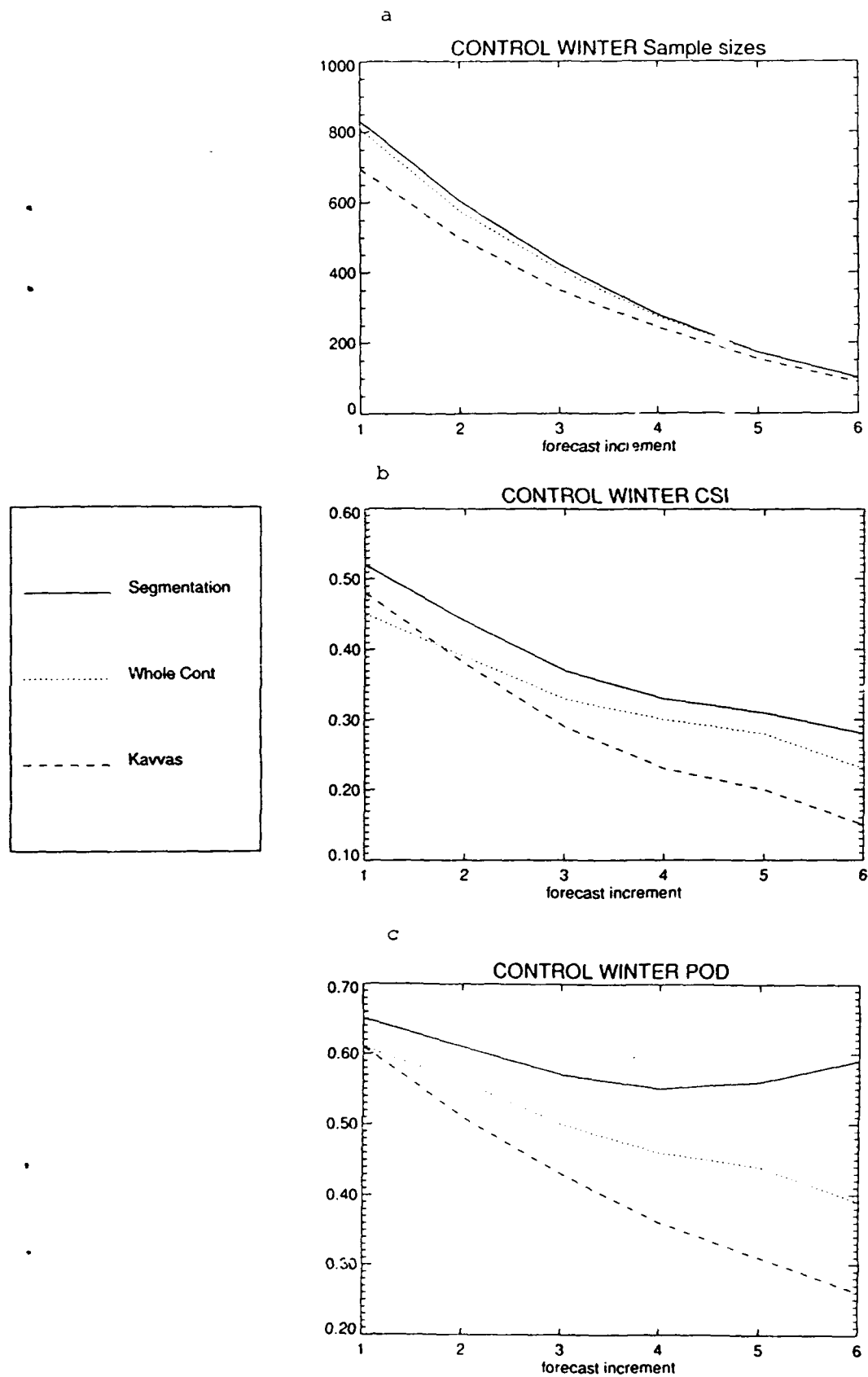


Figure 52: Same as Figure 47, except for winter.

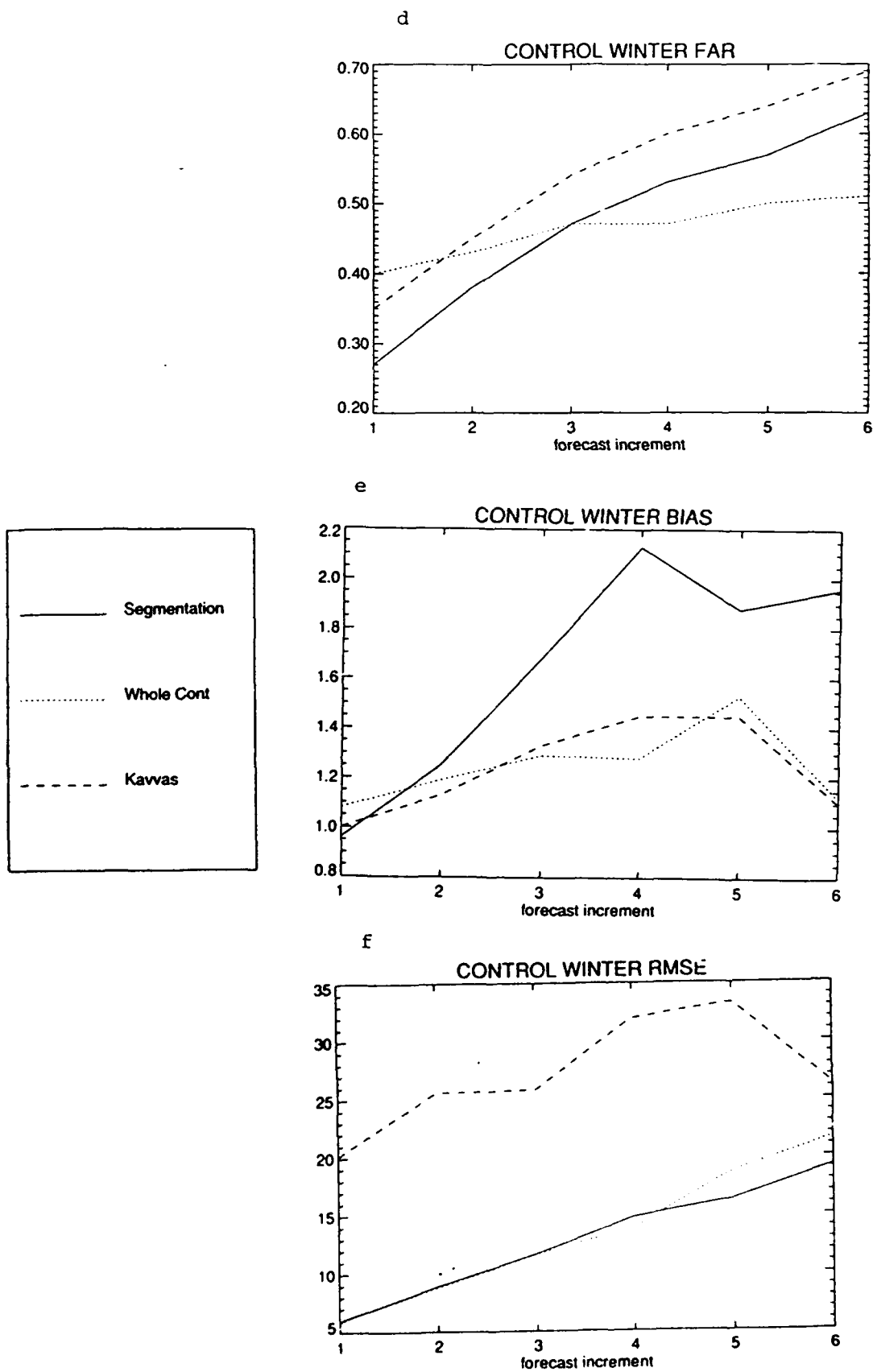


Figure 52: Same as Figure 47, except for winter.

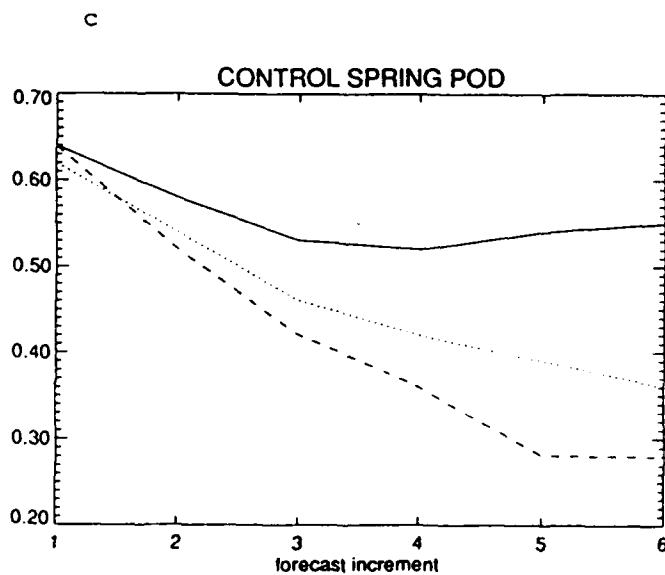
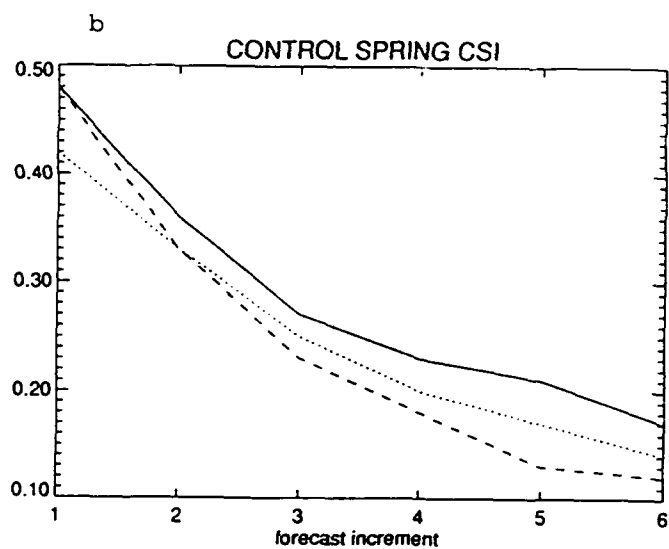
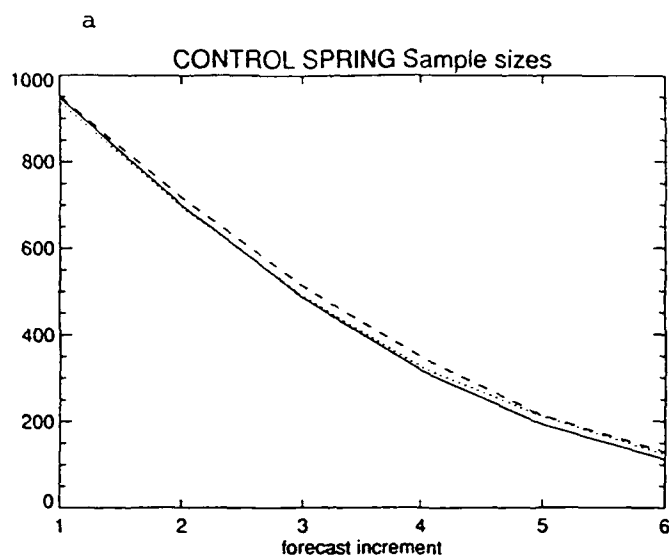
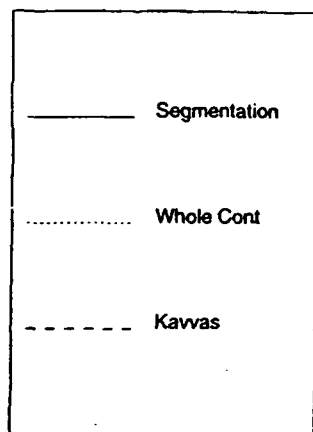


Figure 53: Same as Figure 47, except for spring.

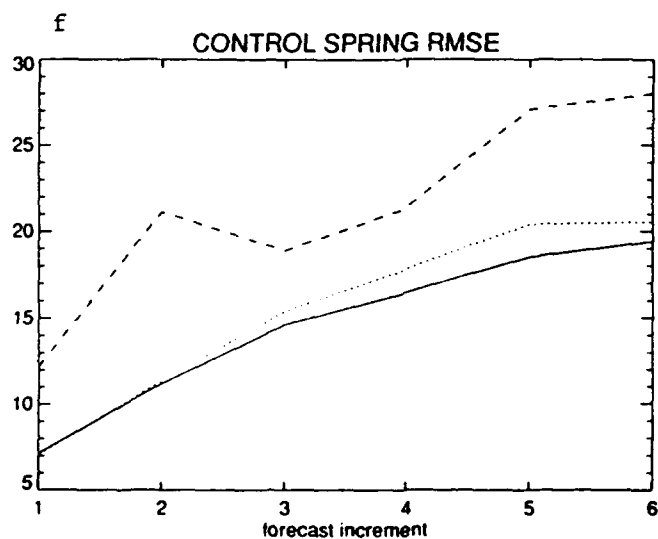
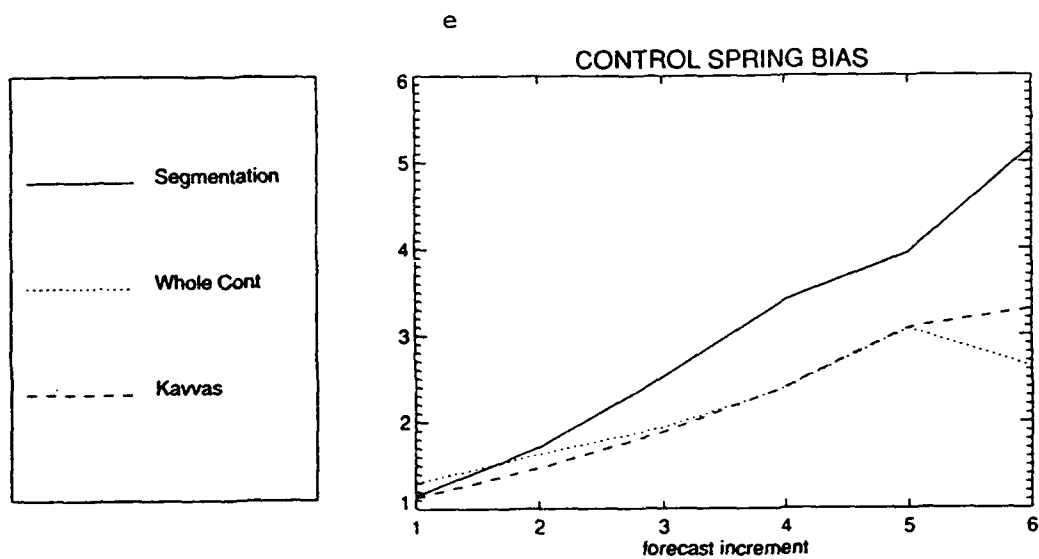
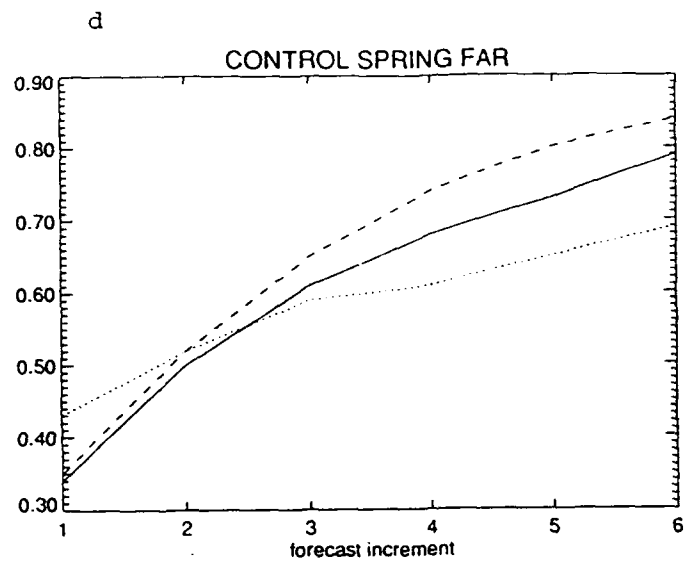


Figure 53: Same as Figure 47, except for spring.

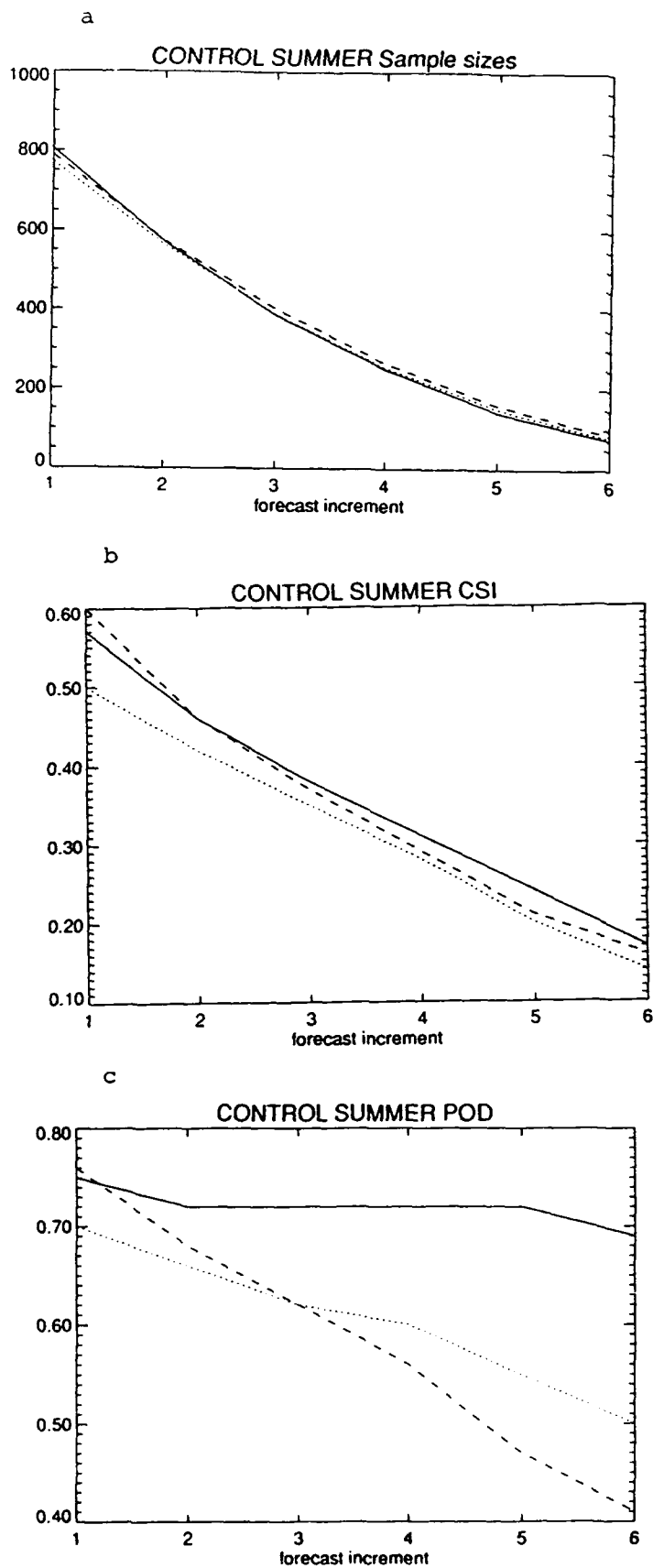
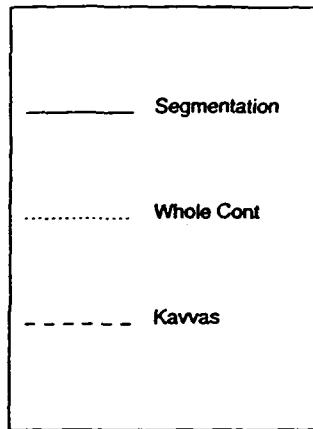


Figure 54: Same as Figure 47, except for summer.



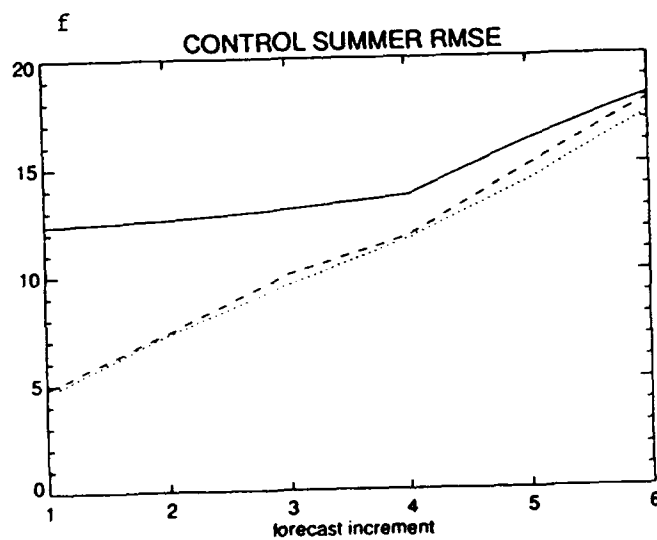
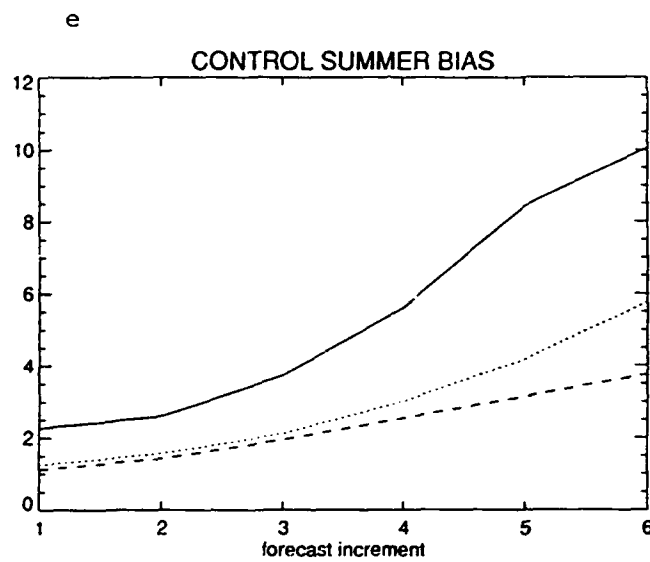
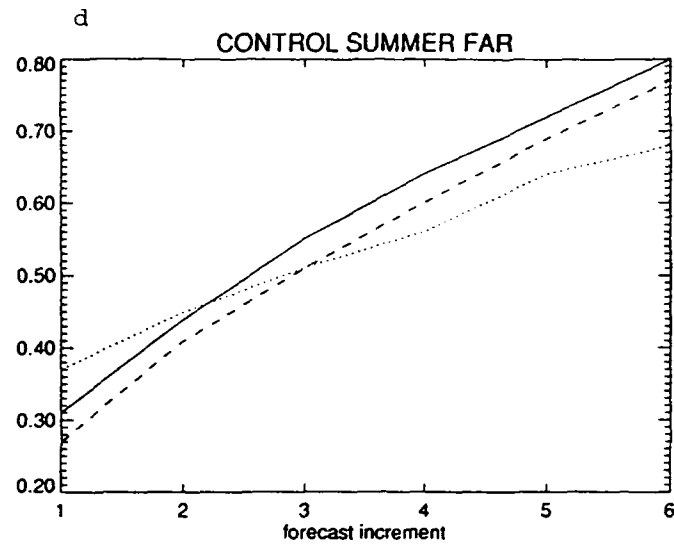


Figure 54: Same as Figure 47, except for summer.

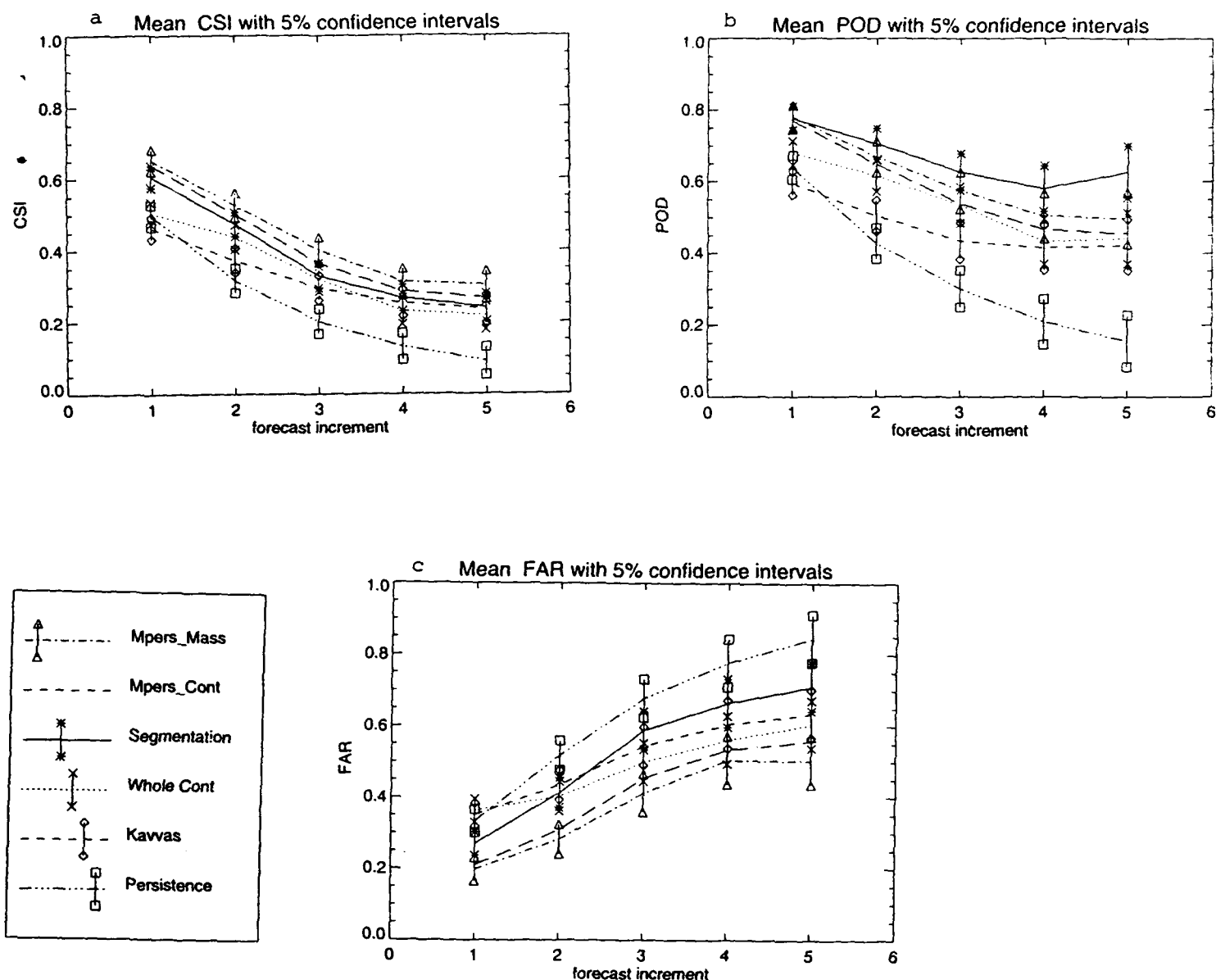


Figure 55: Mean verification scores with 5% confidence intervals from the ANOVA for the CONTROL sample for the whole year as a function of forecast increment. Shown are the CSI (a), POD (b), and FAR (c). The different lines, and symbols used for the confidence intervals, correspond to different forecast techniques: segmentation (solid, asterisk), whole contour (dotted, X), Kavvas (dashed, diamond), and persistence (dash-dot-dot-dot, square), movable persistence based on the center of mass (dash-dot, triangle), and based on the mean contour position (long dashes, confidence intervals omitted for clarity).

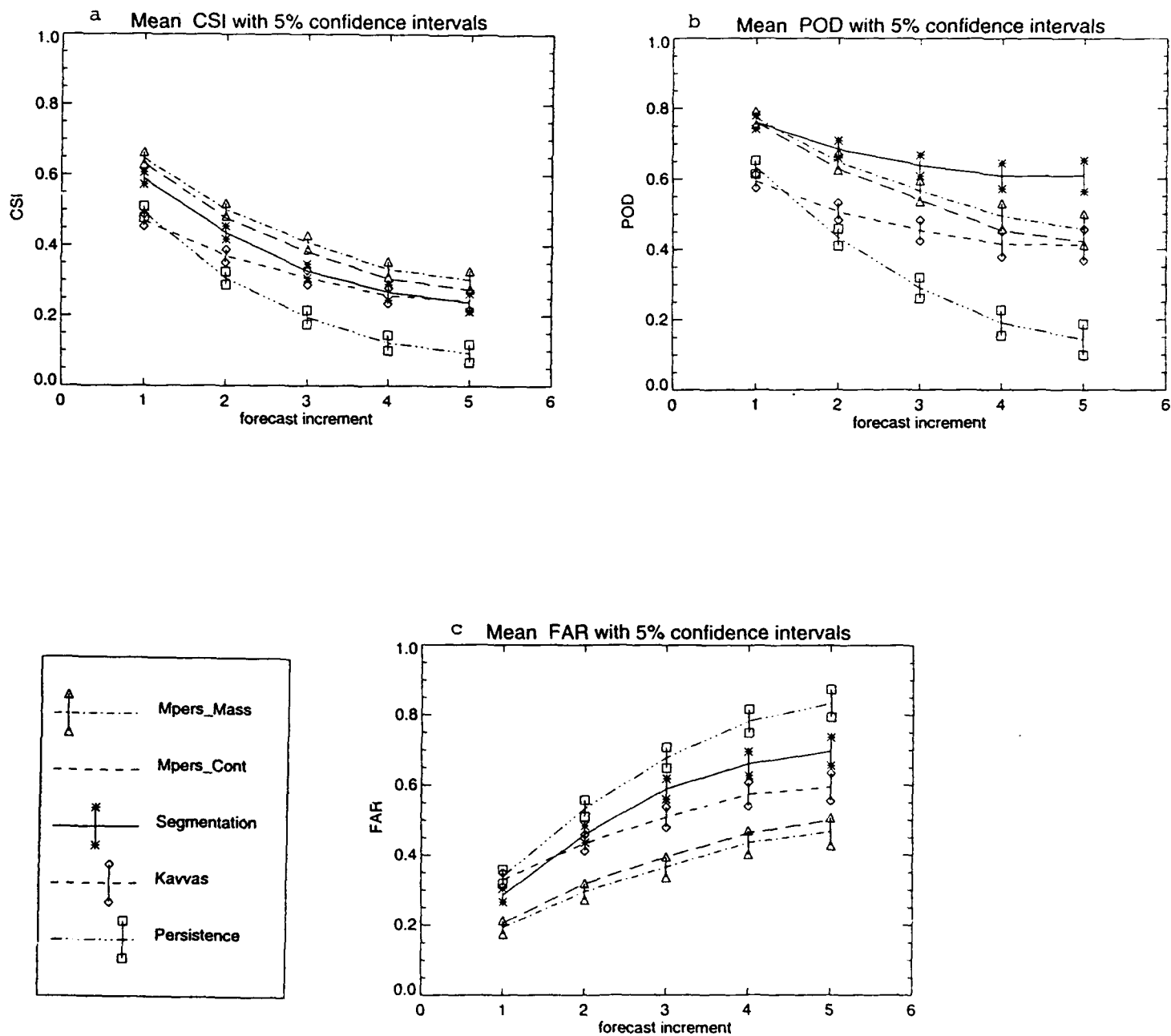
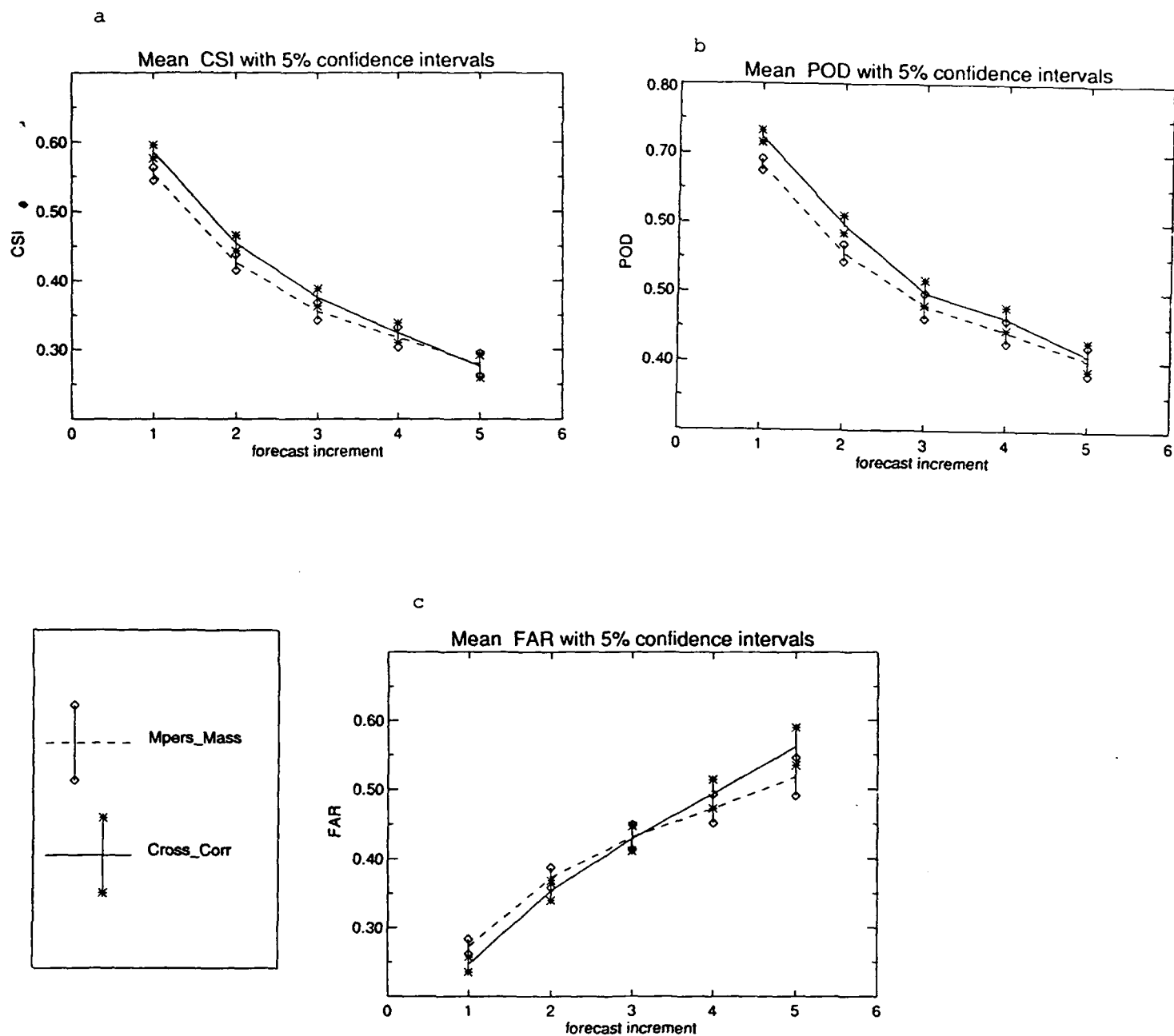


Figure 56: As Fig. 55, but with the whole contour technique eliminated from the comparison.



**Fig. 57:** Mean verification scores with 5% confidence intervals for the contour forecasts from the cross-correlation technique (solid, asterisk) and movable persistence based on the center of mass (dashed, diamond). From the ANOVA for the 40 case sample for the whole year. Shown are the CSI (a), POD (b), and FAR (c) as a function of forecast increment.

## Appendix A: A SHORT - TERM CLOUD FORECAST SCHEME USING CROSS CORRELATIONS

Thomas M. Hamill and Thomas Nehrkorn

*Atmospheric and Environmental Research, Inc.  
840 Memorial Dr  
Cambridge, Massachusetts 02139*

### 1. INTRODUCTION

This paper describes a trajectory-based cloud forecast technique based on lag cross correlations (Panofsky and Brier 1968). This technique generates a set of synthetic IR images nearly indistinguishable from the real images. It is suitable for short-range forecasts and can be run in a few minutes on current generation workstations. This scheme requires two IR satellite images of the same scene not more than one half hour apart; no other data are needed. Advective velocities are generated through the cross-correlation of multiple subsets of the two frames. This is based on the same technique used for satellite-derived winds (Merrill 1989), and has also been used for cloud and rainfall forecasts by Bellon et al. (1992) and applied to radar for boundary layer winds by Tuttle and Foote (1990). This particular application was designed with Air Force's Automated Weather Distribution System workstation in mind, but should be similarly useful within the civilian community.

Since the technique described here is trajectory-based, it has some typical problems associated with such techniques. For example, it cannot effectively develop or dissipate clouds, limiting the length of time and the weather regime for which they are useful. Another problem is determining correct advecting velocities; if an arbitrary level (say, 500 mb) wind field is used, low clouds may move unduly fast and high clouds too slowly. As will be shown, a correlations-based approach partly avoids this latter problem.

Longer-range forecast schemes (e.g., Slingo, 1987; Sundqvist et al. 1989; Mitchell and Hahn 1989) typically require the execution of a dynamic forecast model. They have their own set of drawbacks, such as poor spatial resolution, sensitivity to model spinup, and dependence on hard-to-forecast variables such as relative humidity. There is a crossover point between 6 and 18 hours where these longer-range forecast schemes become more skillful than trajectory schemes. Our technique was designed to meet the very short-range forecast (0 - 2 1/2 h) needs of the weather consumer; as such, it is clearly more skillful than any of the longer-range schemes during this period. Our testing was limited to this

forecast envelope; thus, we have not yet developed any statistical basis for determining the crossover time when this scheme's skill is exceeded by one of the longer-range schemes.

### 2. ALGORITHM DESCRIPTION

#### 2.1 Review of Cross-Correlations Technique

At the heart of our prototype cloud forecast technique is the derivation of displacements vectors (i.e., "winds") through a cross-correlations analysis. The technique is as follows: a subset of pixels from the first image in a satellite loop is chosen. For purpose of illustration in Figure 1, this subset is 8\*8; in our actual prototype scheme, the subset chosen is 15\*15. Next, based on the maximum possible wind displacement in half an hour, a search radius is chosen, and identically sized subsets of pixels from the second image with centers inside the search radius are correlated against the subset from the first image. If the scene has a uniform cloud layer, then the advective velocity for this layer will be defined by the vector from the center of the subset in Image 1 to the center of the subset with the maximum correlation in Image 2. This is illustrated in Figure 1, and a sample plot of correlation coefficients and a derived displacement vector is shown in Figure 2. In our technique, a cross correlations analysis is repeated at a gridded subset of points throughout the domain, and wind displacement vectors for all points are then derived through an objective analysis. [The domain is a lambert-conformal map projection covering the eastern two-thirds of the U.S. and southern Canada. Raw GOES IR imagery was remapped into a 256\*256 set of pixels in this projection, with an approximate resolution of 11 km.]

The correlations technique has drawbacks; there may be multiple cloud layers, in which case a single displacement vector may not be applicable for that region (Leese and Novak 1971). Second, if the frame is clear, then the displacement vector will be null, even with strong winds; use of the null wind in a trajectory analysis will prevent clouds from moving into the clear region. Further, if small subsets are used for the correlation analysis, the displacement vector may be inaccurate, reflecting a random high

correlation and not a true advective wind velocity.

The focus here is on producing a cloud forecast and not on the derivation of accurate wind observations for use in forecast model initialization; thus, these limitations can either be corrected or overcome. For the first problem, a displacement vector for a region with multiple cloud layers may represent the most appropriate single displacement vector that can be used in a one-layer trajectory scheme. Further, let us assume advection (rather than development or dissipation) is the dominant process, and there is only one cloud layer in a given area. If so, then this technique will derive more reasonable

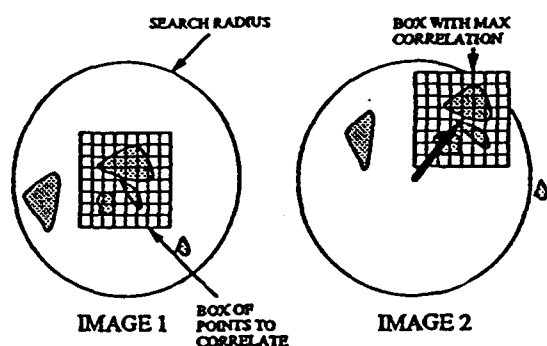


Figure 1. Illustration of correlation analysis and derivation of the displacement vector. The displacement vector is directed from the center of the correlation box in Image 1 to the center of the correlation box in Image 2 most highly correlated with Image 1.

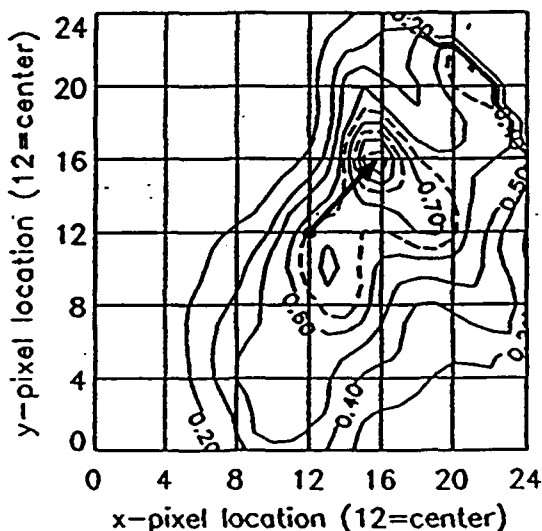


Figure 2. Example of a correlation field used in the derivation of a displacement vector. The point (12,2) is the center of the original correlation box. The displacement vector originates at this point and ends at the point with the highest correlation.

vectors than could be achieved using just single level winds such as a 500 mb wind field. Wind magnitudes generally increase with height, so by using the cross-correlations technique, areas of low cloud will have smaller magnitude displacement vectors than neighboring areas with high cloud. In essence, the trajectory wind field over the domain can be warped to represent correct advective velocities for a given region's cloud height.

Should part of the frame be cloud-free, those areas will have null displacement vectors. Since the cloud edge moving into an area is often one of the most crucial features to forecast, our technique was tailored to avoid the anomalous slowing of cloud edges. Hence, a restriction was imposed during the objective analysis step, where vectors are set for all pixels in the domain. The imposed restriction removes null displacement vectors from use as observations. As a result, wind velocities at cloud edges are not decreased from the assimilation of the null displacement vectors, and cloud edges are advected at more appropriate speeds. However, without correction, clear areas in front of the advancing clouds are also advected. This presents no problem when the clear-scene background is homogeneous, but if terrain features or lakes are present, they may appear to move. This problem was alleviated by identifying clear and cloudy pixels (using user-defined threshold values) and using persistence rather than advection for clear areas.

The last problem, inaccurate vectors and resultant displacement field noisiness, can be corrected in two ways: first, the size of the subset of pixels for correlation can be increased. However, this is done at the risk of increased computations. Our choice of a 15\*15 subset was a compromise between excessive CPU time and excessive noise. The second correction used here is a local consistency check to compare each derived vector against its neighbors. In this scheme, displacement vectors that deviate more than the width of four pixels from the local mean vector are replaced by the local mean (other deviations were tried, but four pixels gave the best result in our tests). Figure 3 shows a frame of the remapped GOES IR satellite imagery used in the correlation (1230 UTC 20 November 1991). Figure 4 shows a field of correlation displacement vectors derived from data between 1200 and 1230 UTC 20 November 1991, illustrating typical noise. Figure 5 shows the same field of displacement vectors after application of the consistency check. This set of vectors is itself quite consistent; for example, compare the results in Figure 5 with those in Figure 6, which shows the derived vectors for the frames 1/2 hour later, from 1230 and 1300 UTC imagery.



Figure 3. A frame of the satellite imagery used in the demonstration correlation analysis. Data is over the central and eastern U.S., valid at 1230 UTC 20 November 1991.

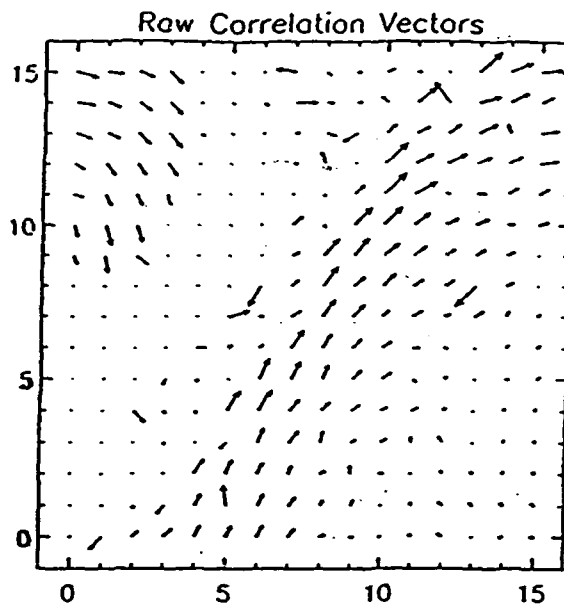


Figure 4: A sample of the raw displacement vectors derived from two successive frames of GOES imagery, 1200 and 1230 UTC 20 November 1991.

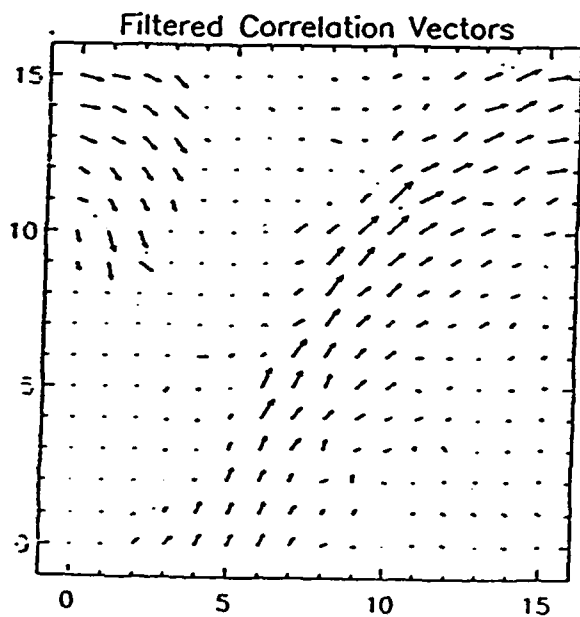


Figure 5. Displacement vectors from Figure 4 after quality control through a consistency check, examining and replacing wind vectors which deviate excessively from surrounding points.

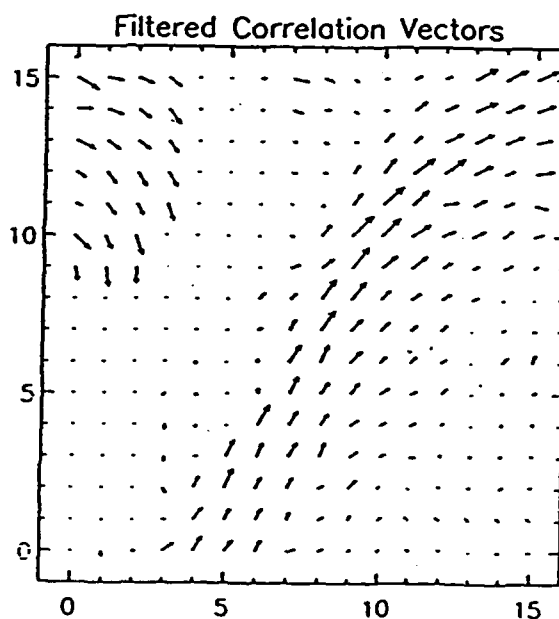


Figure 6. Displacement vectors derived from images 1/2 h later (and processed through consistency check).

## 2.2 Objective Analysis

The next step after derivation and QC of the displacement vectors is to take the field of vectors and produce a gridded displacement field for every point in the domain. This is done by objective analysis. The objective analysis technique and radius of influence was chosen to smooth the vector field slightly and produce a continuous flow pattern. We used two-pass objective Cressman-type objective analysis with a first pass summation function (Benjamin and Seaman 1985) of the form:

$$G1(i,j) = \frac{\sum_{n=1}^{nobs} (W^2 * D(x_n, y_n))}{\sum_{n=1}^{nobs} (W)}$$

Here G1 is the first guess at pixel (i,j). W is the standard isotropic Cressman weighting function dependent on the distance between the observation and the analysis point, and D is the displacement vector velocity for the observation at location (x<sub>n</sub>, y<sub>n</sub>). U and V components are analyzed separately in this process. The second pass summation function is of the form:

$$G2(i,j) = \frac{\sum_{n=1}^{nobs} (W^2 * (D(x_n, y_n) - G1(x_n, y_n)))}{\sum_{n=1}^{nobs} (W)}$$

where G2 represents the final analysis value. The radius of influence was set at 90 and 40 pixels for the first and second pass, respectively. As noted earlier, we throw out the null vectors before proceeding with the objective analysis. Figures 7 and 8 illustrate the effect of this; Figure 7 shows an objective analysis of the data in Figure 5, allowing the null vectors to be used. Figure 8 shows the implemented version, with the null vectors deleted. As can be seen in the upper-left corner of the domain, the influence of the windfield is spread into the clear areas, resulting in stronger magnitude winds along cloud edges.

## 2.3 Semi-Lagrangian Trajectory Forecast

In order to produce forecast images, pixel intensities from the latest satellite image are now advected using the full field of displacement vectors.

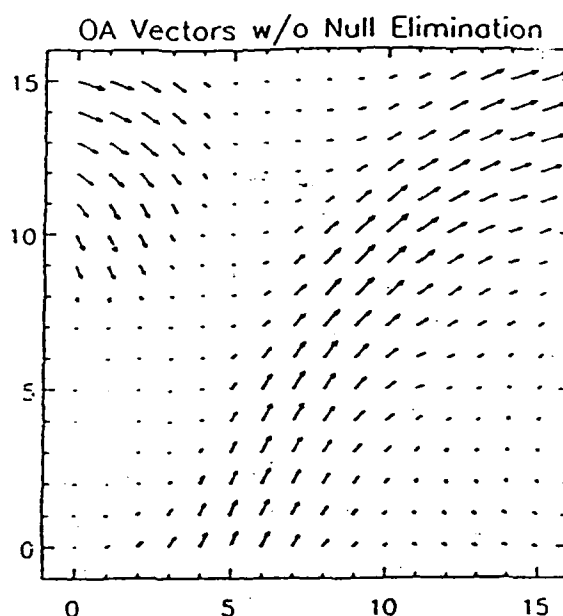


Figure 7. Objective analysis of data from Figure 5, without null displacement vectors eliminated.

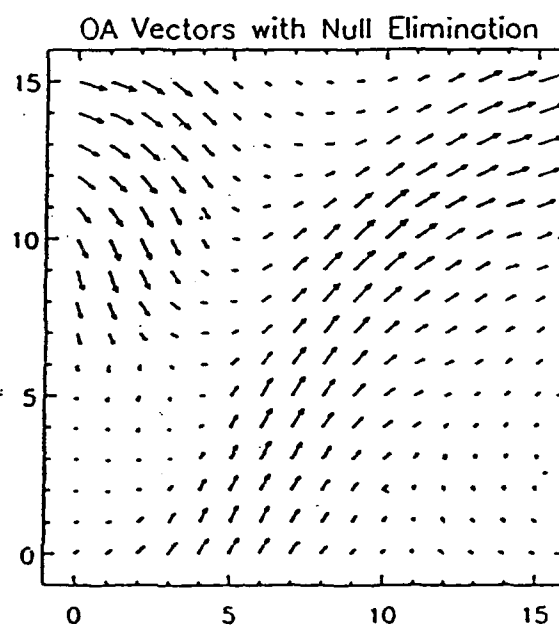


Figure 8. Objective analysis of data from Figure 5, with null displacement vectors eliminated.

Before the trajectory technique is performed, however, the U and V-component 1/2 hour displacement vectors are modified slightly through a semi-lagrangian scheme (Staniforth and Cole 1991). The use of semi-lagrangian displacement vector rather than the original displacement vector itself markedly improves the trajectory forecasts in areas where the wind field at the trajectory endpoint differs



significantly from the wind field at the trajectory origin. In essence, this scheme iterates to find the correct compromise trajectory.

With final advective velocities calculated, a simple backwards-in-time trajectory is used with the initial satellite data to make forecast images. In this scheme, the trajectory endpoints for time interval  $t(i)$  are known; they are the regular set of gridpoints for the domain. Using the semi-lagrangian vectors, the scheme finds the trajectory origin at time  $t(i-1)$ ; if the origin is coincided with a pixel, that pixel value is used as the forecast value; however, if the origin does not lie directly on a pixel, then a bilinear interpolation of the surrounding four pixel values is performed to determine the forecast pixel value. If the trajectory origin is outside the domain, the trajectory is assumed to originate at the nearest border point. The forecast scheme steps forward in 1/2 hour intervals, with each successive forecast frame used in the initialization of the next step.

### 3. RESULTS

Our prototype cloud forecast scheme has now been tested with satellite images over the central U.S. for each season. It shows skill over persistence for all time periods tested (1/2 to 2 1/2 hours in 1/2 hour increments). The scheme was also tested side-by-side with an advection scheme using the 500 mb wind field, and comparison tests were made against several contour extrapolation methods.

#### 3.1 Comparison with Persistence and 500 mb Advection Forecasts

For all tests and all times, the correlations-based advection scheme showed less error than persistence. An ensemble of 10 forecasts from each of the four seasons were made, and RMS errors (in pixel grayshade values) were calculated using the observed satellite imagery for verification. The fall, winter, spring, summer error statistics for correlations forecasts and persistence are summarized in Table 1. As shown, both persistence and correlations exhibit higher errors in summer than in winter. From visual inspection, this was clearly due to the dominance of convective development and dissipation over advection during the summer months. Conversely, during the winter, advective processes seemed to dominate, and both persistence and the correlations technique show smaller errors, though the *percentage* improvement of correlations-based forecasts over persistence is greater in winter than in summer.

Fcst. Hour	Season	Correlation RMS	500 mb RMS	Persistence RMS
1/2	Fall	9.13	--	12.32
	Winter	8.57	9.36	11.30
	Spring	8.98	--	11.95
	Summer	11.28	11.63	13.96
1	Fall	12.87	--	16.21
	Winter	11.67	12.82	14.98
	Spring	12.55	--	16.04
	Summer	16.32	16.99	19.77
1 1/2	Fall	15.35	--	18.59
	Winter	14.19	15.22	17.38
	Spring	14.99	--	18.55
	Summer	19.94	20.61	23.46
2	Fall	17.27	--	20.48
	Winter	16.12	17.09	19.23
	Spring	17.02	--	20.51
	Summer	22.77	23.44	26.36
2 1/2	Fall	18.95	--	22.16
	Winter	17.79	18.64	20.83
	Spring	18.64	--	22.19
	Summer	25.25	25.82	28.78

Table 1. Comparison of RMS Errors for 10-case ensembles of correlation, 500 mb, and persistence forecasts over each of the four seasons, and for each forecast interval. Units are grayshade values, which range from 0-256 in the original imagery.

A reasonable alternative candidate to a correlations-based forecast scheme is one using 500 mb winds for displacement vectors. To test this, we also compared a set of 500-mb-based forecasts to the observed IR pixel values for the winter and summer cases. The results for these are also presented in Table 1. Generally, the correlations forecasts are clearly superior in the winter, but much closer to the RMS of the 500 mb forecasts in the summer. The generally higher RMS in the summer and the lesser RMS difference between correlations and 500 mb forecasts for summer cases is most likely due to the dominance of convective development and dissipation. During the summer, use of the 500 mb wind field as a steering current for thunderstorms generally makes as much sense as correlations-derived winds, which cannot be expected to produce reliable wind vectors in regions of development and dissipation. Conversely, during the winter months, the correlation scheme's ability to determine an accurate advecting velocity regardless of the height of the cloud is likely responsible for its higher skill.

A few forecasts were made using 700 mb winds instead of 500 mb; the verification scores for this small sample were generally worse using 700 mb data than 500 mb.

### 3.2 Comparison Against Contouring Schemes

Other techniques exist for the extrapolation of prominent cloud features, notably contour extrapolation methods (Heideman et al. 1990; Ruggiero et al. 1991). For these methods, significant weather features such as thunderstorms are contoured at a user-selected brightness level, and the past behavior of the contour shape and movement is used to forecast future shape and movement. The cross-correlations based forecasts were tailored to also produce contour forecasts and are currently being compared side-by-side against the existing contour forecast schemes. The critical success index, false alarm ratio, and probability of detection (Stanski et al. 1989) will be the benchmark performance indices in this comparison. Early results indicate competitive performance compared with contour-based schemes. Quantitative results will be available at the conference.

### 4. CONCLUSIONS

A cross-correlations based cloud forecast technique has been developed which is skillful at extrapolating cloud features. The output is a set of synthetic satellite images which may be looped in combination with analyzed images. This scheme was designed for a U.S. Air Force weather workstation, but it may also be useful to forecasters and broadcast meteorologists who need short-range cloud forecasts.

### 5. ACKNOWLEDGMENTS

The authors would like to acknowledge the careful reviews provided by Don Chisholm, Ken Heideman, and Stu Muench at the U.S. Air Force Phillips Laboratory, and by Gary Gustafson, Jean-Francois Louis, Larry Knowlton, and Jeanne Sparrow at AER. This research was supported by the U. S. Air Force Systems Command under contract F19628-92-C-0014.

### 6. REFERENCES

- Bellon, A., A. Kilambi, G. L. Austin, and M. R. Duncan, 1992: A satellite and radar rainfall observational and forecast system. *Preprints, 8th AMS Interactive Information and Processing Systems Conference*, pp. J110-J116.
- Benjamin, S. G., and N. L. Seaman, 1985: A simple scheme for objective analysis in curved flow. *Mon. Wea. Rev.*, **113**, 1184-1198.
- Heideman, K. F., H.-C. Huang, and F. H. Ruggiero, 1990: Evaluation of a nowcasting technique based on GOES IR satellite imagery. *Preprints, 5th AMS Conf. Satellite Meteor. and Ocean.*, London, England, 366-371.
- Leese, J. A., and C. S. Novak, 1971: An automated technique for obtaining cloud motion from geosynchronous satellite data using cross correlation. *J Appl. Meteor.*, **16**, 118-132.
- Merrill, R. T., 1989: Advances in the automated production of wind estimates from geostationary satellite imagery. *Preprints, 4th AMS Conf. Satellite Meteor. and Ocean.*, San Diego, CA, 246-250.
- Mitchell, K. E., and D. Hahn, 1989: Development of a cloud forecast scheme for the GL baseline spectral model. *GL-TR-89-0343*, Phillips Laboratory / Geophysics Directorate, Hanscom AFB, MA, 147 pp., ADA231595.
- Panofsky, H. A., and G.W. Brier, 1968: *Some Applications of Statistics to Meteorology*. Penn State University, University Park, PA. 224 pp.
- Ruggiero, F. H., K. F. Heideman, and J. Doherty, 1991: An evaluation of three techniques for nowcasting precipitation fields using weather radar. *Preprints, 25th AMS Conf. Radar Meteor.*, Paris, France, 83-86.
- Slingo, J. M., 1987: The development and verification of a cloud prediction scheme for the ECMWF model. *Quart J. Roy. Meteor. Soc.*, **113**, 899-927.
- Staniforth, A. and J. Cote, 1991: Semi-lagrangian integration schemes for atmospheric models - A review. *Mon. Wea. Rev.*, **119**, 2206-2223.
- Stanski, H.R., L. J. Wilson, and W. R. Burrows, 1989: Survey of common verification methods in meteorology. MSRB 89-5, Canadian Atmospheric Environment Service, Downsview, Ontario, 114 pp.
- Sundqvist, H., E. Berge, and J. Kristjansson, 1989: Condensation and cloud parameterization studies with a mesoscale numerical weather prediction model. *Mon. Wea. Rev.*, **117**, 1641-1657.
- Tuttle, J. and G. B. Foote, 1990: Determination of the boundary layer airflow from a single Doppler radar. *J Atmos. Ocean. Tech.*, **7**, 218-232.